Coherent Diffractive ρ Production by Neutrinos in NOMAD.

Nicole Michelle Hyett

School of Physics

The University of Melbourne

Parkville Victoria 3052

Australia

August 4, 1998

Thesis submitted in total fulfilment of the requirements of the degree of Doctor of Philosophy.

Produced on acid-free paper.

Abstract

A search for coherent diffractive production of ρ mesons has been performed at NOMAD under exposure to neutrinos from the CERN SPS wide band neutrino beam. Monte Carlo simulations were used to study properties of the signal as well as background processes. Using data taken during 1995 22 events of the type $\mu\pi^0\pi^+$ with momentum transfer squared less than 0.1 GeV were found. Two methods of estimating the background were used. One method yields an estimated background of 2.2 ± 2 events and signal of 20 ± 4 events. The other method does not yield a conclusive signal. The slope of the momentum transfer squared distribution (t' - distribution) under the first method of background estimation was measured to be $(28 \pm 9)\ GeV^{-2}$. The cross-section was measured to be $(71 \pm 14) \times 10^{-40}\ cm^2$ per carbon nucleus, in agreement with theoretical predictions.

I declare that the length of this thesis does not exceed 100,000 words.

Acknowledgments

Many people have contributed to the successful completion of this thesis. I would like to take this opportunity to thank them all for their help, advice and support.

Firstly, I would like to thank Dr. Stuart Tovey my PhD supervisor, for allowing me the opportunity to undertake the work towards this thesis. I would also like to thank him for his patience and forbearance in supervising my work. His calm but constant enthusiasm for the project was greatly appreciated.

I would like to thank Dr. Kevin Varvell who has given so freely of his time to explain physics, to help with software problems and to contribute ideas and suggestions.

I would also like to thank the EPP group who have always provided a friendly and helpful environment in which to work. In particular I would like to thank my friends and colleagues Caroline Poulsen and Fawzi Fares who have worked, suffered and laughed along with me since we began our studies together.

I would like to thank the Lausanne High Energy Physics group for allowing me the opportunity to work as part of their team during time spent in Lausanne on my Swiss Government Scholarship. I would like to thank Dr. Min-Tam Tran for providing supervision and along with Dr. Ian Bird for the valuable advice given to me. I would especially like to thank Martine Steininger whose warmth and friendship made my stay in Lausanne one which I will always look back upon fondly.

I would like to thank Fawzi Fares and Ralph Gailis for taking the time and effort to proof read this thesis.

If it were not for the DPS, the time spent completing this work would have been very dull indeed. I would like to thank them for the many jokes and good times we have shared.

Finally, I would like to thank my parents who have always encouraged me to pursue my goals and to work hard to bring about their achievement. This thesis

could not have been completed without their love and support.

This work has been partly funded by the Australian Research Council (ARC) and the Department of Industry, Science and Technology(DIST).

Contents

List of Figures

List of Tables

Chapter 1

Introduction

Coherent diffractive ρ production by neutrinos occurs at low four-momentum transfer and high energy transfer. These interactions are generally understood to occur via the coupling of the weak charged current to the vector meson, which scatters diffractively from the target nucleus. Since coherent events are those in which the nucleus interacts as a whole, ie without break-up, and with small recoil energy, these events have a very sharp momentum transfer distribution.

A study of these interactions is a clear probe of the hypothesis of the conservation of the vector current. The diffraction model of interactions [1] estimates the total cross-sections for leptonic production of π, ρ and A_1 mesons, using the meson-dominance assumption, so a measurement of these cross-sections can give an indication of the accuracy and reliability of this model.

Previous searches for coherent diffractive ρ production have taken place in bubble chambers, and have characteristically yielded positive results, but with low statistics. The small amount of data available in this area results in large errors and a serious difficulty in understanding the relationship between cross-section and energy. It is possible to study this type of interaction with the use of modern counter experiments, utilizing the high interaction rate and the accuracy to which particles can be tracked in these detectors. The **N**eutrino **O**scillation **MA**gnetic **D**etector, NOMAD, at the European Laboratory for Particle Physics, CERN, near Geneva, Switzerland is one such detector. NOMAD was primarily designed to search for the oscillation from ν_μ to ν_τ. However, the detector is also well suited to study the coherent diffractive production of ρ mesons and was used to do so in this analysis.

This report presents an observation of 22 events of the type ($\mu^-\pi^+\pi^0$), with $|t'|$, the four momentum transfer squared, less than 0.1 GeV^2. Of these 22 events, the background was estimated to be between (2.2 ± 3) and (25 ± 9) events, depending on which method was used to estimate it. The signal was estimated to be (20 ± 4) and (-3 ± 10) events. Again, the result varies according to which method of background estimation is used.

The data used for this analysis were taken from the 1995 exposure of NOMAD to the CERN SPS wide band neutrino beam. During the same data taking period, $\approx 60,000$ charged current events were measured. This analysis can be seen as a detailed feasibility study into the possibility of detecting coherent diffractive ρ in NOMAD. The extension of this analysis to include subsequent data would significantly contribute to our understanding of the processes described above.

Chapter 2 is a review of the relevant theory for this analysis. An account of the basic precepts of electroweak theory, the conserved vector current hypothesis, and the vector meson dominance assumption is given, along with a description of the diffraction model of high-energy leptonic interactions. The theoretical cross-section is derived under the assumptions of the models mentioned above.

In Chapter 3, NOMAD is described in detail, with special emphasis given to the electromagnetic calorimeter and the drift chambers as the sub-detectors most relevant to this analysis. A brief description of the neutrino beam and the triggers used is also given.

Chapter 4 goes on to describe the analysis of the candidate coherent diffractive ρ signal. The Monte Carlo simulation algorithm and parameters are described. A study of potential backgrounds to the signal is performed and a background estimate is given. The cuts used to isolate the coherent signal and the efficiency of this process is summarized. The fit done to the t'-distribution is explained. Other kinematic distributions are also examined. The cross-section for the coherent ρ process is calculated along with its uncertainty. Comparisons with previous experiments and theoretical predictions are made.

A brief outline of the authors particular involvement in NOMAD is given in Appendix A.

In this thesis, natural units, ie $\hbar = c = 1$, are used at all times.

Chapter 2

Theory

2.1 Theoretical Introduction

In a neutrino induced interaction, the $\bar{d}u$ pair from the Cabibbo favored transition $W \rightarrow \bar{d}u$ may coherently rescatter from the nucleus, mostly in a diffractive way, see Figure 2.1. A coherent process is one in which the nucleus recoils without breaking up or changing from the ground state. In order for this to occur, only a small 4-momentum transfer to the nucleus is permitted. Diffractive scattering occurs when momentum is transferred via the exchange of a pomeron ($\mathcal{P}$). In diffractive scattering, the momentum exchange spectrum is sharply peaked near its minimum value.

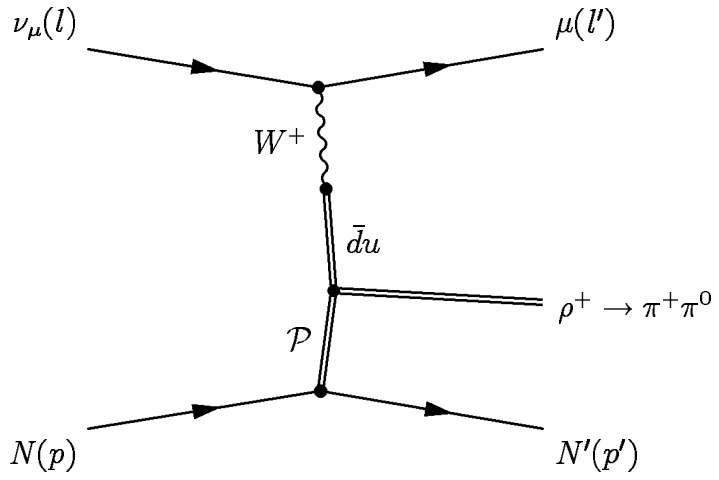

Figure 2.1: The coherent diffractive ρ production process.

The specific tests performed by studying these types of events given sufficient statistics are :

- The coupling of weak currents to vector mesons.
- The conservation of the vector current (CVC).
- The vector meson dominance (VMD) hypothesis.

2.1.1 The Diffraction Mechanism

The pomeron was originally proposed [2] to fill the position $M^2 = 0$ on a plot of angular momentum vs mass squared. The pomeron has the quantum numbers of the vacuum, (ie zero charge, zero isospin, spin parity 0^+) and is now postulated to be a collection of gluons with the same quantum numbers as the vacuum. By studying the diffractive process and investigating matters such as the t-dependence (where t is the 4-momentum transfer squared to the nucleus) of the interaction a better understanding of pomerons, particularly with respect to their coupling to vector mesons, can be gained.

The Salam-Weinberg model of weak interactions [3] leads us to expect V-A coupling for weak interactions. In interactions such as that shown in Figure 2.1, the quantum numbers of the final state hadrons are identical to those of the intermediate vector meson. Therefore by studying the final state hadrons, it is possible to study the spin nature of the current and learn something of the V-A contribution to that current.

For the momentum exchange to occur dominantly via pomeron exchange, there must be small momentum transfer from the leptonic system to the hadronic one, ie small Q^2 and small t[1]. Q^2 must be of the order of a few GeV^2, and t must be less than the inverse pion Compton wavelength. In fact, the main feature of diffractive scattering is the sharp exponential distribution of the momentum transfer [1]. This allows the parameterization of the differential cross-sections for vector mesons by exponential t-distributions, e^{-bt}. An exponential parameterization is chosen for consistency with electroproduction [9]. The slope b is of the order of the transverse

[1]Here the standard notation has been used. It will be defined in more detail in Section 2.2.

dimensions of the nucleus, $b \sim A^{2/3}$. In contrast, incoherent scattering typically has a slope of $b \sim A^{1/3}$.

2.1.2 The Coherence Condition

The coherence condition is that all the nucleons inside a nucleus of radius R_N must react in phase. Each nucleon contributes a phase $e^{i(\vec{p}-\vec{p'})\cdot\vec{r}}$, where $p - \vec{p'}$ is the momentum acquired by the nucleon and $\vec{r}$ is the position of the nucleon inside the nucleus. For the coherence condition to be met, the phase factor should not oscillate rapidly over distances comparable with the nuclear radius, i.e. the momentum transfer between the incident and scattered waves must be small. More specifically

$$(\vec{p} - \vec{p'}) = \sqrt{|t|} < 1/R_N, \tag{2.1}$$

where $R_N = R_0 A^{1/3}$ is the nuclear radius, $R_0 = 1.2\ fm$ and A is the atomic mass of the nucleus.

The NOMAD target consists mostly of carbon. For a detailed description of the NOMAD target see Section 3.4. For carbon nuclei Equation 2.1 becomes

$$\sqrt{|t|} \lesssim 1/2.75\ fm^{-1} \approx 72\ MeV, \tag{2.2}$$

The kinetic energy acquired by the nucleus is

$$T = \frac{|t|}{2M_N} < 3\ MeV. \tag{2.3}$$

where M_N is the mass of the nucleus.

If the coherence condition is met, the momentum transfer is small enough to prevent the struck nucleon from escaping the nucleus. Consequently, coherent interactions are characterized by the way the nucleus recoils as a whole, without break-up and with a small recoil energy.

In order to have a truly coherent interaction, no transfer of any quantum

number (including isospin to exclude π transfer) is allowed. If there were a quantum number transfer, the result would be an interaction with a specific nucleon, rather than the whole conglomerate.

These interactions between neutrinos and nuclei are also illustrative of the effects of wave particle duality, since these interactions are a result of the interference of the scattering wave of the neutrino with those of the nucleons in the target [6].

2.1.3 Hadron Dominance

The hadron dominance model for high energy leptonic interactions was first introduced by Piketty and Stodolsky [1], in analogy with the successful hadron dominance model used in the photoproduction of vector mesons. They linked the cross-section for electroproduction of vector mesons to that of neutrino production, with the use of the Conserved Vector Current (CVC) hypothesis [4], [5].

The study of coherent ρ interactions provide a strong test of the hadron dominance model for interactions with low Q^2. The weak current can be imagined as a superposition of virtual hadron states. These states can fluctuate into real states, changing the energy of the system, for periods of time corresponding to a "coherence length" l_c (as stated in [6]) such that

$$l_c = \Delta t_c \approx \frac{2\nu}{Q^2 + m_h^2}, \tag{2.4}$$

where Δt_c is the coherence time, m_h is the mass of the real hadron and Q and ν have there usual meanings and are defined in Section 2.2. If the coherence time is greater than or equal to the typical interaction time , $\Delta t_c \geq \Delta t_i$, the weak current behaves as a real hadron current. That is to say, the hadron constituents of the current only appear if sufficient time is allowed. This criterion is met only at high energy.

2.2 Kinematics

The Feynman diagram for the coherent diffractive process

$$\nu_\mu N \rightarrow \mu^- \rho^+ N' \tag{2.5}$$

is shown in Figure 2.1. The notation used is that l and l' are the four-momenta of the initial and final leptons, and p and p' are the four-momenta of the initial and final nucleus states respectively. Four-vectors are denoted in normal type, while three-vectors are written in bold font.

The transfer of energy from the incident lepton to the hadronic system is defined by

$$\nu = E_\nu - E_\mu. \tag{2.6}$$

The negative of the 4-momentum transfer squared from the incident lepton to the hadronic system is

$$\begin{aligned} Q^2 &= -q^2 \\ &= -(l - l')^2 \\ &\geq 0. \end{aligned} \tag{2.7}$$

The 4-momentum transfer squared to the nucleus is

$$\begin{aligned} t &= (p - p')^2 \\ &\leq 0. \end{aligned} \tag{2.8}$$

This variable has a kinematically allowed minimum [2] [7] for a given Q^2 and ν given by

$$t_{min}(Q^2, \nu) = \frac{(A_2 - \sqrt{A_2^2 - A_1 A_3})}{A_1}, \tag{2.9}$$

[2]Since the variable t is less than zero, the t with the smallest modulus is actually a maximum. However, it will be referred to as a minimum throughout this analysis, as in other work.

where

$$\begin{aligned} A_1 &= 1 + 2\frac{\nu}{M_N} - \frac{Q^2}{M_N^2} \\ A_2 &= 2(Q^2 + \nu^2) - (1 + \frac{\nu}{M_N})(Q^2 + M_\rho^2) \\ A_3 &= (Q^2 + M_\rho^2)^2. \end{aligned} \tag{2.10}$$

where M_N is the mass of the target nucleus and M_ρ is the mass of the ρ meson. Occasionally the approximation

$$t_{min} = \left(\frac{Q^2 + M_\rho^2}{2\nu}\right)^2 \tag{2.11}$$

is used, although this approximation does not seem necessary. In fact, there is even some evidence [7] that this approximation overestimates the number of predicted events by a factor of up to 3 times in comparison with predictions made using the exact value of t_{min}. Throughout this analysis, the exact value of t_{min} has been used.

The Bjorken variables, x and y, are defined as

$$x = \frac{Q^2}{2\nu M_N}, \tag{2.12}$$

and

$$y = \frac{\nu}{E_\nu}. \tag{2.13}$$

The hadronic invariant mass squared is denoted by

$$\begin{aligned} W^2 &= 2\nu M_N - Q^2 + M_N^2 \\ &= Q^2(\frac{1}{x} - 1) + M_N^2. \end{aligned} \tag{2.14}$$

2.2.1 Kinematical Constraints

The cross-section of the coherent production of ρ mesons is constrained by kinematical limits over a range of energies. At higher energies the dominant effect is

related to t_{min} and nuclear break-up, while at lower energies constraints on Bjorken x and y are dominant.

Kinematical constraints occur if one requires that the cosine squared of the scattering angle (see Figure 2.2) to be less than one, and the invariant mass squared of the system to be sufficiently large. One therefore obtains limits for the xy-plane. These limits can be expressed mathematically as shown below in Equations 2.15 and 2.16, and can be seen graphically in Figure 2.3.

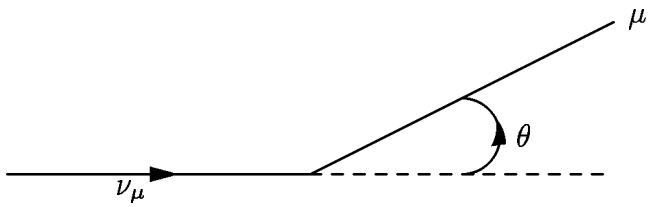

Figure 2.2: The definition of the scattering angle.

$$\cos^2\theta \leq 1 \Longrightarrow y \leq \frac{1}{1+(M_N x)/(2E)} \tag{2.15}$$

$$W^2 \geq (M_\rho + M_N)^2 \Longrightarrow Ey(1-x) \geq M_\rho + \frac{M_\rho^2}{2M_N} \tag{2.16}$$

2.2.2 An expression for the square of the 4-momentum transfer to the nucleus.

In NOMAD it is not possible to measure the neutrino energy directly, nor is it possible to measure the momentum of the recoil nucleus. However, if one makes the assumption that the interaction is coherent and that the mass of the nucleus is known, an exact expression for t can be derived. Appendix B shows the derivation of this quantity.

$$|t| = \frac{[\sum_i (E_i - p_i^L)]^2 + [\sum_i p_i^T]^2}{1 - \sum_i (E_i - p_i^L)/M_N}. \tag{2.17}$$

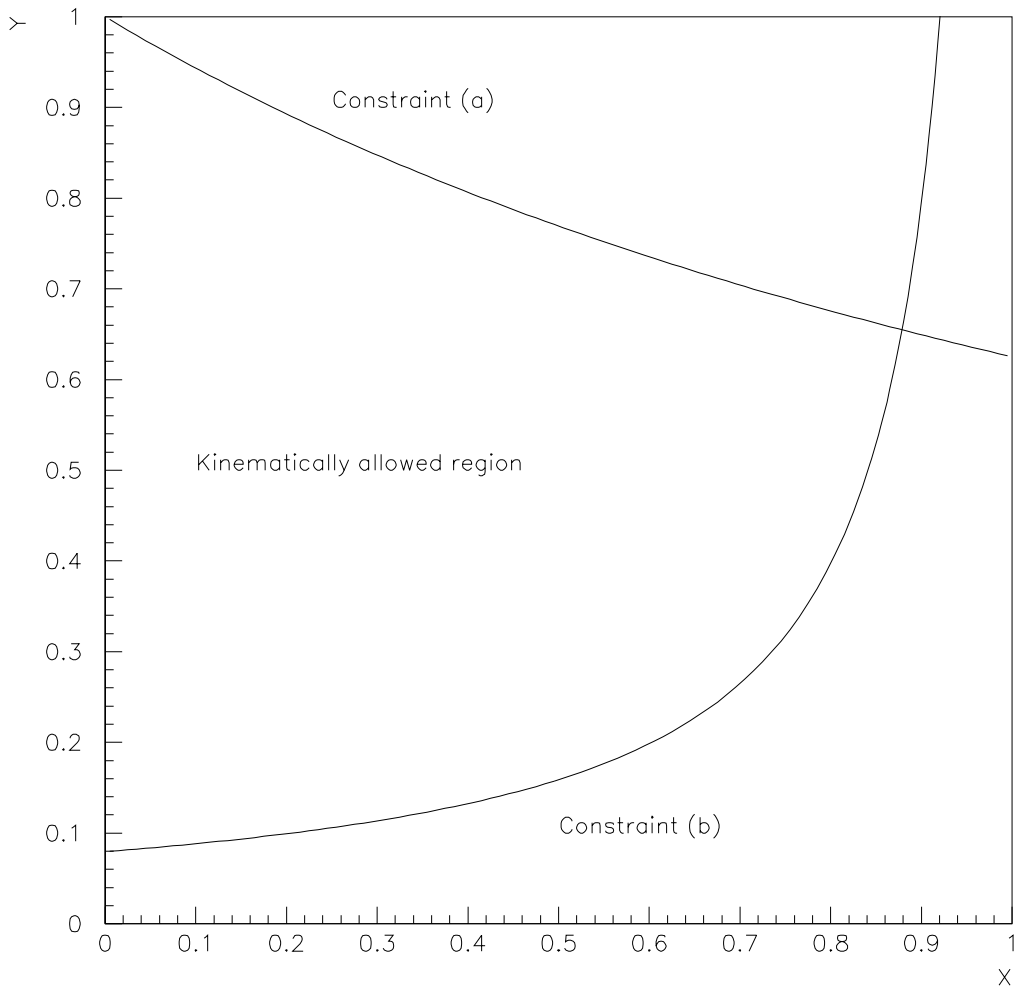

Figure 2.3: The kinematical limits on the xy-plane, for $E_\nu = 10\ GeV$. (a) Constraint given by Equation 2.15. (b) Constraint given by Equation 2.16.

where the sum is over all the final state particles ($\mu^-\pi^+\pi^0$). E_i is the energy of the i^{th} particle, and $p_i^{L(T)}$ are the longitudinal (transverse) components of the three-momenta of the i^{th} particle with respect to the neutrino beam. M_N is the mass of the nucleus.

In much of the literature an approximation for t is used

$$|t| = [\sum_i (E_i - p_i^L)]^2 + [\sum_i \mathbf{p}_i^T]^2. \tag{2.18}$$

For small values of t this approximation is a very good one.

2.3 Weak Interactions and V-A Theory

Lorentz invariance and quantum field theory require that all interactions proceed via a combination of at most five mechanisms, these being the scalar (S), psuedoscalar (P), vector (V), axial-vector (A) and tensor (T) currents. It is well established that the weak charged current is of the form vector minus axial-vector (V-A).

By studying the rate of diffractive production of vector particles, such as the ρ, particularly when compared to the rates for axial-vector and psuedoscalar particles like the A_1 and π respectively, this V-A nature can be studied in detail. In particular, a knowledge of how vector mesons are coupled to weak charged currents can be obtained.

The leptonic current for weak charged current interactions can be written as

$$\begin{aligned} J_\alpha(x) &= \sum_l \bar{u}_l(x')\gamma_\alpha(1-\gamma_5)u_{\nu_l}(x), \\ J_\alpha^\dagger(x) &= \sum_l \bar{u}_{\nu_l}(x)\gamma_\alpha(1-\gamma_5)u_l(x'), \end{aligned} \tag{2.19}$$

where the l labels refer to the different lepton fields $l = e, \mu, \tau$, and ν_l the corresponding neutrino fields. The $u(x)$ are the linear creation and annihilation operators of the lepton fields. $J_\alpha(x)$ and $J_\alpha^\dagger(x)$ are called currents because they transform like four-vectors under Lorentz transformations.

The weak interaction Hamiltonian takes the form

$$\mathcal{H} = g_W \left(J^{\alpha\dagger}(x) W_\alpha(x) + J^\alpha(x) W^\dagger_\alpha(x) \right), \tag{2.20}$$

where g_W is a dimensionless coupling constant and $W_\alpha(x)$ is the vector boson propagator. This interaction couples the field $W_\alpha(x)$ to the leptonic vector current, and so $W_\alpha(x)$ must be a vector field. The W particles are therefore vector bosons. This interaction is known as V-A because the current, $J^\alpha(x)$, can be made from the difference of a vector part and an axial vector part. $J^\alpha(x)$ can be written as

$$J^\alpha(x) = J^\alpha_V(x) - J^\alpha_A(x), \tag{2.21}$$

where the vector and axial vector parts are expressed respectively as:

$$\begin{aligned} J^\alpha_V(x) &= \sum_l \bar{u}_l(x)\gamma^\alpha u_{\nu_l}(x), \\ J^\alpha_A(x) &= \sum_l \bar{u}_l(x)\gamma^\alpha\gamma^5 u_{\nu_l}(x). \end{aligned} \tag{2.22}$$

2.3.1 The Vector Current

The conserved vector current (CVC) hypothesis is the precursor to modern electroweak theory. It arises as a consequence of isotopic invariance. That is, it puts the charged weak and the electromagnetic currents in the same isotriplet, so that the non-strange weak charged current and the electromagnetic current form an isospin multiplet [9], [10].

Production of coherent ρ mesons on nuclei test the vector current behavior of the hadron dominance model, and so provide a test of the CVC assumption in weak interactions. It is known that the electromagnetic interactions violate CVC [11] and it is this violation that causes the mass difference between the u and d quarks, ie $M_u - M_d \neq 0$.

The importance of the conservation of the vector current to coherent diffractive ρ production lies in the way it allows the connection between the cross-section

for vector meson production to that of the corresponding cross-section for the electromagnetic current to be made.

2.3.2 Calculation of the Matrix Element Squared.

The production of any given hadronic state $\mathcal{F}$, from the initial state $\mathcal{I}$, is now considered. The kinematics for this process are described in Section 2.2. The scattering matrix element for this process is given by [1]

$$\mathcal{M}_{\mu\nu} = \frac{G_F}{\sqrt{2}} l_\mu v_\nu^{\mathcal{FI}}, \tag{2.23}$$

where l_μ is the leptonic current matrix element, $v_\nu^{\mathcal{FI}}$ is the hadronic element, the weak coupling constant $G_F = 1.166 \times 10^{-5}\ GeV^{-2}$ and

$$\frac{G_F}{\sqrt{2}} = \left(\frac{g_W}{M_W}\right)^2. \tag{2.24}$$

The Leptonic Current

The leptonic current for weak scattering is described by

$$l_\mu = \bar{u}(l')\gamma_\mu(1-\gamma_5)u(l). \tag{2.25}$$

Continuing to look at the purely leptonic contribution, one then squares the amplitude, averages over initial states and sums over the final ones, to write $L_{\mu\nu}$ for weak scattering as

$$L_{\mu\nu} = \overline{\sum_{\mathcal{I}}} \sum_{\mathcal{F}} l_\mu^* l_\nu, \tag{2.26}$$

or more explicitly,

$$L_{\mu\nu} = (l_\mu l'_\nu + l_\nu l'_\mu - (l.l')\delta_{\mu\nu} + \epsilon_{\mu\nu\alpha\beta} l^\alpha l'^\beta). \tag{2.27}$$

Replacing l' with $l' = l - q$ this can be written as

$$L_{\mu\nu} = (2l_\mu l_\nu - l_\mu q_\nu - q_\mu l_\nu + (l.q)\delta_{\mu\nu} + \epsilon_{\mu\nu\alpha\beta} l^\alpha q^\beta). \tag{2.28}$$

The Hadronic Current

The hadronic part of the matrix element can be expressed as

$$V_{\mu\nu} = \overline{\sum_{\mathcal{I}}} \sum_{\mathcal{F}} v_\mu^{*\mathcal{F}\mathcal{I}} v_\nu^{\mathcal{F}\mathcal{I}}. \tag{2.29}$$

Remembering that p_μ is the momentum for the target nucleus and q_μ is the momentum carried by the vector current, the most general matrix element can be derived:

$$V_{\mu\nu} = -F_1\delta_{\mu\nu} + F_2\frac{p_\mu p_\nu}{M^2} + F_4\frac{q_\mu q_\nu}{M^2} + F_5\frac{p_\mu q_\nu + q_\mu p_\nu}{M^2}, \tag{2.30}$$

where F_i^V are real positive functions of q^2 and ν. There is no antisymmetric cross term ($F_3 = 0$), as this arises as a consequence of the interference between the vector and axial vector parts. Invoking the conservation of the vector current, such that

$$q_\mu V_{\mu\nu} = V_{\mu\nu} q_\mu = 0, \tag{2.31}$$

the four unknowns can be reduced to only two,

$$F_5 = F_2\frac{(q.p)}{Q^2} \tag{2.32}$$

and

$$F_4 = -F_1\frac{M^2}{Q^2} + F_2\frac{(q.p)^2}{Q^4}. \tag{2.33}$$

Hence Equation 2.30 is expressed in terms of just two structure functions,

$$\begin{aligned} V_{\mu\nu} \;=\; & F_1[\delta_{\mu\nu} - \frac{q_\mu q_\nu}{Q^2}] - \\ & \frac{F_2}{M^2}[p_\mu - \frac{q.p}{Q^2}q_\mu][p_\nu - \frac{q.p}{Q^2}q_\nu]. \end{aligned} \tag{2.34}$$

The Generalized Cross-Section

Multiplying the leptonic contribution by the hadronic one and using the kinematic relations described in Section 2.2 allows the matrix element squared to be written as

$$\begin{aligned} |\mathcal{M}|^2 &= \frac{G_F^2}{2} L_{\mu\nu} V^{\mu\nu} \\ &= \frac{G_F^2}{4} [2F_1 Q^2 + F_2(4EE' - Q^2)]. \end{aligned} \tag{2.35}$$

The generalized cross-section relation is given by [12]

$$d\sigma = \frac{(2\pi)^4}{4M_N E} |\mathcal{M}|^2 \, d(LIPS). \tag{2.36}$$

where the Lorentz invariant phase space (LIPS) factor is given by

$$d(LIPS) = \delta^{(4)}(l + p - l' - p') \frac{d^3\mathbf{l}'}{(2\pi)^3 2E'} \frac{d^3\mathbf{p}'}{(2\pi)^3 2E_F}. \tag{2.37}$$

Integrating over phase space, one now arrives at the differential cross-section for coherent diffractive ρ production, written in terms of the two functions F_1 and F_2

$$\frac{d^2\sigma}{dQ^2 d\nu} = \frac{G_F^2}{8\pi^2 E^2} [2F_1 Q^2 + F_2(4EE' - Q^2)]. \tag{2.38}$$

2.4 The Diffraction Model

The diffraction model [1] was originally proposed to predict the cross-sections for leptonic production of the π, ρ and A_1 particles under meson dominance assumptions. Simple VMD models described the electromagnetic current as a superposition of the lightest hadrons with the relevant quantum numbers. Vector dominance was successful in high energy electromagnetic interactions, particularly in photoproduction of vector mesons as illustrated in Figure 2.4. The model was consequently extended to include the weak interactions. As electromagnetic interactions are de-

scribed by the scattering of a ρ^0 meson, so weak interactions are analogously described by the scattering of a $\rho^{\pm}$.

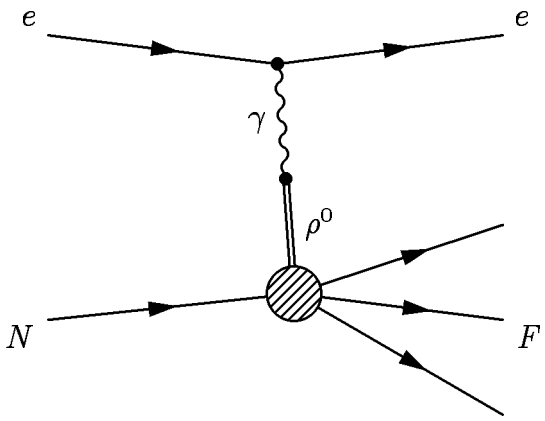

Figure 2.4: Meson dominance in electroproduction.

Some properties of the diffraction model are outlined in the following list:

- The model is restricted to large ν relative to $\sqrt{q^2}$. ie $\nu > 2\ GeV^2$ and $M_\pi^2 < Q^2 < 1.2\ GeV^2$
- Photoproduction data suggests the ω and ϕ contributions are negligible when compared to the contribution made by the ρ.
- The scattering is expressed in terms of transverse (longitudinal) polarized cross-sections $\sigma_{T(L)}$ for the incident ρ, where transverse (longitudinal) refers to the component of the spin perpendicular (parallel) to the ρ momentum.

2.4.1 Vector Meson Dominance

The idea of ρ-dominance for the vector current is now introduced into the cross-section calculations. Since CVC means the weak vector current is just an isotopic rotation of the electromagnetic current, and if the electromagnetic current at high energy is described by the scattering of a ρ^0, then one can deduce that the weak vector current is described by the scattering of a $\rho^{\pm}$.

The hadronic isovector takes the form

$$v_\mu = \frac{g_{I\rho}}{q^2 + M_\rho^2}[\delta_{\mu\lambda} + \frac{q_\mu q_\lambda}{M_\rho^2}]T_\lambda^{(\rho\to\mathcal{F})}, \tag{2.39}$$

where $\epsilon_\lambda^i T_\lambda^{(\rho\to\mathcal{F})}$ describes the production of a given hadronic state $\mathcal{F}$ by a ρ meson of mass q^2, of momentum q and polarization i. The vector meson must also obey $q_\lambda T_\lambda^{(\rho\to\mathcal{F})} = 0$. The hadronic matrix element is then given by

$$V_{\mu\nu} = \frac{g_{I\rho}^2}{(Q^2 + M^2)^2}\overline{\sum_{\mathcal{I}}}\sum_{\mathcal{F}} T_\mu^{(\rho\to\mathcal{F})}T_\nu^{*(\rho\to\mathcal{F})}. \tag{2.40}$$

The polarized cross-sections for the final state $\mathcal{F}$ for an incident ρ of longitudinal (L) or transverse (T) polarization are now introduced.

$$\sigma_T = \frac{1}{|\mathbf{q}|}T_{\mu\nu}e_\mu^T e_\nu^{*T}, \quad \sigma_L = \frac{1}{|\mathbf{q}|}T_{\mu\nu}e_\mu^L e_\nu^{*L}, \tag{2.41}$$

where $1/|\mathbf{q}|$ is a flux factor. One can consider the polarization vectors e_μ^L and e_μ^T, which have imposed upon them the conditions

$$q^\mu e_\mu^T = 0 \tag{2.42}$$

and

$$(e_\mu^T)^2 = -1, \qquad (e_\mu^L)^2 = 1 \ \ (\ Q^2 > 0). \tag{2.43}$$

The polarization vectors can now be written as

$$\begin{aligned} e^L &= \frac{1}{Q}(|\mathbf{q}|, 0, 0, \nu), \\ e^T &= (0, \sqrt{\frac{1}{2}(1+\epsilon)}, \sqrt{\frac{1}{2}(1-\epsilon)}, 0), \end{aligned} \tag{2.44}$$

where ϵ is related to the angle θ, between the polarization plane and the x axis via

$$\epsilon = 2\cos\theta - 1. \tag{2.45}$$

It is now possible to find expressions for the structure functions F_1 and F_2 using Equations 2.34, 2.41 and 2.43:

$$F_1 = |\mathbf{q}|\,\sigma_T \frac{g_{l\rho}^2}{(Q^2 + M_\rho^2)^2} \tag{2.46}$$

and

$$F_2 = \frac{g_{l\rho}^2}{(Q^2 + M^2)^2} \frac{Q^2}{|\mathbf{q}|}(\sigma_T + \sigma_L). \tag{2.47}$$

2.4.2 Cross-Section Calculation

Substituting the relations for F_1 and F_2 from Equations 2.46 and 2.47 into the equations for the cross-section 2.38, the differential cross-section now has the form

$$\frac{d^2\sigma^{(\nu\to\mathcal{F})}}{dQ^2 d\nu} = \frac{G_F^2}{4\pi^2}\frac{1}{E^2} g_{l\rho}^2 \frac{Q^2}{(Q^2 + M_\rho^2)^2}\,|\mathbf{q}|\,[\sigma_T^{(\rho^+\to\mathcal{F})} + \frac{(\sigma_T + \sigma_L)^{(\rho^+\to\mathcal{F})}}{2\,|\mathbf{q}|^2}(4EE' - Q^2)]. \tag{2.48}$$

Using the kinematical relationship

$$\epsilon = \frac{4EE' - Q^2}{4EE' + Q^2 + 2\nu^2}, \tag{2.49}$$

the weak cross-section from Equation 2.38 can be simplified to

$$\frac{d^2\sigma(\nu N \to lN')}{dQ^2 d\nu} = \frac{G_F^2}{4\pi^2} g_{l\rho}^2 \frac{|\mathbf{q}|}{E^2} \frac{Q^2}{(Q^2 + M^2)^2} \frac{1}{1-\epsilon}\sigma_T(1 + \epsilon R). \tag{2.50}$$

In this equation, g_ρ is the ρ meson decay constant, and R is the ratio between the transverse and longitudinal ρ nucleus cross-sections and is model dependent.

Based on dispersion relations, the cross-section ratio R, can be parameterized as

$$R(Q^2) = \sigma^L(Q^2)/\sigma^T(Q^2) = \xi^2 Q^2/M_\rho^2 \tag{2.51}$$

for small Q^2 values, ($Q^2 \leq 1\ GeV^2$). For real mesons, the ratio of cross-sections ξ^2

is given by

$$\xi^2 = \sigma^L(\rho)/\sigma^T(\rho) \simeq 0.4. \tag{2.52}$$

This parameterization does not hold for higher values of Q^2.

It now remains to derive a form for the transverse vector meson cross-section, σ_T. Two specific models for doing this are outlined in Sections 2.4.3 and 2.4.4.

2.4.3 The Rein And Sehgal Formulation

The hadron-nucleus differential cross-section can be expressed in terms of the hadron-nucleon differential cross-section [13] as

$$\frac{d\sigma(hN \to hN)}{d\,|t|} = A^2\,|F_N(t)|^2\,\frac{d\sigma(hn \to hn)}{d\,|t|}\bigg|_{t=0}, \tag{2.53}$$

where N refers to the nucleus and n refers to the nucleons. A is the atomic number of the nucleus and $F_N(t)$ is the nuclear form factor, which includes absorption effects.

Using the optical theorem,

$$\frac{d\sigma(hn \to hn)}{d\,|t|} = \frac{1}{16\pi}[\sigma(hn)]^2(1+r^2), \tag{2.54}$$

where r is the ratio of real to imaginary parts of the forward elastic scattering amplitude and is given by

$$r = \frac{\Re f_{hn}(0)}{\Im f_{hn}(0)}. \tag{2.55}$$

r is model dependent and is usually taken to be 0.

In this formulation the nuclear form factor from Equation 2.53 has an exponential form

$$|F_N(t)|^2 = e^{-b|t|}F_{abs}, \tag{2.56}$$

where the relationship between b and the nuclear radius R, is given by

$$b = \frac{1}{3}R^2, \qquad (R = R_0A^{1/3}), \qquad R_0 = 1.12fm. \tag{2.57}$$

The model used by Rein and Sehgal describes absorption in the nucleus in terms of F_{abs}, a t-independent attenuation factor:

$$F_{abs} = e^{-\overline{x}/\lambda} \tag{2.58}$$

where $\overline{x}$ is the average path length and λ is the absorption length. λ is defined in terms of the pion-nucleon inelastic cross-section and the nuclear density ρ. Following the method outlined in [13] one can arrive at the following expression for F_{abs}:

$$F_{abs} = \exp\left(-\frac{9A^{1/3}}{16\pi R_0^2}\sigma_{inel}\right). \tag{2.59}$$

Experimental data on coherent ρ production [47], gives $F_{abs} = 0.47 \pm 0.03$.

Substituting Equation 2.54 and Equation 2.56 into Equation 2.53 leads to the relation

$$\frac{d\sigma(hN \to hN)}{dt} = \frac{A^2}{16\pi}[\sigma(hn)]^2(1+r^2)e^{-b|t|}F_{abs}. \tag{2.60}$$

The $\sigma(hn)$ cross-section is usually chosen to be that at $\nu = E_h$.

The Resultant Cross-Section

Substituting Equation 2.60 into Equation 2.50 the resultant cross-section using the Rein and Sehgal model is

$$\frac{d^3(\nu_\mu N \to \mu\rho N)}{dQ^2 d\nu dt} = \frac{G_F^2}{4\pi^2} g_{l\rho}^2 \frac{|\mathbf{q}|}{E^2} \frac{Q^2}{(Q^2+M^2)^2} \frac{1}{1-\epsilon}(1+\epsilon R)\frac{A^2}{16\pi}[\sigma(hn)]^2(1+r^2)e^{-b|t|}F_{abs}. \tag{2.61}$$

It is claimed by Bel'kov & Kopeliovich [14] that the formula used by Rein & Sehgal [13] is wrong because it contradicts the diffraction character of πA scattering.

2.4.4 The Bel'kov And Kopeliovich Formulation

Starting with Adler's relation and parameterizing the differential cross-section in terms of the square of the transverse component of 3-momentum transfer, $\mathbf{k_T}$,

the differential cross-section can be written as

$$\frac{d\sigma}{d\mathbf{k}_T} = \left|F_N(Q^2)\right| \left.\frac{d\sigma}{d\mathbf{k}_T}\right|_{\mathbf{k}_T=0}. \tag{2.62}$$

where $|F_N(Q^2)|$ is a nuclear form factor.

Following the Glauber theory approach of Bel'kov and Kopeliovich [14], the scattering potential for high energy hadron-nucleus elastic scattering can be expressed as

$$g^{hN}(\mathbf{k}) = \frac{i\,|\mathbf{q}|}{4\pi}\int d^2b \int dz e^{i\mathbf{k}_T\mathbf{b}} e^{ik_L z}\sigma^{hn}\rho_N(\mathbf{b},z) e^{-\frac{1}{2}\sigma^{hn}\int_{-\infty}^{+\infty} dz'\rho_N(b,z')}. \tag{2.63}$$

In the heavy nuclei approximation $B_{hN} \ll R_N^2/2$, and in the limit $k_L = 0$ one can square Equation 2.63 and integrate over z such that

$$|g|^2 = \left.\frac{d^3\sigma^N}{d\mathbf{k}}\right|_{k_L=0} = \left.\frac{d^3\sigma^n}{d\mathbf{k}}\right|_{k=0} \left|\frac{2}{\sigma^{hn}}\int d^2b e^{i\mathbf{k}_T\mathbf{b}}\left(1 - e^{-\frac{1}{2}\sigma^{hn}T(b)}\right)\right|^2, \tag{2.64}$$

where the profile function of the nucleus is

$$T(b) = \int_{-\infty}^{+\infty} dz\tilde{\rho}(z,b), \tag{2.65}$$

$$\tilde{\rho}(z,b) = \int d^2b'\rho_N(z,b')\frac{1}{2\pi B_{hn}}\exp\left(-\frac{(b-b')^2}{2B_{hn}}\right). \tag{2.66}$$

$\rho_N(z,b)$ is the single-particle nuclear density and is a function of b, the impact parameter [3] and the hadron direction z. B_{hn} is the slope parameter of the cross-section for elastic scattering. All formulae were generated in the optical approximation.

Under the above limiting conditions, an exponential dependence on k_T^2 can be made such that Equation 2.64 becomes

$$\left.\frac{d^3\sigma^{hN}}{d\mathbf{k}}\right|_{k_L=0} = \left.\frac{d\sigma^{hN}}{d\mathbf{k}}\right|_{k=0} e^{-B_T\mathbf{k}_T^2}. \tag{2.67}$$

[3] $\vec{b}$ is a two-dimensional vector lying in the plane perpendicular to the z-axis and is thus interpreted as the impact parameter.

Again taking the ratio of real to imaginary parts of the forward scattering amplitude to be zero ($r = 0$), the slope is represented in terms of the impact parameter b by

$$B_T = \frac{1}{2} < b^2 >= \frac{1}{\sigma^{hN}} \int d^2b \, b^2 \left(1 - e^{-\frac{1}{2}\sigma^{hn}T(b)}\right). \tag{2.68}$$

The total pion-nucleus cross-section is described by

$$\sigma^{hN} = 2 \int d^2b \left(1 - e^{-\frac{1}{2}\sigma^{hn}T(b)}\right). \tag{2.69}$$

Physically, the slope B_T is a measure of the transverse dimensions of the nucleus, $B_T \sim A^{2/3}$.

The form factor $F_A(Q^2)$ can be written as a product of the nuclear form factor and the nucleon form factor

$$F_A(Q^2) = \tilde{F}_N(Q^2) F_n(Q^2). \tag{2.70}$$

The Glauber mechanism allows us to write

$$\tilde{F}_N(Q^2) = \frac{\sigma^{hn}}{\sigma^{hN}} \int d^2b \int_{-\infty}^{+\infty} dz e^{ik_L z} \tilde{\rho}(b,z) e^{-\frac{1}{2}\sigma^{hn}\int_z^{+\infty} dz' \tilde{\rho}(b,z')}. \tag{2.71}$$

In the limit $Q^2 \ll 2\nu/R_A$, the above Equation 2.71 simplifies to

$$\tilde{F}_N(Q^2) = e^{-\frac{1}{2}B_L k_L^2}, \tag{2.72}$$

where B_L is the square of the width of the z-distribution averaged over the nucleus,

$$B_L =< z^2 > - < z >^2 . \tag{2.73}$$

This averaging over the nuclear radius is done after consideration of absorption effects,

$$< z^n >= \frac{\sigma_{hn}}{\sigma_{hN}} \int d^2b \int_{-\infty}^{\infty} dz \; z^n \rho(b,z) e^{-\frac{1}{2}\sigma_{hn}\int_z^{\infty} dz' \rho(b,z')}. \tag{2.74}$$

The slope B_L is physically related to the cross-section of the meson in the nuclear matter on its way out of the nucleus, ie it defines the depth of the nuclear slice on which the coherence condition applies. The slope of B_L is sensitive to the parameterization of the nuclear density near the surface of the nucleus.

The nuclear density function is also model dependent and can take either the Woods-Saxon form

$$\begin{aligned} \rho(r) &= \rho_0 \left(1 + e^{\frac{r-R}{a}}\right)^{-1}, \\ \rho_0 &= \frac{3A}{4\pi R^3} \left(1 + \pi^2 a^2 / R^2\right)^{-1}, \end{aligned} \tag{2.75}$$

or the harmonic oscillator form

$$\rho(r) = \rho_0 \left(1 + \beta \left(\frac{r}{R}\right)^2\right) e^{\left(\frac{r}{R}\right)^2}. \tag{2.76}$$

Many analyses make the approximation that $b \approx B_T \approx B_L$. This assumption has no a priori physical basis but is validated experimentally for nuclei used in bubble chambers, like neon. In fact, the difference between B_T and B_L increases with A [14] as shown in Figure 2.5. B_T increases faster than B_L, because it is more directly related the radius R [6]. As carbon has a smaller nuclear radius than neon, the approximation that $B_L \approx B_T$ is even more valid for this analysis. This analysis uses carbon nuclei and the approximation $B_L = B_T = b = 56.6\ GeV^{-2}$. For ρ production, the ρ-nucleon cross-section was taken to be the same as the π-nucleon cross-section, due to a lack of direct measurement.

$$\sigma(\rho n) = \sigma(\pi n) = 24.0\ mb. \tag{2.77}$$

The relationship between t, t_{min}, k_L and k_T is given by

$$k_L^2 \approx t_{min}, \tag{2.78}$$

$$k_T^2 \approx |t| - t_{min} = t', \tag{2.79}$$

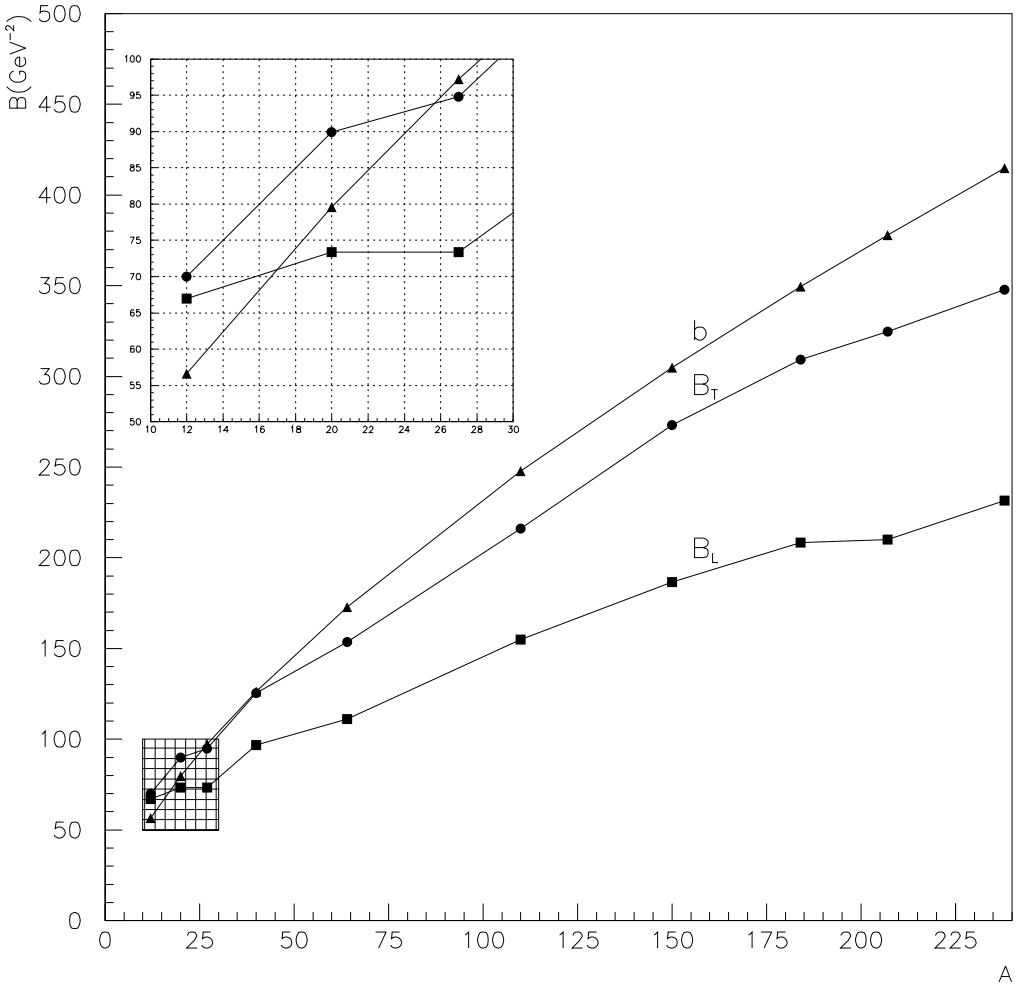

Figure 2.5: A comparison of B_T, B_L and b (from the Rein and Sehgal model) as a function of atomic number.

$$\frac{d\sigma^N}{d\mathbf{k}_T} = \left.\frac{d\sigma^N}{d\mathbf{k}_T}\right|_{k=0} e^{B_L t_{min}} e^{-B_T t'}. \tag{2.80}$$

This result was obtained using the limiting case $k_L = 0$ and $k_T = 0$, but the result is assumed to be valid for k_L and k_T as long as they remain small.

Using Adler's theorem and the optical theorem, an expression for the cross-section for coherent neutrino production can be found such that

$$\frac{d\sigma(hN)}{dk_T^2} = \frac{\left(\sigma^{hN}\right)^2}{16\pi}(1+r^2)\left|g\right|^2. \tag{2.81}$$

Substituting Equations 2.79 and 2.80 into Equation 2.81, the relation for the hadron nucleus elastic scattering cross-section can be expressed as a product of two exponentials

$$\frac{d\sigma(hN)}{dk_T^2} = \frac{\left(\sigma^{hN}\right)^2}{16\pi}(1+r^2)e^{-B_T k_T^2}e^{-B_L k_L^2}. \tag{2.82}$$

The Resultant Cross-Section

The final cross-section using this model after the combination of Equations 2.50 and 2.82 is given by

$$\frac{d^3(\nu_\mu N \to \mu\rho N)}{dQ^2 d\nu dt} = \frac{G_F^2}{4\pi^2}\frac{|\mathbf{q}|}{E^2}\frac{g_{\rho^\pm}^2}{1-\epsilon}\frac{Q^2}{(Q^2+M_\rho^2)^2}(1+\epsilon R)\frac{\sigma^2(hN)}{16\pi}(1+r^2)e^{-B_T k_T^2}e^{-B_L k_L^2}. \tag{2.83}$$

Using the approximation that $B_T = B_L = b = 56.6\ GeV^{-2}$ justified in Figure 2.5 and the above discussion, and the relationship between $\mathbf{k_T}$, $\mathbf{k_L}$ and t described in Equations 2.78 and 2.79 the cross-section can be written as

$$\frac{d^3(\nu_\mu N \to \mu\rho N)}{dQ^2 d\nu dt} = \frac{G_F^2}{4\pi^2}\frac{|\mathbf{q}|}{E^2}\frac{g_{\rho^\pm}^2}{1-\epsilon}\frac{Q^2}{(Q^2+M_\rho^2)^2}(1+\epsilon R)\frac{\sigma^2(hN)}{16\pi}(1+r^2)e^{-bt}. \tag{2.84}$$

2.4.5 Comparison of the models

Previous experiments were performed with bubble chambers mostly using neon nuclei. For these experiments, the choice of model made very little difference to the result, since numerically both models are similar and indistinguishable within

experimental uncertainty. Figure 2.6(a) shows the cross-section as a function of energy for coherent diffractive interactions from neon nuclei.

For carbon nuclei, as in the NOMAD detector, again the models are numerically similar. Figure 2.6(b) shows a comparison of the different models for coherent diffractive scattering from carbon nuclei. This plot shows the difference between the cross-section using the Rein and Sehgal model and the Bel'kov and Kopeliovich model.

As can be seen from Figure 2.6 for neutrino energies of around 25 GeV and carbon nuclei as in the NOMAD experiment, we can expect to measure a cross-section in the range $(40 \rightarrow 70) \times 10^{-40}\ cm^2$, depending on the model used. For similar neutrino energies, but on neon nuclei, as in previous CERN bubble chamber experiments, we can expect a slightly higher cross-section measurement in the range $(60 \rightarrow 110) \times 10^{-40}\ cm^2$, again the exact value depends on the model used. Thus, in changing from neon nuclei to carbon nuclei over the neutrino energy range at NOMAD a drop in the cross-section of around 40% is expected.

This chapter has outlined the coherent diffractive model beginning with a description of the diffraction mechanism, the coherence condition and hadron dominance. The kinematics of coherent diffractive scattering have been described. The theoretical cross-section has been calculated under the diffraction model to be $(40 \rightarrow 70) \times 10^{-40}\ cm^{-2}$/carbon nucleus, depending on the exact form of the model used.

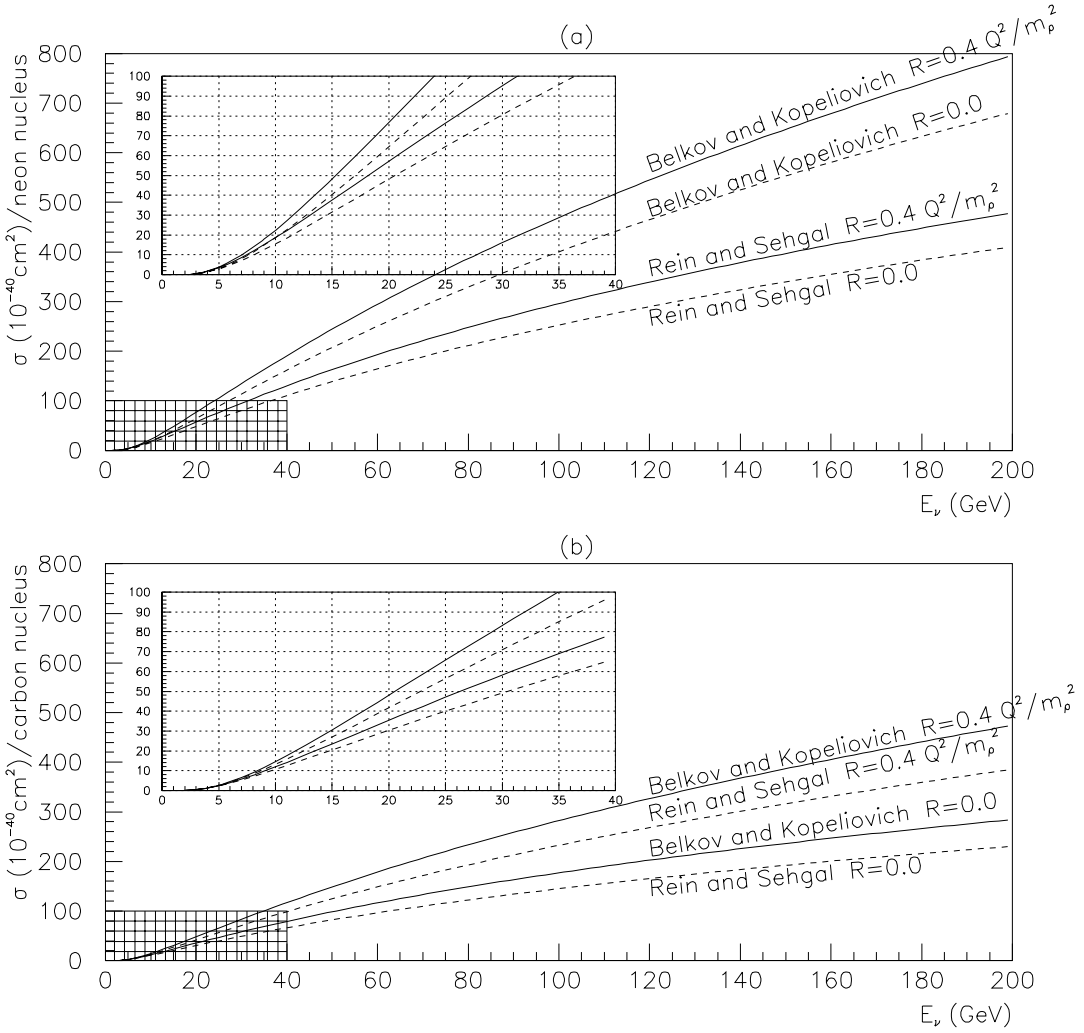

Figure 2.6: A comparison of the cross-section predictions on (a) neon nuclei and (b) carbon nuclei for different models.

Chapter 3

The NOMAD Detector and the Neutrino Beam

The NOMAD detector is shown in Figure 3.1. In the NOMAD coordinate system the x-axis is into the plane of the figure, the y-axis is towards the top of the detector and the z-axis is horizontal and approximately coincident with the neutrino beam axis. In reality, the neutrino beam points upward at an angle of 2.4^o to the z-axis.

NOMAD was primarily designed [15], [16], [17] to search for neutrino oscillations

$$\nu_\mu \overset{\nu-oscillations}{\rightsquigarrow} \nu_\tau \tag{3.1}$$

via a search for the the τ-lepton

$$\nu_\tau N \rightarrow \tau X \tag{3.2}$$

and its subsequent leptonic decays

$$\begin{aligned} \tau &\rightarrow \bar{\nu_\tau} \nu_e e, \\ &\rightarrow \bar{\nu_\tau} \nu_\mu \mu. \end{aligned} \tag{3.3}$$

NOMAD will also look for the hadronic decay modes of the τ.

The method employed in this search is one of kinematical criteria. Basically, NOMAD looks for missing transverse momentum (p_T) in an event due to the non-detection of the neutrinos from the τ decay. These decay neutrinos take a significant

proportion of the original neutrino momentum. Hence, the missing p_T from these interactions is greater than that from ν_μ charged current interactions, where the missing p_T is due to the mismeasurement of the hadron momentum vector [1], or from neutral current events, where the missing p_T is due to the missing neutrino. A careful and precise measurement of p_T is needed in order to distinguish the signal from the background.

As a result, the detector is well suited to look for a range of other neutrino interactions, in particular those that require a good measurement of missing transverse momentum, such as coherent diffractive ρ interactions.

The NOMAD detector [20], [19] consists of the following parts:

- A dipole magnet providing a 0.4 Tesla magnetic field in the x-direction.
- A forward (front) calorimeter to aid the search for heavy leptons, positioned inside the magnet support.
- A honeycomb structure target made predominantly from carbon oxygen and nitrogen. The target is interspersed with drift chambers, designed for tracking and momentum measurements and is enclosed in the magnetic field. Further details are given in Section 3.4 and in Section 4.5.2.
- A series of Transition Radiation Detector (TRD) modules, each comprising of a radiator, a detector and a drift chamber. All modules are positioned inside the magnetic field. The TRD greatly enhances the identification of electrons.
- A lead-glass Čerenkov counter electromagnetic calorimeter (E.M. Calorimeter) and preshower (PS) system, positioned at the end of the target volume inside the magnet. This is designed to measure electron energy as well as photon energy and angle from electromagnetic shower information.
- Two scintillator planes, one at the end of the target, the other in front of the preshower, provide the trigger for the detector.

[1] The hadron momentum vector is the sum of all the momenta of particles X in Interaction 3.2.

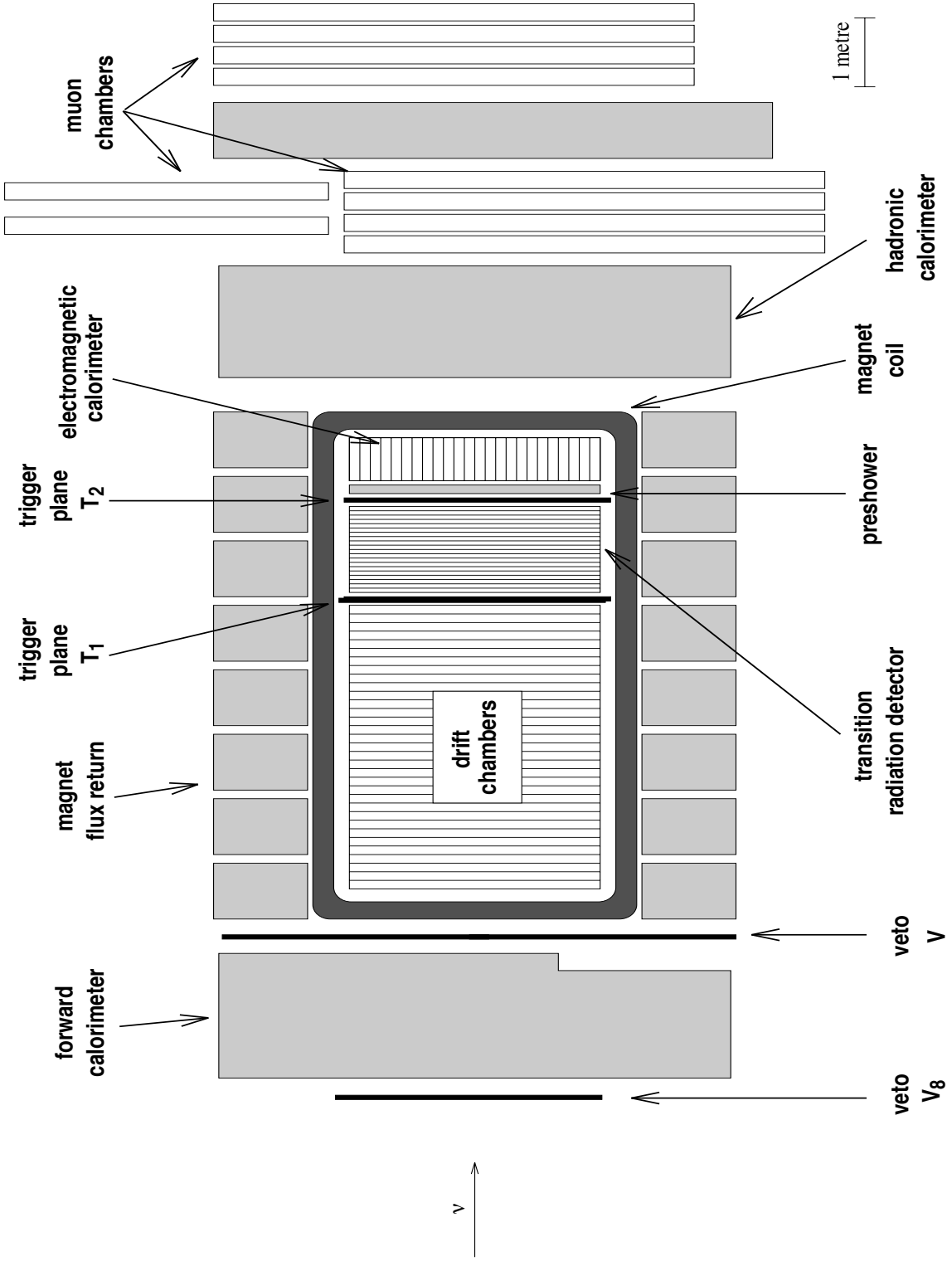

Figure 3.1: The NOMAD detector in cross-section.

- Two further scintillator planes at the front of the target area and mostly outside the magnetic field provide a veto against contamination of the neutrino beam by charged particles such as high momentum muons. The veto was designed, constructed and maintained by the Australian groups of which the author was a member.

- An hadronic calorimeter was added in 1995, with the purpose of better measuring the hadronic shower energy and hence missing p_T. This reduces inefficiencies due to "lost" neutral hadrons.

- Muon identification chambers complete the detector, being positioned at the back of the detector and outside the magnetic field.

The most important subdetectors to the search for coherent diffractive ρ are the drift chambers and the E.M. calorimeter. The drift chambers provide the momentum measurement with good resolution, for charged tracks, while the preshower E.M. calorimeter combination provides information on the energy and position of the photons from $\pi^0 \rightarrow \gamma\gamma$ decay. Events are flagged as one muon events by muon chamber information. The muon chambers are also used to help distinguish the μ from the π^+.

3.1 The Magnet

The magnet used in NOMAD was recuperated from the UA1 experiment. This magnet provides a uniform dipole magnetic field of 0.4 Tesla in the x-direction and enables NOMAD to reconstruct charge and momentum. The target and drift chambers, TRD, preshower and E.M. calorimeter are positioned inside the magnetic field, while the remaining subdetectors sit outside it.

3.2 The Forward Calorimeter (FCAL)

The forward calorimeter uses the iron in the support pillar to add additional instrumented target mass to NOMAD. The instrumentation is done by a series of scintillators interspersed inside this support.

3.2.1 Geometry

The forward calorimeter [19], [20] is made from the 23 iron plates of the support pillar of the detector. It has an area of 1750 $mm \times 1850$ mm as seen by the neutrino beam, and a thickness of 5 nuclear interaction lengths or 490 mm. Its mass is around 17.7 tons. Each plate is separated from the others by a gap of 18 mm. Scintillators are inserted in twenty of these gaps and are designed to measure the energy and position of any hadronic showers that may occur in the iron plates. Each scintillator measures 1750 $mm \times 185$ $mm \times 6$ mm, and is read out on both sides by photomultiplier tubes. Groups of five scintillators are read out together, as shown in Figure 3.2. These modules are arranged such that there are ten modules stacked vertically and four planes of modules, one behind the other with respect to the beam direction.

3.3 The Veto

The NOMAD veto has a two-fold purpose. It was designed to act as a safeguard against muons faking neutrino interactions in the target, and as a means of reducing the trigger rate from large angle cosmic rays and against charged particles produced upstream of NOMAD.

3.3.1 Geometry

The NOMAD veto is made from 59 plastic scintillators and covers an area of 5×5 m^2. The scintillators, coated with light proof black plastic, are supported by an aluminium frame situated in front of the magnet. The veto counters are

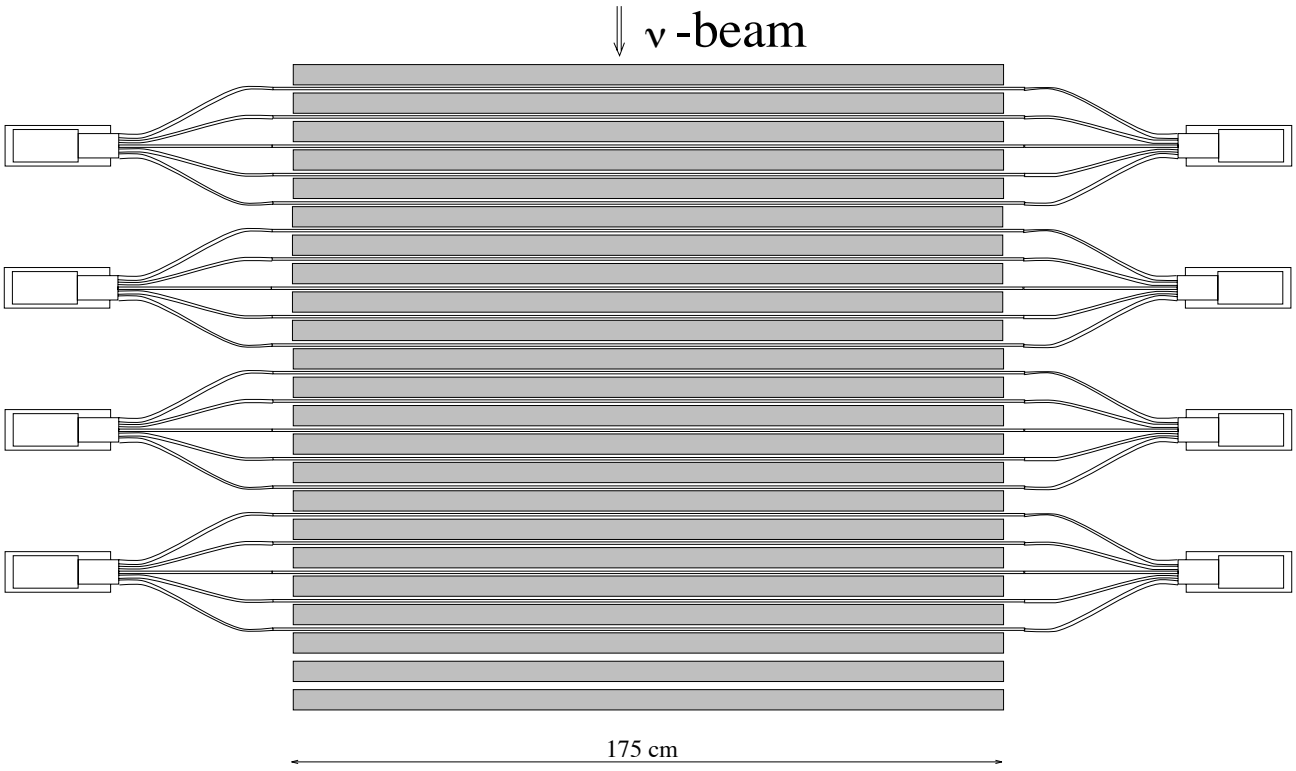

Figure 3.2: A schematic top view of the forward calorimeter.

grouped into eight banks. Figure 3.3 shows a diagram of the veto bank structure. An independent subsection of the veto, V_8 or bank 8, sits in front of the detector support, and serves as a veto for the forward calorimeter.

If a minimum ionizing particle passes through the veto, its scintillation light is collected by light guides, then detected by photomultiplier tubes positioned at both ends of the scintillator paddle.

3.3.2 Efficiency

The veto efficiency is measured using straight through muons from the muon spill, see Section 3.12 for details of the spills. A coincidence is made using CHORUS [2] the trigger planes and the muon chambers. In this way the veto efficiency was measured to be $96 - 97\%$.

3.4 The Drift Chambers (DC)

The main functions of the NOMAD drift chambers [18], [19], [20] are to provide a target for the experiment, to measure the positions of vertices and tracks in the detector and to measure track momenta. This information is then used to reconstruct the event.

3.4.1 The Target

A target, with a fiducial mass of 2.5 tonnes [3] is obtained by a combination of chambers and target. The honeycomb structured target is made from phenolic resin $(C_7H_6O)_n$ and aramide $(C_{14}H_{10}O_2N_2)_n$. The fiducial area, perpendicular to the beam axis is usually taken to be $2.6 \times 2.6\ m^2$. However, other fiducial cuts are

[2] CHORUS is an independent upstream experiment also searching for neutrino oscillations.

[3] Problems with the drift chambers during the initial stages of data taking meant that the chambers were installed in a modular fashion. During the first part of 1995 only 4 drift chamber modules were installed. Data taken from July of 1995 were taken with 8 drift chamber modules, while data taken from September 1995 had the full quota of 11 drift chamber modules. The fiducial mass described above is that for the full quota of drift chambers. However, the actual fiducial mass present during data taking periods was the mass used for the calculation of the cross section in this analysis.

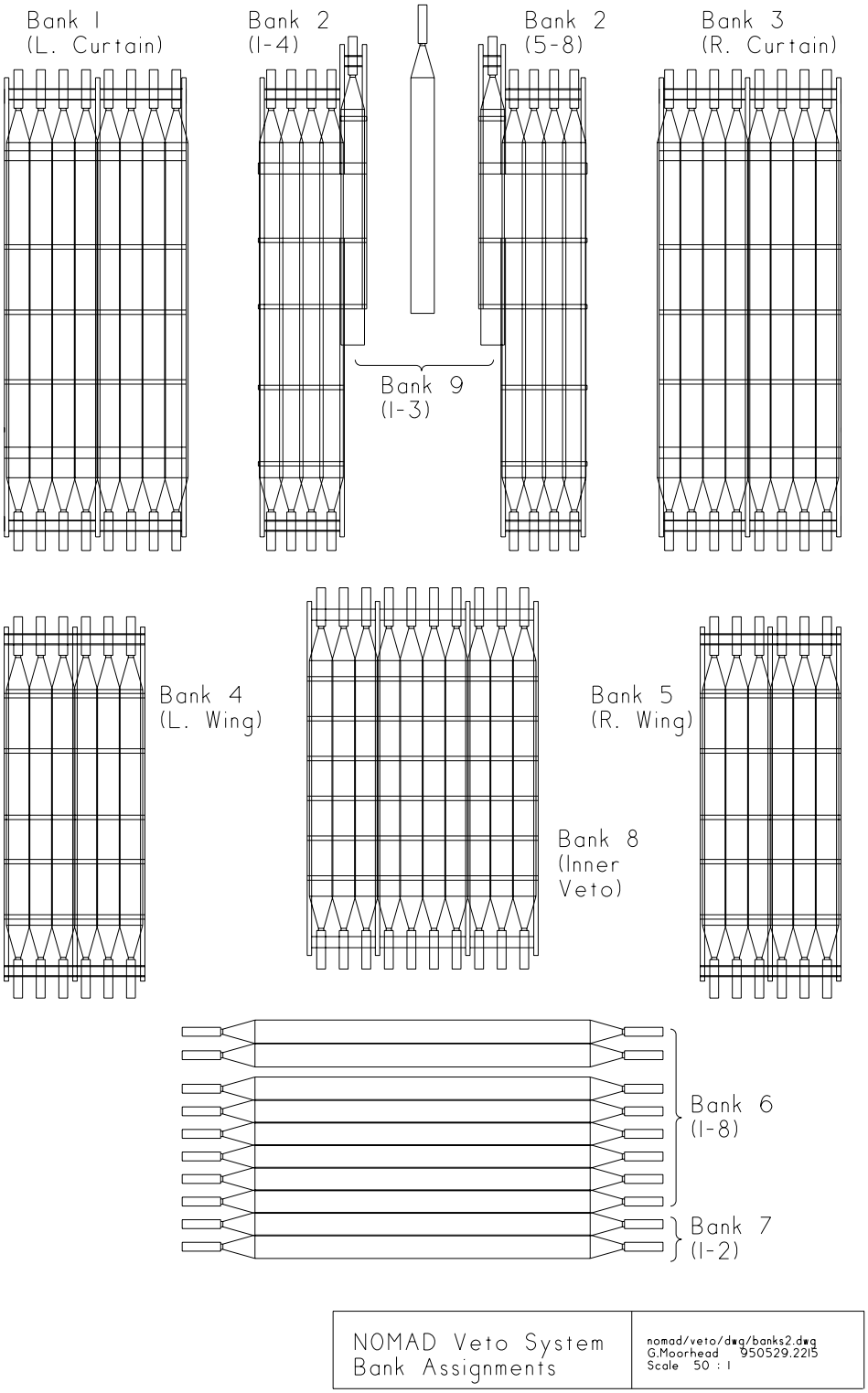

Figure 3.3: The veto layout.

sometimes applied. The target and chambers are constructed from low density, low atomic mass (Z), material thus minimizing the number of radiation lengths traversed by the interaction products. At the same time, the design maintains a significant target mass, maximizing the number of neutrino interactions.

3.4.2 Chamber Geometry

NOMAD contains 49 drift chambers in all. 44 of these chambers are arranged into 11 modules of 4 chambers each and are positioned in the front of the detector. The remaining five modules are interspersed with TRD modules.

Each chamber is made from 3 planes of sense wires, two planes being rotated with respect to the magnetic field $\vec{B}$, such that there are planes with wires at $5^o, 0^o$ and -5^o with respect to the magnetic field. Each chamber has a radiation length of $0.02X_0$ and no measurement is separated by more than $0.01X_0$. A schematic of a drift chamber is shown in Figure 3.4.

3.4.3 Resolution

These drift chambers are able to obtain a spatial resolution of 200 μm in the x or drift direction, and of 2 mm in the y direction or the direction perpendicular to the magnetic field. The active area of the chamber is restricted to

$$-130 \leq x, y \leq 130 \ cm. \tag{3.4}$$

The momentum resolution of the chambers for charged particles other than electrons is given by

$$\frac{\sigma_p}{p} \approx \frac{0.05}{\sqrt{L}} \oplus \frac{0.008p}{\sqrt{L^5}}, \tag{3.5}$$

where L is the track length in metres and p the measured track momentum in GeV/c. The first term arises from multiple scattering and the second from the single hit resolution of the chambers. For particles with momenta up to 10 GeV/c and track lengths less than 1.4 m, the multiple scattering term dominates.

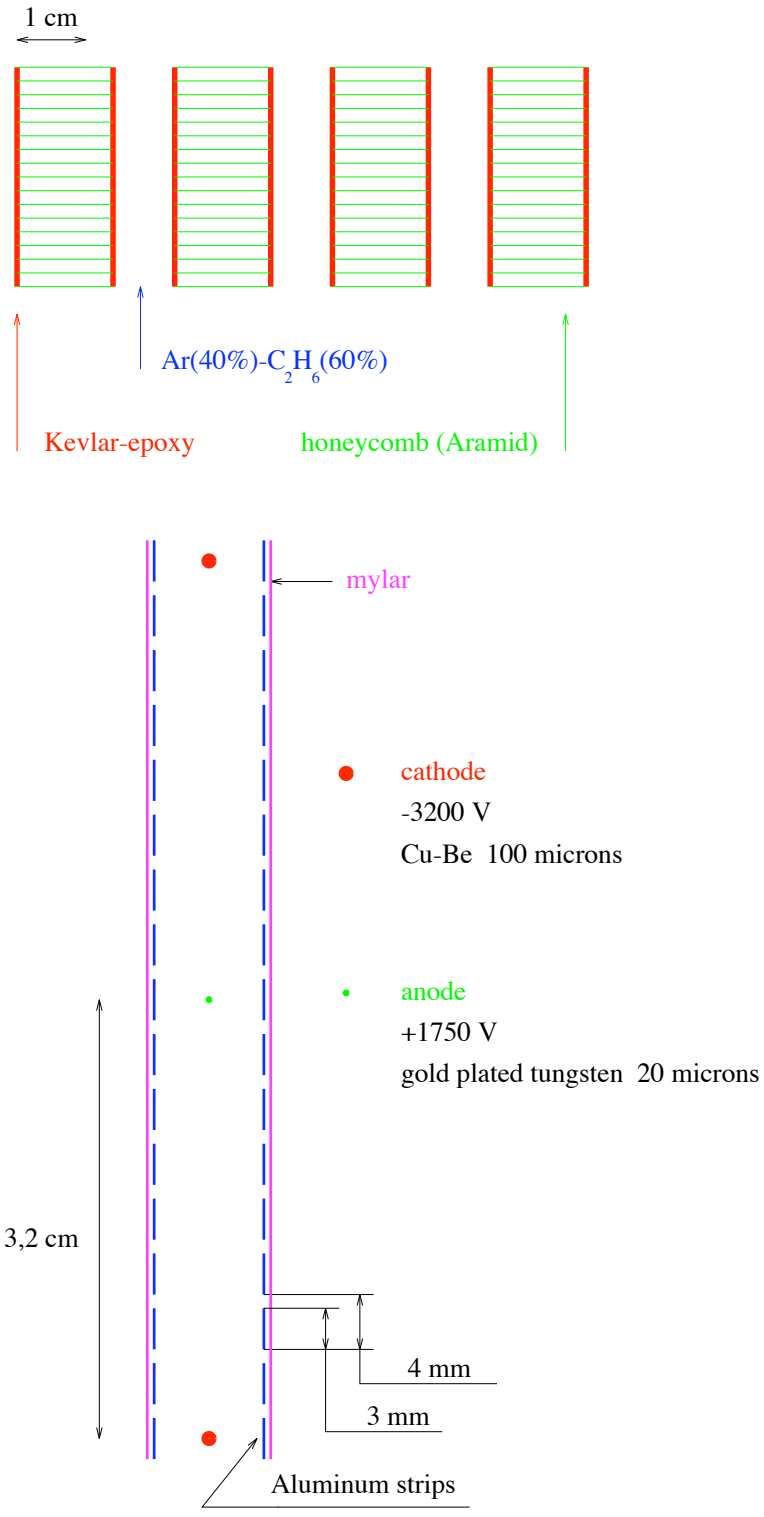

Figure 3.4: The schematic layout of the drift chambers.

3.4.4 Track Reconstruction

The drift chamber reconstruction [21] is based on building triplets, searching for a helix, collecting hits, finding a candidate track, and fitting that track using the Kalman filter. The Kalman filter is used as a method of incrementally adding points to a track. A more detailed description of the Kalman filter can be found in [22].

1. A triplet is made from three hits, one in each plane ($5^o, 0^o$ and -5^o) of a single chamber.
2. Once three triplets are found, a test is made to see if they can be fitted by a helix.
3. Once the helix is defined, a search is made for hits in a "road" near the helix.
4. An attempt is made to add hits found within this road to the track. If the hit can be included in the fit within a certain χ^2, then it is added to the hit record and the fit is adjusted accordingly.
5. Hits that can not be added to the track in this way are removed from the sample.

3.4.5 Vertex Finding and Fitting

When a particle interacts in the detector, the subsequent charged interaction products are observed as tracks in the drift chambers. In an ideal detector, i.e. one with infinite resolution, the interaction point would be coincident with the origin of these tracks. This point is known as a vertex.

In a non-ideal detector, the vertex position must be estimated from track information. Furthermore, it is not possible to know a priori which track belongs to which vertex. The vertex position and event topology are not independent and the position of the vertex will be affected by which tracks are assigned to it. If the fit on the vertex position is poor, tracks may be added to or subtracted from the

vertex in an attempt to improve the fit. This process could easily become extremly time consuming. Hence an efficient algorithm is needed to find and fit vertices.

In the method used by the NOMAD vertex software package [23] (Kalman filter method), an initial vertex is estimated. Information from the first track is then used to give a new vertex estimation. A weighted mean, a χ^2 minimization, is used to combine the two estimates. The process is repeated for each track until the final vertex position is found. With this method it is not neccessary to estimate the initial vertex position very accurately. The initial vertex is simply given a weighting of zero and consequently the vertex position is governed by the weight of the tracks. In this manner a fast and simple means of vertex fitting is performed.

The most upstream vertex is considered to be the neutrino interaction point and is known as the primary vertex. Downstream vertices are the result of interactions of products of the primary interaction and are known as secondary vertices. Vertices with no incoming track and two oppositely charged outgoing tracks are known as V^0s. These can originate from photon conversions to electron-positron pairs $\gamma \rightarrow e^+e^-$ or from decays of neutral particles to two oppositely charged particles such as $K^0 \rightarrow \pi^+\pi^-$.

Using this algorithm, it is possible to have vertices made from only one track. Furthermore, points at which tracks from charged particles are observed to stop in the detector, whether through ranging out or by interacting where the interaction products are not observed are also considered vertices.

The NOMAD drift chambers have the ability to find secondary vertices (including V^0s) down to a distance of $1cm$ from the primary vertex.

3.5 The Trigger

The NOMAD trigger planes [18] [19], [20] are made from two planes of scintillator. Various triggers can be selected and these are described more fully in Section 3.13.

3.5.1 Geometry

There are 64 scintillators of dimensions $(199 \times 124 \times 5)\ mm^3$. The scintillators are arranged into two trigger planes. Each plane presents a cross sectional area of $2.80 \times 2.86\ m^2$ to the beam.

The first plane is situated just after the target and before the TRD, the second just after the TRD and before the preshower. Adiabatic light guides take the scintillation light from the trigger to magnetic field resistant *(proximity mesh) HAMAMATSU R2490-05* photomultipliers. These photomultipliers operate with about 70% of the response they would have without a magnetic field.

3.5.2 Efficiency

The trigger efficiency for each plane is measured by counting the coincidences between hits in the muon chambers and hits in the veto. The trigger operates with an average efficiency of $97.5 \pm 0.1\%$ for single tracks, and with an efficiency greater than 99.5% for multiple track events.

3.6 The Transition Radiation Detector

A transition radiation detector [18] [19], [20] was installed in NOMAD with the aim of distinguishing electrons from other charged particles produced by neutrino interactions. It utilizes the principle that when a relativistic particle traverses a junction of two materials with different dielectric constants, transition radiation photons are emitted. The amount of transition radiation emitted is inversely proportional to the mass of the particle, and so is greatest for light particles such as electrons. Transition radiation X-rays from electrons are detected by a detection plane.

3.6.1 Geometry

The TRD is made from 9 modules. Each module is made from a radiator followed by a detection plane.

The radiator is made from 315 polypropylene foils, each 15 μm thick and separated from the next by an air gap of 250 μm. As an electron passes through the TRD, a few photons with energy in the KeV range are produced for every air gap.

The detection plane consists of 176 vertical *straw tubes*, each tube being 3 m long and having a diameter of 16 mm. The tubes are made from mylar ribbon and are filled with a gas mixture of 80% Xe and 20% CH_4. This gas mixture was chosen because it has a large cross-section for photons in the expected energy range.

Eight TRD modules are arranged into four groups. A group is formed by two TRD modules and a drift chamber. These four groups are followed by the remaining TRD module, which in turn is followed by five more drift chambers. The TRD is calibrated by the use of an Fe^{55} ($E_\gamma = 5.89KeV$) source.

Electron Identification and Efficiency

Electron identification in the TRD [20] is based on the "likelihood ratio" method. This method uses the difference in energies deposited in the straw tubes by charged particles of different Lorentz factors ($\gamma = E/mc^2$). Heavier particles with small Lorentz factors, such as pions, deposit energy in the straw tubes mostly by ionization losses. Lighter particles with large Lorentz factors, such as electrons emit transition radiation X-rays as they traverse the radiator.

Electrons are identified by calculating a likelihood ratio for each reconstructed TRD track. The likelihood ratio, Equation 3.6 is a function of the energy deposited in the i^{th} straw tube of the TRD (ϵ_i), and of the probability density functions ($P(\epsilon|e)$) and ($P(\epsilon|\pi)$) of an electron and a pion of given momentum to deposit the energy ϵ_i in the i^{th} straw tube. These probability functions must be calculated a priori for all possible detector and particle parameters. In the case of NOMAD they were obtained from Monte Carlo TRD simulations. More detail on the TRD

electron identification algorithm can be found in [39].

$$LH = \sum_{i=1}^{N} log \frac{P(\epsilon_i|e)}{P(\epsilon_i|\pi)} \tag{3.6}$$

The likelihood threshold value is set according to what pion contamination is acceptable or to what electron acceptance is required. The TRD is able to obtain a rejection factor against pions of $\approx 1.6 \times 10^4$ for an electron efficiency of 90%.

3.7 The Preshower

The preshower [18], [24], [19], [20], has two main purposes. The first purpose is to distinguish, in conjunction with the TRD and elctromagnetic calorimeter, between pions and electrons. The method used to achieve the π/e separation was to instigate an electromagnetic shower by the use of a lead converter, and then to detect and to measure this shower using a detector made from proportional tubes. A distinction occurs because electrons and photons have a high probability of initiating an electromagnetic shower, whereas pions have a low probability of interacting.

The second purpose of the preshower is to give a better spatial resolution on electromagnetic showers. The proportional tubes are a factor of 10 narrower than the lead-glass blocks used in the E.M. calorimeter. Hence it has a significantly better spatial resolution.

3.7.1 Geometry

The converter is made from two planes $(2.880 \times 2.880)\ m^2$ of lead-antimony $(96\%Pb, 4\%An)$. Each plane is $4.5\ mm$ $(1.6X_0)$ thick. The planes are separated by a $2\ mm$ thick aluminium support plane.

Directly behind the converter, after an air gap of $4\ mm$, sit two planes of proportional tubes. One plane consists of 288 vertically orientated tubes. The other consists of 286 horizontal tubes. The vertical plane is $2.89\ m$ long while the horizontal is $2.92\ m$ long. The tubes are square with dimensions of $9\ mm \times 9\ mm$

and are filled with a gas mixture of $80\%Ar$ and $20\%CO_2$. Each tube has a tungsten anode of 30 μm diameter. The anode is set to a potential of around $+1500\ V$, which gives a gain of ~ 2000. These planes are separated by an aluminium support piece of thickness $2\ mm$. Figure 3.5 shows a diagrammatic outline of the preshower.

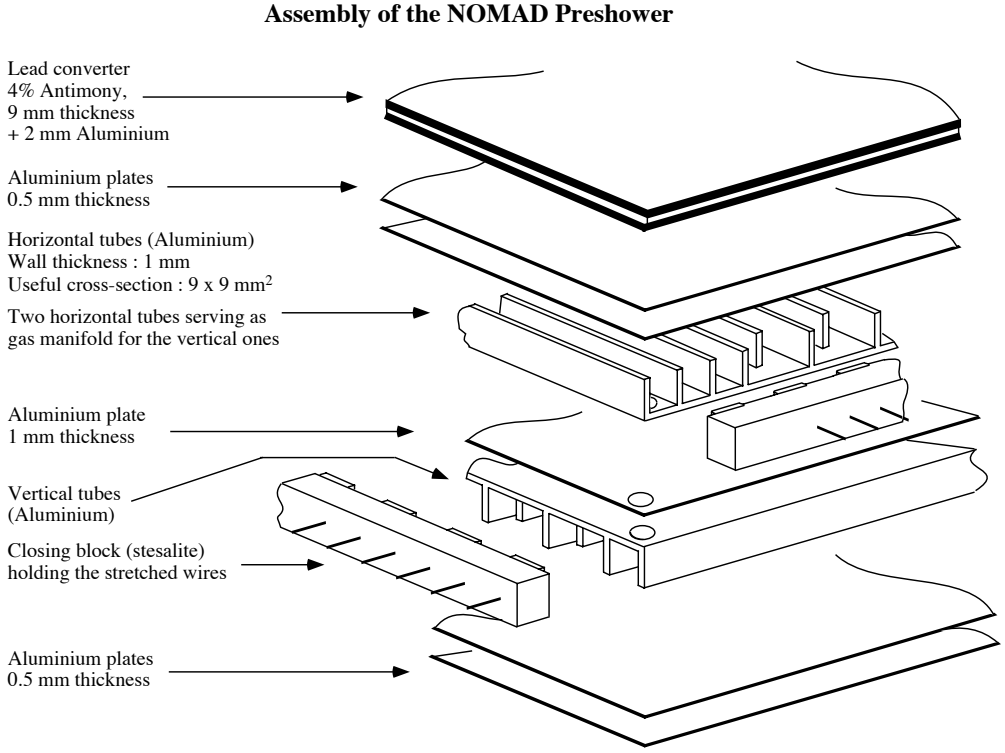

Figure 3.5: A schematic of the NOMAD preshower.

3.7.2 Performance

Tests have shown that the preshower alone is able to distinguish electrons from charged pions with an efficiency of 90% while maintaining a pion contamination of less than 10%. Once information from the E.M. calorimeter is added, the pion contamination is reduced to 4×10^{-4}.

The spatial resolution of the preshower can not be measured directly, but is estimated [20] to be 10 mm. Consequently, it is possible to measure the position of electromagnetic showers with a resolution of 10 mm.

3.8 The Electromagnetic Calorimeter

The E.M. calorimeter [18], [20], [25] was built to measure the energy of photons and electrons, and in combination with the preshower, to determine the position and direction of the photons. This measurement is discussed further in Section 4.3.2.

3.8.1 Geometry

The calorimeter consists of 875 lead-glass Čerenkov counters of dimensions $(79 \times 112) \times 500\ mm^3$. Each block is $(19X_0)$ deep. These blocks are arranged so they cover an area of $(2.8 \times 2.8)\ m^2$ in a plane perpendicular to that of the beam direction.

This calorimeter is positioned after the TRD and inside the magnetic field. To overcome the problem of the magnetic field, the face of each block was cut at an angle of 45^o with respect to the field, and then coupled to the photo-tetrodes using an epoxy resin with a refractive index $n = 1.484$ at $589\ nm$. This gave an increased response factor as well as increased mechanical stability when compared to a purely mechanical coupling. Figure 3.6 shows the E.M. calorimeter structure more explicitly.

3.8.2 Calibration

The energy response of the electromagnetic calorimeter was calibrated using a 10 GeV/c electron beam. The beam was centered on each tower and 3000 electron counts were taken in coincidence with a trigger. Some anti-coincidences were also taken in order to measure the pedestals of the towers. The calibrated energy for each tower i is given by

$$E_i = \alpha_i ADC_i, \tag{3.7}$$

where ADC_i are the pedestal subtracted signals and α_i are the calibration constants. A full description of the calibration is given in [26].

The electromagnetic calorimeter response is monitored by the use of blue

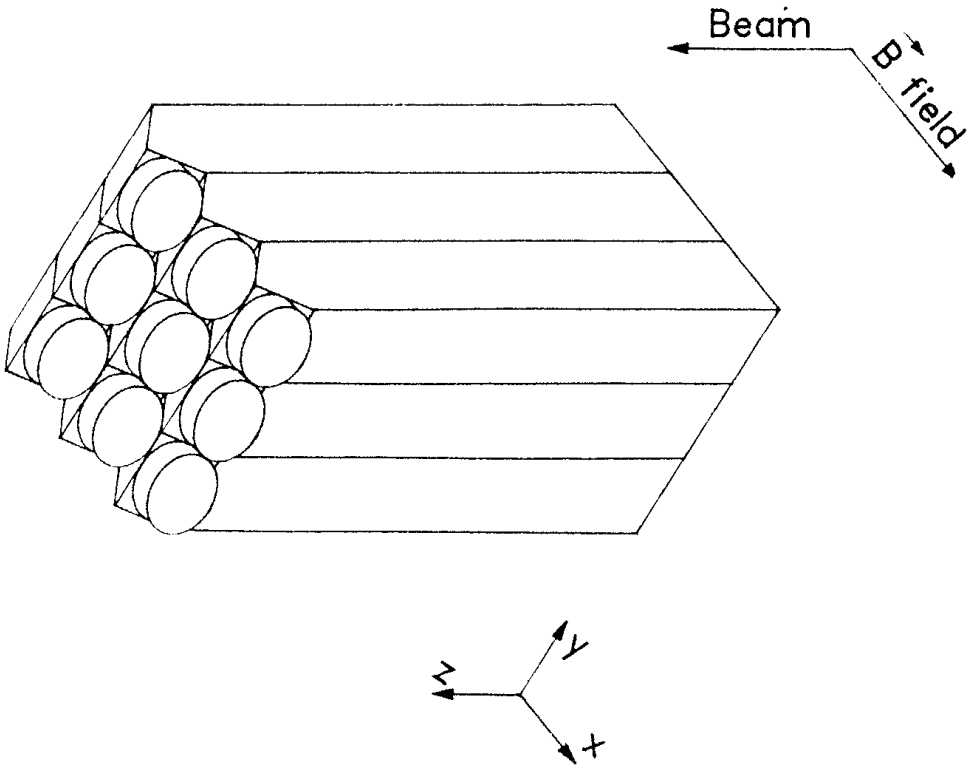

Figure 3.6: The Electromagnetic Calorimeter Structure

LEDs. The response was found to be uniform to within 1% over the whole face of the block. The stability has been shown to be better than a few parts in a thousand over periods of several months.

3.8.3 Energy Resolution

The energy resolution of the E.M. calorimeter is affected by [27]:

- fluctuations in the energy deposition in the E.M. calorimeter ($1.2\%/\sqrt{E}$)
- the number of photo-electrons detected
- the lateral energy leakage
- the longitudinal energy leakage (0.8% at 80 GeV)
- the intrinsic noise of the electronic chain (≈ 11 MeV per tower).

The energy resolution of the NOMAD E.M. calorimeter is described by a two parameter fit such that

$$\frac{\sigma(E)}{E} = (a + \frac{b}{\sqrt{E}})\% \tag{3.8}$$

where E is in GeV, $a = (1.04 \pm 0.01)$ and $b = (3.22 \pm 0.07)$.

3.8.4 Linearity

To detect deviations from linearity, a lead-glass module was exposed to an electron beam of energies in the range from 1.5 to 80 GeV. The total deposited energy was examined as a function of the beam energy. If the relationship were purely linear then $E_{measured} = \alpha E_{deposited}$. However, two significant contributions to the deviation from linearity were observed.

- Light produced by a electromagnetic shower will be attenuated on its path to the photocathode due to absorption in the lead-glass. The further an electromagnetic shower is from the photocathode, the more it will be attenuated.

Since the longitudinal profile of an electromagnetic shower depends on its energy, this suggests a nonlinear increase with energy in the detector response. Thus this non-linearity is corrected by applying the following:

$$E' = \frac{E}{1 + 0.038 \log \frac{E}{10}}. \tag{3.9}$$

where $E(GeV)$ is the energy released by the particle, $E'(GeV)$ is the cluster energy (a cluster is defined below in Section 3.8.5) and $\epsilon = 0.038$ is the fitted parameter. After application of this correction, the response of the calorimeter to normally incident particles is linear to less than 1% for all energies in the normal NOMAD operating range.

E GeV	E' GeV
5	5.06
10	10.00
20	19.77
40	39.10

Table 3.1: The non-linear response of the calorimeter.

- The angle at which the particle entered the calorimeter. Since the calibration as described above is only valid for particles incident normally to the face of the E.M calorimeter, a correction needs to be applied for particles incident away from this normal. This correction was measured up to 20 degrees and applied up to 26 degrees:

$$E' = \frac{E}{\sqrt{cos\theta}}. \tag{3.10}$$

θ is the incident angle of the particle with respect to the tower's axis.

3.8.5 The Electromagnetic Calorimeter Clustering Algorithm

Energy in the E.M. calorimeter is measured via the cluster energy. A cluster [28] is a collection of adjacent calorimeter cells satisfying the following conditions:

- A cell must have a minimum of CELMIN (10 MeV) deposited in it in order to be considered as part of a cluster.
- The seed cell used to build the cluster is the first cell found in the cell bank with energy above a given threshold, CLSMIN (= 30 MeV).
- All adjacent cells with energy above CELMIN are added to the cluster.
- The cluster building stops when no other adjacent unused cell is found.
- The cluster is kept if it has a total energy above a threshold CLSMIN, allowing the possibility of clusters with only one cell.
- The cluster centroid is computed using the centre of gravity method, while the cluster radius is found by computing the standard deviation of the distribution.

3.9 The Hadronic Calorimeter (HCAL)

The hadronic calorimeter [18] is used to detect neutral hadrons, which would be otherwise undetectable, as they leave only a small part of their energy in the electromagnetic calorimeter. It is also designed to find photons, whose energy is mixed in with that of charged particles in the E.M. calorimeter. This detector is important to the search for neutrino oscillations as an aid to reducing background from missing p_T, but is not used in this analysis and so is only described breifly here.

3.9.1 Geometry

The hadronic calorimeter, located downstream of the E.M. calorimeter, is built from the iron endcaps of the magnet, interspersed with long scintillator paddles which are read out at both ends. The iron serves as an absorber for the hadronic calorimeter and the scintillator as a sampler. The position of the hadronic shower is found in the vertical direction by looking at which scintillator was hit, and in

the horizontal direction by the ratio of pulse heights at each end coming from that paddle.

There are 23 longitudinal layers of scintillator in the HCAL. The first is before the first iron layer, followed by one in each gap in the endcap. Each layer is made from 20 paddles of dimensions 184 mm. The total active area of the HCAL is $(3.5 \times 3.9)\ m^2$.

3.9.2 Resolution

The energy resolution of the HCAL is given by

$$\frac{\sigma(E)}{E} \leq \frac{1.2}{\sqrt{E}}. \tag{3.11}$$

In the vertical direction, the resolution is limited by the physical size of the paddles and so $\delta y \sim 20\ cm$. In the horizontal direction, the position resolution is typically 20 cm. In this direction, the limitation to the resolution is caused by photon statistics, ie the amount of scintillation light generated.

3.10 The Muon Chambers

In NOMAD, muons are identified via a series of muon chambers [18],[19],[20].

3.10.1 Geometry

There are ten chambers in all, filled with an argon 40%, ethane 60% gas mixture. Each chamber has the dimensions $(3.75 \times 5.55)\ m^2$ and has four wire planes, two each in of the vertical and horizontal directions. All together, there are 1210 drift cells. Each drift cell has a maximum drift distance of 70 mm.

The chambers are arranged into five pairs for the purpose of track reconstruction. The first station, consisting of three pairs, is placed behind the magnet return yoke which serves as an iron absorber (8 interaction lengths thick). The second station, consisting of the two remaining pairs of chambers, is situated behind

an 800 mm (13 interaction length) iron wall. Figure 3.1 more clearly shows the position of the muon chambers.

3.10.2 Performance

The NOMAD muon chambers have a position resolution of 400 μm in both the vertical and horizontal directions. It is also possible to measure momentum of tracks in the muon chambers, though of course not as accurately as tracks measured in the drift chambers. Muon momenta are estimated in the muon chambers from the amount of multiple scattering in the iron wall, the scattering angle being inversely proportional to the track momentum. This method requires that the muon be energetic enough to reach the second muon station.

3.10.3 Reconstruction

If both muon stations record some in-time hits, then track segments are reconstructed individually for each station, using typically three or four hits per projection. The measured efficiency for track segment reconstruction is 97%.

Once two track segments are reconstructed, an attempt to reconstruct muons was made using the following algorithm [29]:

- For each track segment in the first station, a partner in the second was searched for.
- If a partner is found, the tracks from each station were extrapolated to the centre of the iron wall between them.
- The angular and spatial mismatch between them were calculated.
- The angular mismatch between the two tracks was used to estimate the muon momentum, assuming this mismatch is due only to multiple scattering in the iron wall.
- Using this estimate of muon momenta from the angular mismatch, tracks were

extrapolated back to the central detector and matched with a drift chamber track.

- The drift chamber information then gives an accurate meausure of the muon momentum.

If only one muon station records some in-time hits, then a muon can still be reconstructed. In this case:

- The track segement is extrapolated back to the central detector.
- The drift chamber information then gives a meausure of the muon momentum.

Muons with a momentum greater than 2.3 GeV/c have at least a 50% probability of being measured in the front muon chambers. Muons with momentum greater than 3.7 GeV/c have a more than 50% chance of being measured by the rear chambers. Figure 3.7 illustrates this point.

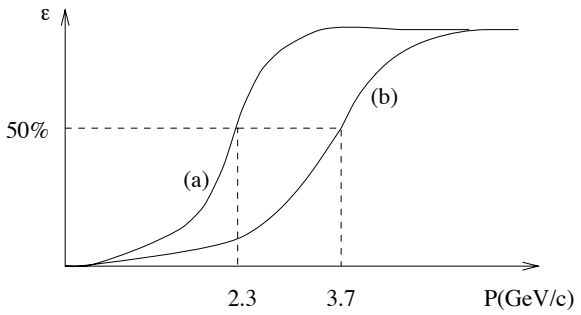

Figure 3.7: The efficiency for detecting muons. Line (a) represents the probability (ϵ) for a particle of momentum P to be detected in the first muon station. Line (b) represents the same probability for the second station.

The reason some muons of a given momentum will reach the muon chambers whereas others will not is due to two reasons. The first is the angular distribution of the muons. Some muons will exit the side of the detector whereas others will pass straight through to the muon chambers. The second reason is the distribution of interaction points in the detector. Muons arising from interactions near the start of

the detector will have a lower probability of reaching the muon chambers than those arising from interactions near the end of the detector. These points are discussed in some detail in Section 4.3.1

3.11 An Example Of A Reconstructed Event In NOMAD.

Figure 3.8 shows an example of a real candidate ν_μ charged current event ($\nu_\mu N \rightarrow \mu X$) as reconstructed by NOMAD. Three views are shown, the detector as seen from the side (YZ view), the top (XZ view) and the front (XY view). In this diagram, tracks are represented by lines. E.M. Calorimter clusters are represented by small "spikes" in the top and side views and in the front view by shading of the lead-glass cells.

The muon candidate is clearly seen. It is the only track to traverse the whole detector and to pass through the iron walls to leave a signal in the muon chambers. The energy deposited in the E.M. calorimeter by this muon can be seen as the cluster at the same position as the muon track in the calorimeter.

A potential photon conversion ($\gamma \rightarrow e^+e^-$) can be seen in the side view towards the middle of the detector. Two oppositely charged tracks appear from the same secondary vertex.

A potential neutral particle, for example a photon, can be seen as the other cluster in the E.M. calorimeter. This energy deposition does not have an associated charged particle track.

3.12 The Neutrino Beam

3.12.1 The West Area Neutrino Facility (WANF)

The CERN Super Proton Synchrotron (SPS) [30], [20] provided a wide band neutrino beam for the NOMAD experiment. Figure 3.9 shows a schematic diagram of the layout of the WANF beam line.

The CERN SPS runs on a 14.4 s cycle. Two extractions of the 450 GeV

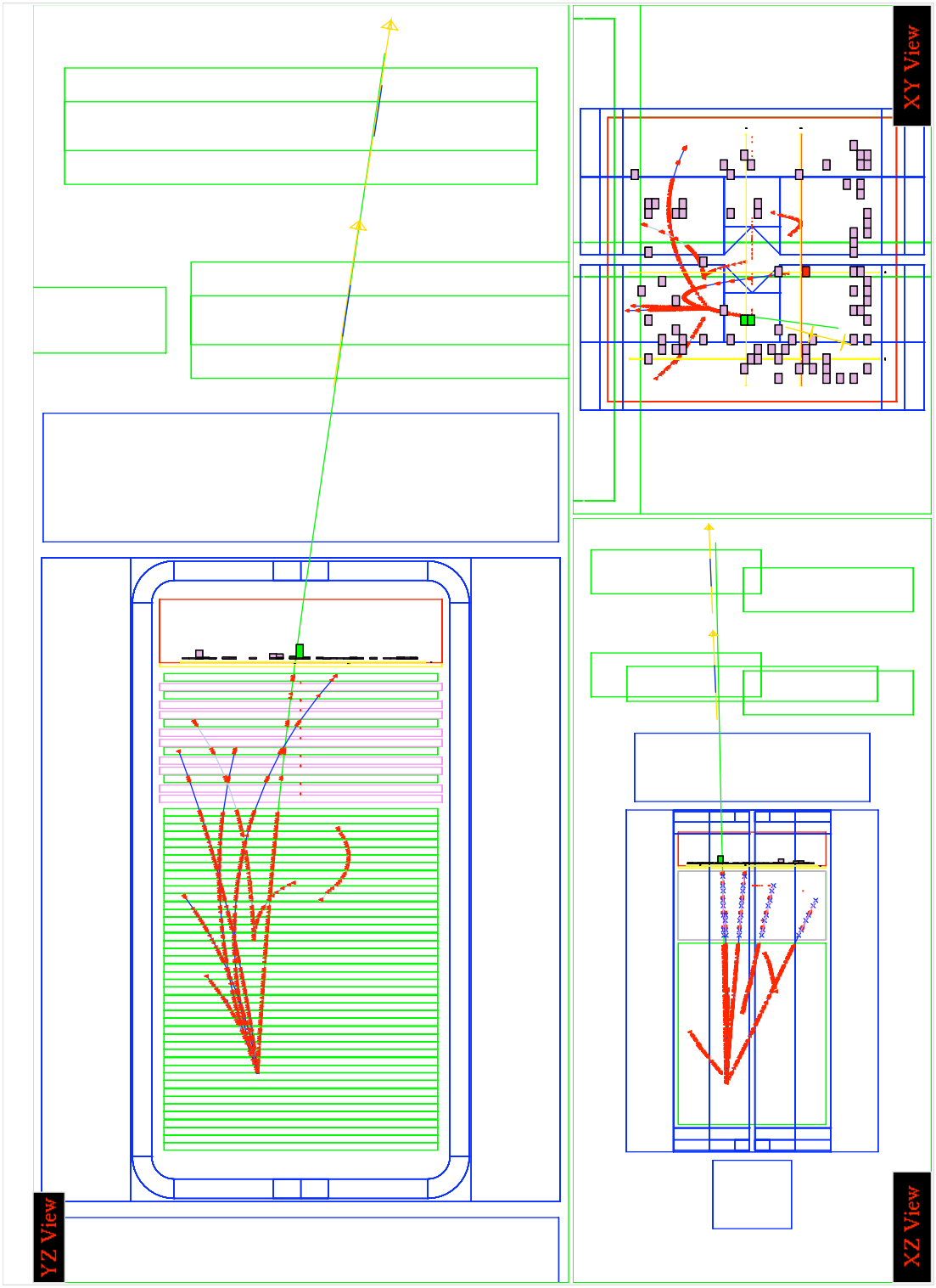

Figure 3.8: A reconstructed candidate ν_μ charged current event in NOMAD.

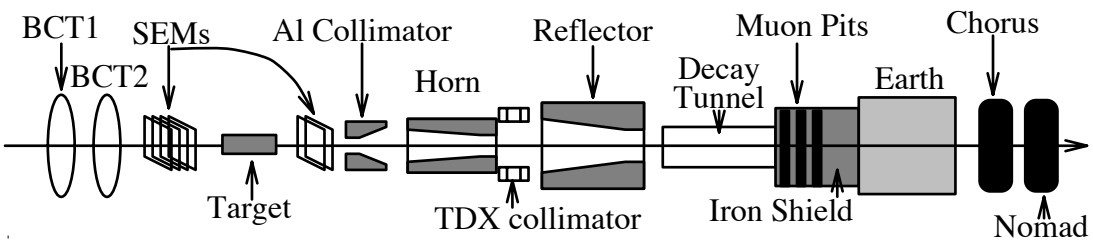

Figure 3.9: A Schematic layout of the WANF beam line.

proton beam are made in two spills (fast/slow extraction) at either end of a $2.6s$ long energy flat top, Figure 3.10 shows a schematic representation of the SPS cycle. During the two 4 ms spills, the proton beam impinges upon a Be target. The target is made from 11 Be-rods each 3 mm in diameter and 10 cm long. Each rod is separated from the next by a distance of 90 cm.

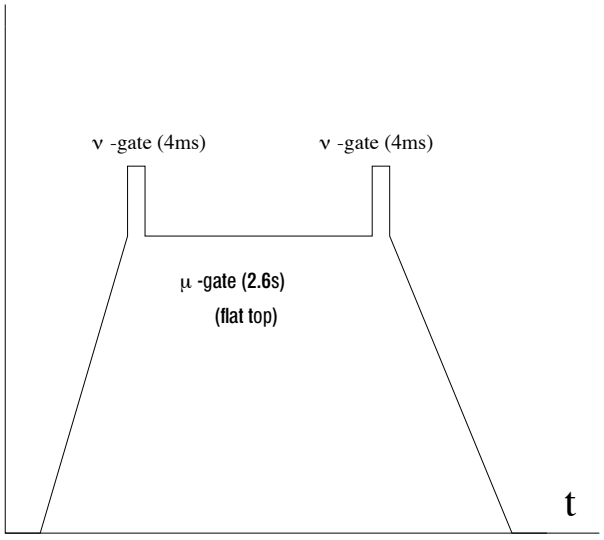

Figure 3.10: A schematic diagram of the timing of the neutrino beam.

The secondary pions and kaons produced in the proton-berillium interaction are then focused using the magnetic horn and reflector. This system operates in such a way as to focus particles of one sign, while defocusing particles of the opposite sign. The pions and kaons decay inside a vacuum decay tunnel, $\pi^+ \rightarrow \nu_\mu \mu^+$ for example, to provide neutrinos. The muons from this decay are removed from the

beam by allowing the beam to pass through a shield of earth and iron. Any muon surviving this shield is deflected away from the beam via another magnet, leaving a relatively pure neutrino beam. The NOMAD detector is placed 400 m from the end of the decay tunnel (835 m from the end of the target).

3.12.2 The Beam Constituents.

The neutrino beam was simulated by the GBEAM [31] package. GBEAM was able to accurately predict the neutrino energy spectrum and flux at NOMAD. While the beam consists mainly of muon type neutrinos, a certain percentage of anti-muon as well as electron type neutrinos can also be found. Table 3.2 [20] summarizes the ratios of these types of neutrinos. Figure 3.11 shows the simulated neutrino energy distributions for all types of neutrinos found in the beam.

Neutrino type	$\overline{E_\nu}$	Relative abundance	ν CC events
ν_μ	24.4	1.00	1.15×10^6
$\overline{\nu_\mu}$	24.1	0.07	0.39×10^5
ν_e	41.5	0.01	0.17×10^5
$\overline{\nu_e}$	30.4	0.003	0.22×10^4

Table 3.2: The Monte Carlo prediction for the ratio of the different neutrino types found in the West Area neutrino beam and the corresponding event numbers, assuming 2.4×10^{19} protons on target and a fiducial area of $2.6 \times 2.6\ m^2$.

3.12.3 Neutrino Beam Performance

The data used for this analysis were taken from the 1995 8-module and 11-module data taking periods. The measured number of protons on target ($p.o.t$) and the number of neutrinos expected at NOMAD (calculated from the beam Monte Carlo) for each data taking period are summarized in Table 3.3.

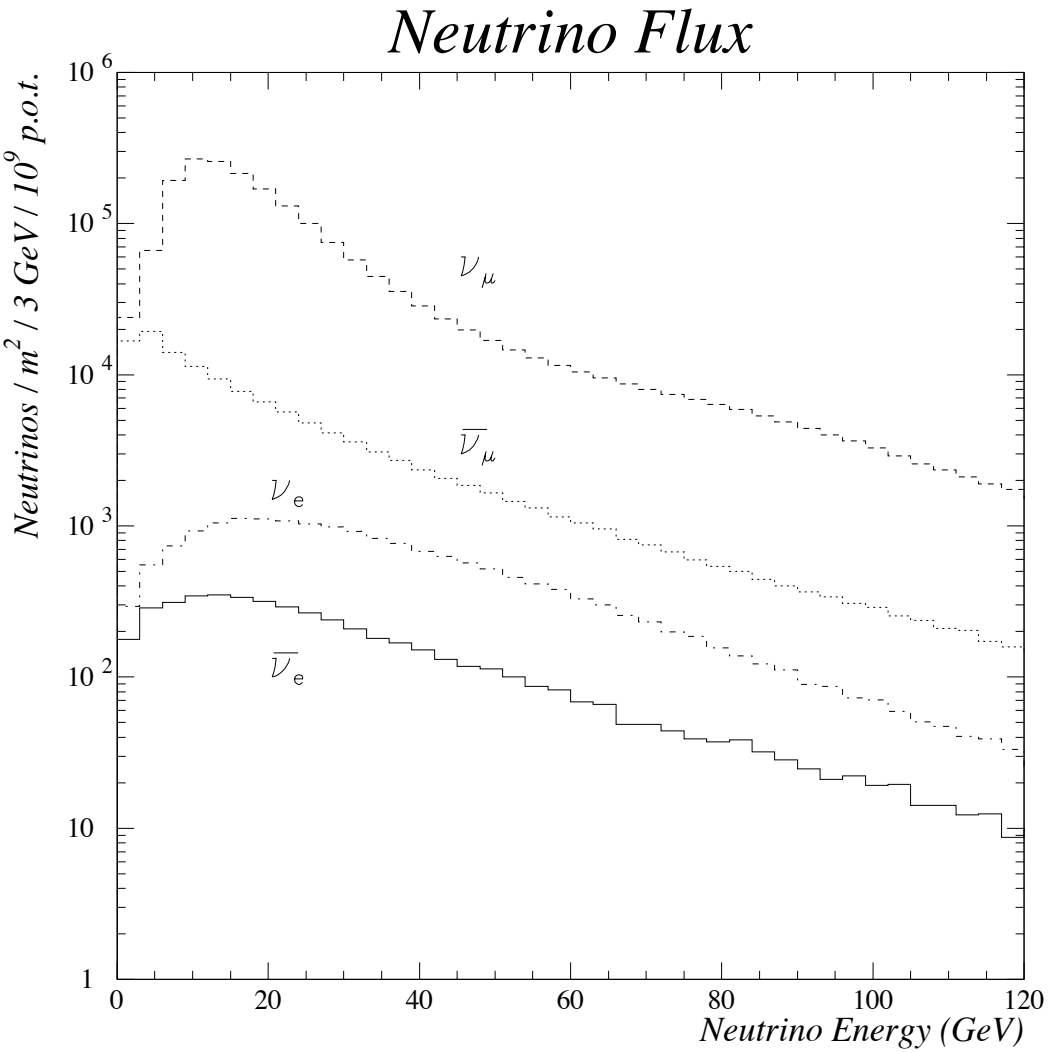

Figure 3.11: The neutrino energy spectrum as predicted by the GBEAM Monte Carlo package.

Data	Protons on Target	ν_μs at NOMAD
4-module	2.80×10^{18}	2.86×10^{16}
8-module	3.35×10^{18}	4.25×10^{16}
11-module	3.03×10^{18}	3.84×10^{16}
This work	6.38×10^{18}	8.09×10^{16}

Table 3.3: A summary of the WANF beam performance in 1995. (The number of neutrinos at NOMAD is taken for a fiducial area of $2.6 \times 2.6 m^2$)

3.13 NOMAD Triggers

A number of different triggers were used throughout the duration of the NOMAD experiment. The physics triggers were those that occurred during either of the two neutrino gates (see Figure 3.10):

1. $T_1 T_2 \overline{V}$
2. $\overline{V} E_{cal} > 1\ GeV$
3. $\overline{V_8} F_{cal}$
4. $\overline{V_8} T_1 T_2 F_{cal}$.

Calibration triggers for the drift chambers, TRD and preshower were taken during the muon gate:

1. $V T_1 T_2$
2. $V T_1 T_2 E_{cal}$,

where $T_{1,2}$ means an in time hit in the first or second trigger plane respectively. $\overline{V}$ means there was no hit in the veto. $\overline{V_8}$ means there was no hit in the central subsection of the veto. E_{cal} implies that there is some energy deposited in the electromagnetic calorimeter. F_{cal} is an in time hit in the forward calorimeter.

The $T_1 T_2 \overline{V}$ triggers acquired during the neutrino gates passing any of the following cuts below are recorded.

- $T_1 * T_2 = 1$
- $ECAL > 1\ GeV$
- (number of TRD planes with 1 hit) < 7

For this analysis, it was sufficient that trigger number 1 was satisfied.

Chapter 4

Data Analysis

This chapter deals with the analysis of the candidate events for a coherent diffractive ρ signal. The data samples under investigation are described. The Monte Carlo simulation algorithm and parameters are outlined. The search for the signal, including the particle identification method and the cuts implemented are summarized. A study of potential backgrounds to the signal is performed and a background estimate is given. The results of the investigation are shown. The fit done to the t'-distribution is explained and other kinematic distributions are examined. The cross-section of the coherent ρ signal is calculated. Comparisons between this analysis, theoretical predictions and previous analyses are made.

4.1 The Data Samples

Two data and three Monte Carlo samples were considered in this analysis.

- **Data**
  - **8-module**

    The data taken in July 1995 with only 8 drift chamber modules. This data sample contained 194,673 events.
  - **11-module**

    The data taken in September 1995 with the full 11 drift chamber modules. This data sample contained 214,848 events.

A total of 409,521 data events were considered in this analysis.

The 11-module sample had more available target, hence for the same number of protons on target, it would contain more events. However, the samples also differ in that the 11-module sample had a drift chamber alignment of a higher precision.

- **Monte Carlo**
  - **Coherent Diffractive ρ**
    $10,000$ coherent diffractive ρ events were simulated. Section 4.2.1 describes the method used to generate these events.
  - **Δ-Resonance Monte Carlo**
    Used for background studies. See Section 4.4.1 for a description of the generation of these events. A sample of 1942 events were studied.
  - **Deep Inelastic Charged Current**
    A sample of $132,064$ charged current deep inelastic scattering events. Section 4.4.2 gives a description of the generation of these events. During the data taking periods examined during this analysis, approximately $140,000$ ν_μ charged current events were expected.
- **A combination of data and Monte Carlo**
  - A sample of candidate Δ^{++} events in the data were transformed into Δ^{+} for background studies. Section 4.4.1 gives the details of this procedure. A total of 870 events were transformed in this manner.

All the data samples (8-module, 11-module, Monte Carlo and data-Monte Carlo combinations) were reconstructed using the NOMAD reconstruction code version recon63 [33].

4.2 The Monte Carlo Simulation of Coherent ρ

The Monte Carlo simulation of coherent diffractive events consisted of two parts. Firstly, the event generator specifically written by the author for this analysis

was used to generate events with kinematic distributions reflecting those expected under the diffraction model described by Piketty and Stodolsky [1].

The second phase of the simulation dealt with detector effects. This part was performed using the standard NOMAD simulation package, GENOM [34], based on the CERN detector simulation package GEANT [35]. Section 4.2.2 gives a brief description of GENOM.

4.2.1 The Event Generator Algorithm

NEGLIB [36] is a Monte Carlo simulation package designed specifically to simulate deep inelastic scattering in NOMAD. The deep inelastic scattering event generation in NEGLIB is done by LEPTO [37].

LEPTO incorporates the generation of the incident neutrino energy and vertex position, chooses the target quark/nucleon according to the NOMAD specific geometry and performs some analysis of the event at the generator level. It also allows the selection of specific channels, for example only charged current events. This event generator was used to create the Deep Inelastic Scattering (DIS) Monte Carlo sample used for background studies.

A coherent diffractive ρ event generator was written by the author and placed in the NEGLIB framework, replacing LEPTO as the event generator. The steps used to generate these events are described below.

- The ρ mass (M_ρ) was generated using the following procedure.
  - Points in the M_ρ, $f(M_\rho)$ plane were generated uniformly within the limits

$$2m_\pi \leq M_\rho \leq 2M_0 \tag{4.1}$$

and

$$0 \leq f(M_\rho) \leq \left(\frac{2}{\Gamma}\right)^2 \tag{4.2}$$

where $M_0 = 0.770\ GeV$ is the centroid and $\Gamma = 0.150\ GeV$ is the width of the distribution.

– The ρ mass was accepted if the generated point lay below

$$f(M_\rho) = \frac{1.0}{(M_\rho - M_0)^2 + (\frac{\Gamma}{2})^2}. \tag{4.3}$$

Figure 4.1 shows a plot of $f(M_\rho)$ vs M_ρ. Random points in this plane are shown. If any point falls below the function described in Equation 4.3 and drawn in Figure 4.1, then it is accepted and the ρ mass for this event is given by M_ρ at this point. If it falls above this line it is rejected.

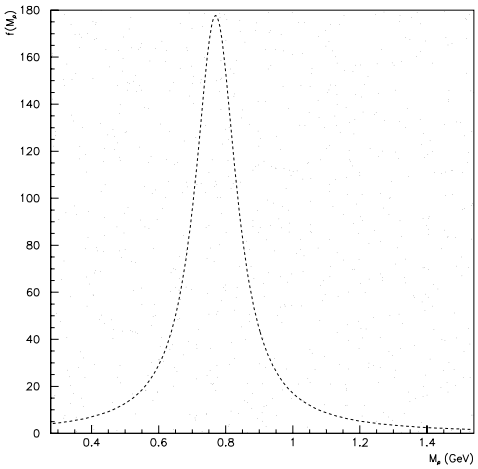

Figure 4.1: Masses are accepted or rejected depending on where they fall on the M_ρ, $f(M_\rho)$ plane.

– The resultant Breit-Wigner mass distribution is shown in Figure 4.2.

- The neutrino energy (E_ν) and interaction point was selected by the GBEAM [31] package. Studies [32] have shown that GBEAM accurately represents the neutrino energy spectrum at NOMAD. Figure 3.11 shows the energy spectrum of the neutrinos as predicted by GBEAM.

- The minimum centre of mass energy squared of the hadronic system, $S_0^{min} = (M_N + M_\rho)^2$, was calculated. The nuclear mass M_N was set to be that of

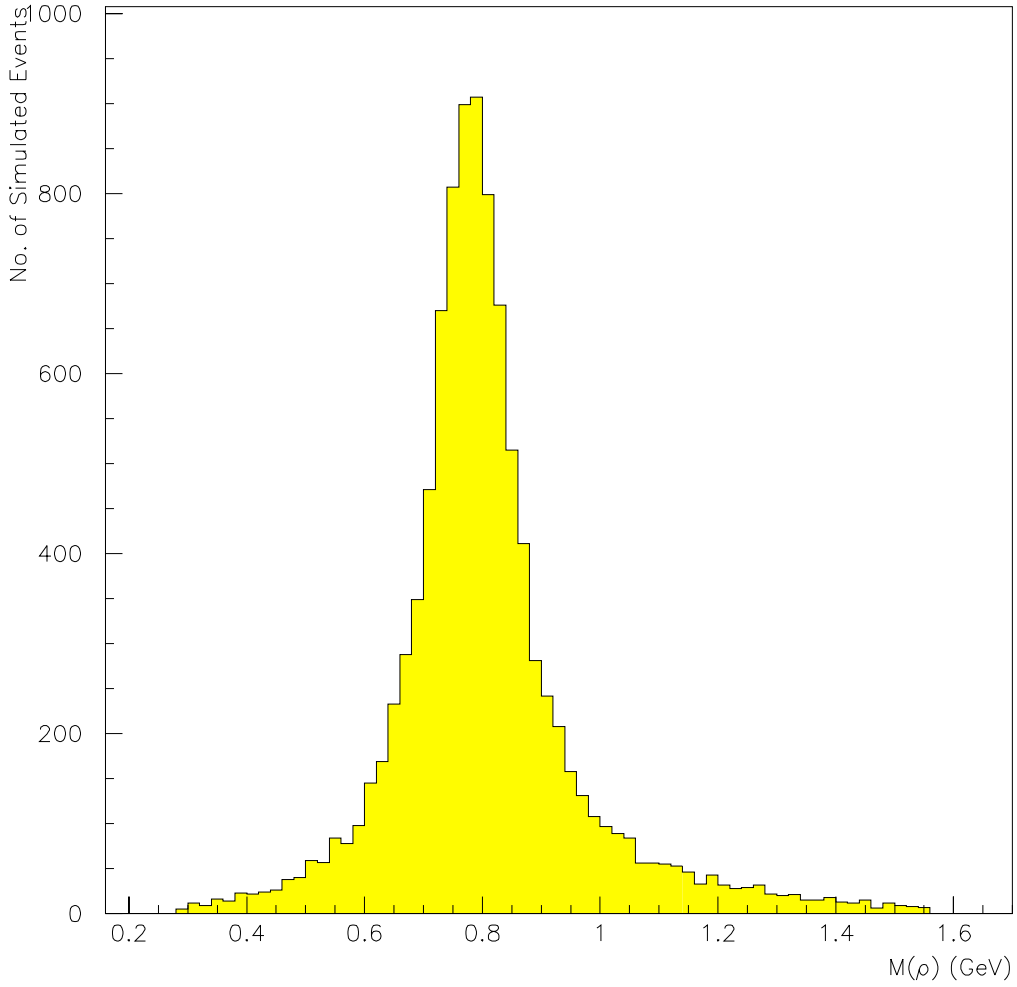

Figure 4.2: The generated ρ mass.

carbon, since carbon is the main component of the target. Section 3.4 gives more details on the target.

- The Bjorken variables x and y were uniformly generated within their kinematic limits. Section 2.2.1 gives a discussion of these limits.

- The kinematic variables Q^2, W, ν, t_{min} and t_{max} were calculated from E_ν, x and y.

- The t-independent part of the cross-section σ was calculated using the given kinematics and the final term in Equation 2.84.

- The event was accepted or rejected using the following principles, known as importance sampling. (This procedure was already used in generating M_ρ according to a Breit-Wigner distribution.)

  - A 3-dimensional (Q^2, ν, σ) space was conceptualized. Since this space is 3-dimensional any equation relating these three variables will define a surface in this space.

  - Points in this volume were selected randomly and uniformly.

  - If a given point in this kinematical space fell below the surface defined in Equation 2.84 it was accepted.

  - This process was repeated until an acceptable point, i.e. an event, was found.

- t was generated with an exponential distribution of slope $b \sim A^{2/3} = 56.6\ GeV^{-2}$, where A is the atomic mass of the nucleus, via the equation:

$$t = \left| \frac{1}{b} \times ln(R) \right| \tag{4.4}$$

where R is a random number uniformly distributed from zero to one. Section 2.4.4 explains the choice of this value of b.

- This leads to a cross-section such that

$$\frac{d\sigma}{dt} \sim e^{-bt}. \tag{4.5}$$

- t was constrained to be within the kinematical bounds

$$t_{min} < t < t_{max}. \tag{4.6}$$

  Section 2.2.1 gives an explanation of these bounds.

- The momenta of all the particles involved in the interaction were calculated from the relevant kinematic quantities.

- The ρ was made to decay into two pions,

$$\rho^+ \rightarrow \pi^+\pi^0. \tag{4.7}$$

  The π^0 decay was modelled by the GENOM [34] package.

- All momenta were rotated from the beam frame into the detector frame. They were then expressed in format readable by GENOM.

The Monte Carlo was generated with all 11 drift chamber modules, whereas the data was a combination of 8 and 11-module samples. In order to best simulate the data each Monte Carlo event was given a weighting according to the z-position of the primary vertex. Events with z-primary vertex less than 110 cm were weighted by 0.47. Events could only occur in this region of the target during the 11-module data taking period. All other events were given a weighting of 1.00, since modules in this part of the detector were present for both 11-module and 8-module data taking periods. See Figure 4.3 for the manifestation of this combination of two data samples and histogram weighting.

4.2.2 Detector Simulation

GENOM [34] is based on the GEANT [35] package. It is used to simulate the effect of the detector on the Monte Carlo data. This program tracked particles through NOMAD simulating physics processes such as bremsstrahlung, Compton scattering and energy loss. Detector specific conditions were also simulated here, for example the NOMAD magnetic field map. This part of the simulation replicated detector inefficiencies and finite resolution etc. It also converted energy deposition and detector responses to measurable quantities such as ADC counts. GENOM gave an output identical in format and as similar as possible in content to that given by the real detector. This output was then reconstructed and analyzed in the same way as the real data.

4.3 The Search for the Coherent ρ Signal.

In order to distinguish coherent diffractive ρ events from the much more numerous background events a series of cuts and selections were made. The selection process is based on the premise that coherent ρ events will consist of only a muon, a charged pion and a neutral pion. The selection process is outlined below.

4.3.1 Preliminary Analysis Filter.

A low multiplicity filter was applied to all the data samples. This quickly reduced the amount of data requiring further processing. It is summarized by the following cuts:

1. The primary vertex[1] was required to be inside the sensitive volume.

$$-140 < x < 140 \; cm \tag{4.8}$$

[1]The primary vertex is ideally the interaction vertex. For the purpose of reconstruction this was taken to be the most upstream vertex of the event, excluding the end vertices of particles traveling backwards from the interaction vertex. Section 3.4.5 gives a more detailed description of the vertex reconstruction algorithm.

$$-140 < y < 140 \ cm \tag{4.9}$$

$$0 < z < 400 \ cm \tag{4.10}$$

This cut ensures events with an interaction vertex inside the magnet ends and supports do not contaminate the data sample. Figure 4.3 shows the distribution of the primary vertices within the boundaries described above. A discussion of these plots is given below.

2. No more than six tracks were reconstructed.

$$N_{tracks} \leq 6 \tag{4.11}$$

Six is the maximum number of tracks a clean coherent ρ event can have (one muon track, one charged pion track and four electron tracks from two gamma conversions).

3. At least two tracks were required.

$$N_{tracks} \geq 2 \tag{4.12}$$

Two is the minimum number of tracks a clean coherent ρ event can have (one muon track and one charged pion track).

4. The sum of the charges on all tracks must be consistent with the hypothesis that the event contains one muon, one charged pion and two photons.

Figure 4.4 shows the track multiplicity of the coherent ρ Monte Carlo compared to that for the deep inelastic scattering Monte Carlo sample, normalized to the same number of events. Clearly, the coherent ρ sample has a much lower multiplicity.

As explained above, coherent ρ events should have no more than six tracks. However, the Monte Carlo sample contains some events with higher than expected multiplicity. Examination of the Monte Carlo at the particle level reveals that the

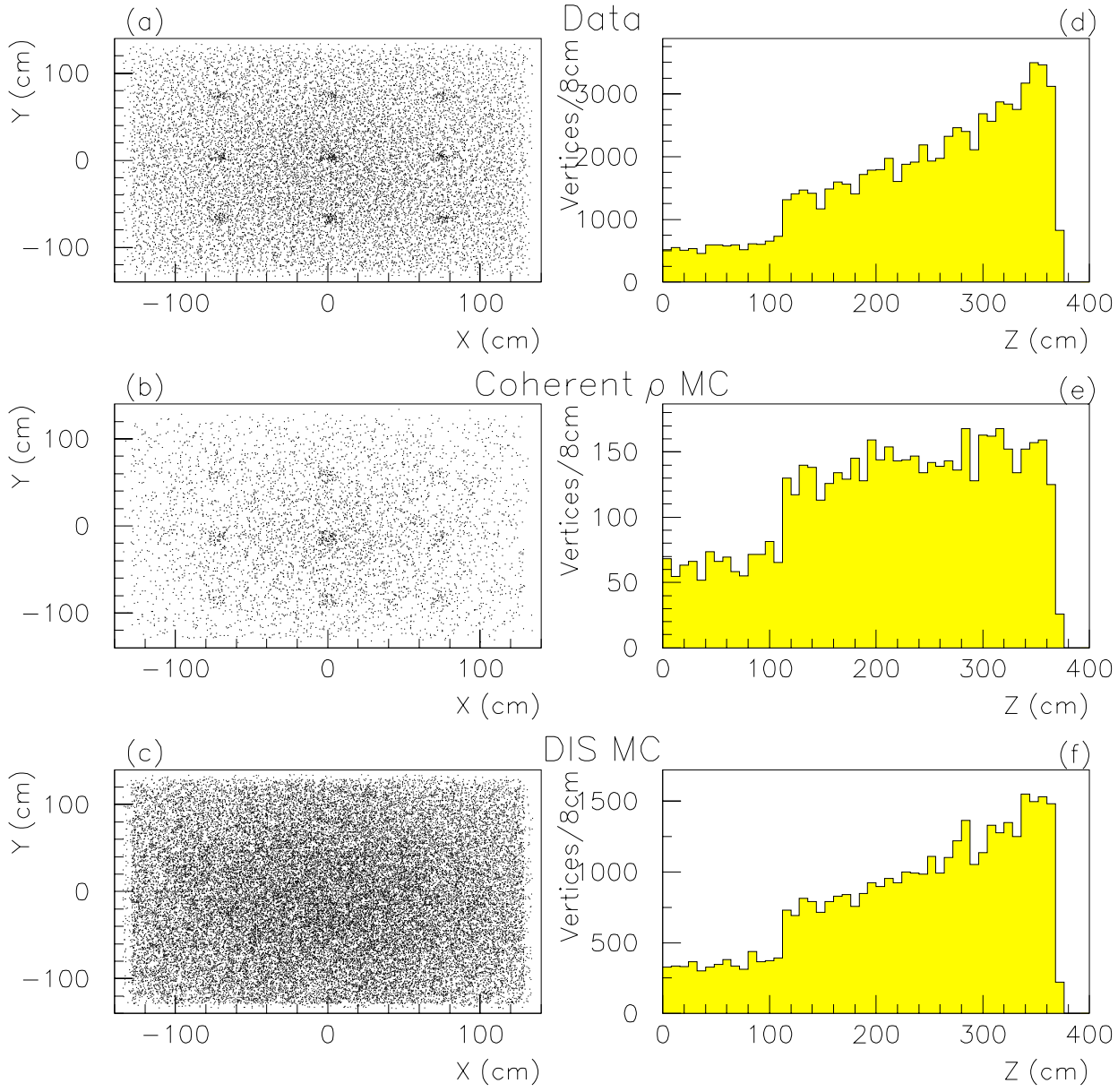

Figure 4.3: The position of the primary vertex. The left hand column shows the position of the vertex in the plane transverse to the beam direction. The right hand column shows the position of the vertex in the direction of the neutrino beam. (See text (Section 4.3.1) for a discussion of these plots.)

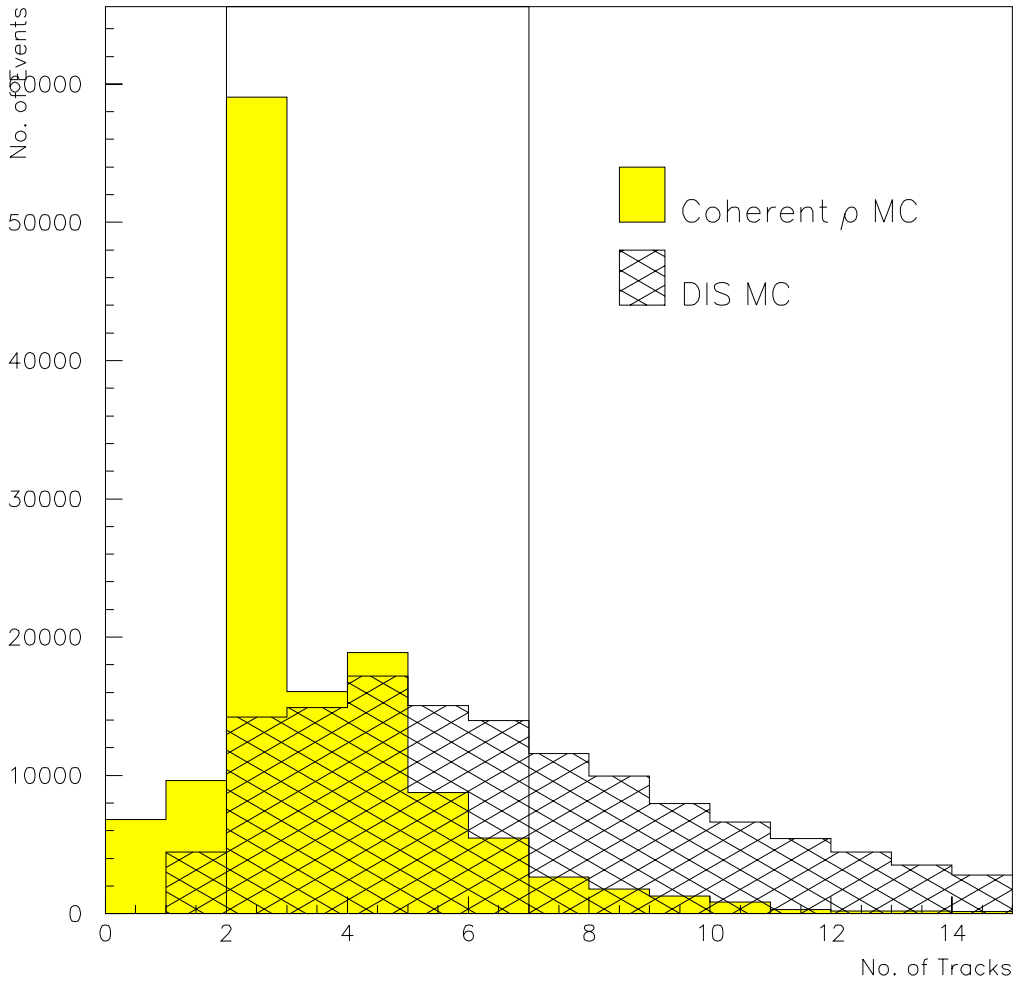

Figure 4.4: The number of reconstructed tracks per Monte Carlo generated event.

majority of excess tracks are caused by the re-interaction of the charged pion in the target. Other high multiplicity events are caused by poor track reconstruction i.e. breaking one track into two track segments.

In plots throughout this chapter, the Monte Carlo histogram has been normalized to have the same number of events as the data for each plot.

Comments on the Primary Vertex Distribution.

The vertex distribution effectively acts as an "X-ray" of the detector. In the case of real data, as shown in Figure 4.3 (a), it is possible to see nine regions of increased vertex activity. These regions correspond to the nine spacers used to give mechanical rigidity to the drift chambers. These supports were included in the simulation of the detector and can also be seen in Figures 4.3 (b) and 4.3 (c).

The shape of the z-vertex distributions for all data samples can be explained in terms of the detector geometry and the event kinematics. To an extremely good approximation, neutrinos have a uniform probability of interacting at any z in the detector. For simplicity, consider a Deep Inelastic Scattering event with just two resultant charged particles, such as any of those shown in Figure 4.5. If one of the particles were to travel with zero angle in the forward direction, it would traverse both trigger planes and the event would be recorded independent of the z-position of the interaction vertex. However, if both particles were to have significant transverse momenta, the probability of the event triggering would increase the closer the interaction point was to the trigger plane. Correspondingly, the trigger efficiency decreases as the distance between the primary vertex and the trigger planes increases.

The same principles hold for coherent ρ interactions. However, these events are high ν, low Q^2 events. Consequently, muons from coherent ρ events tend to have a larger forward momentum than those from Deep Inelastic Scattering events. Figure 4.6 shows a comparison of transverse muon momenta $p_T(\mu)$ for Deep Inelastic Scattering and coherent ρ Monte Carlos. This figure illustrates the difference in

the transverse momentum distribution of the muon between these two different interaction mechanisms.

Figure 4.3 (d) shows the z-vertex distributions for data. Figure 4.3 (e) shows the z-vertex distributions for coherent ρ Monte Carlo. Figure 4.3 (f) shows the z-vertex distribution for Deep Inelastic Scattering Monte Carlo. Clearly the distribution for the coherent ρ Monte Carlo is flatter than that for the deep inelastic scattering Monte Carlo. The data, dominated by deep inelastic scattering events, mimics the Deep Inelastic Scattering events with fewer events at low z.

The step reduction in the number of events with $z \leq 110\ cm$ is a result of the missing modules in the 8-module data sample. The Monte Carlo events were weighted to imitate the effect of these missing modules.

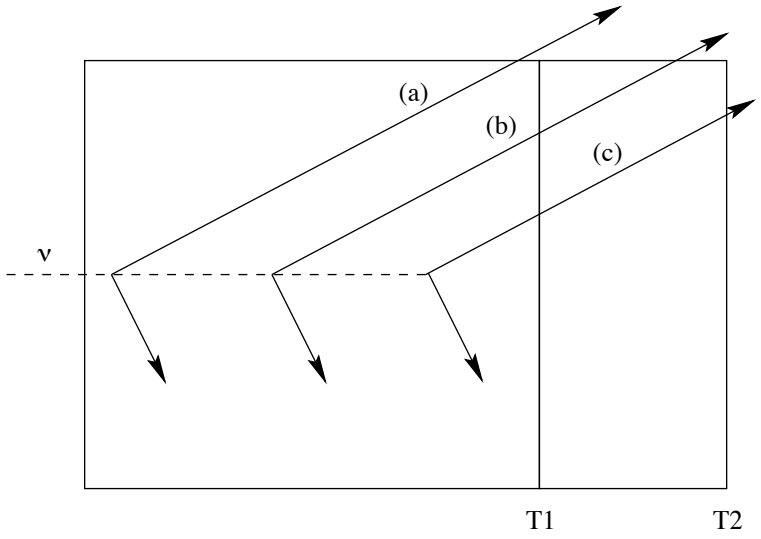

Figure 4.5: Three identical 2-track events at different interaction vertices. Event (a) would have zero hits in both T1 and T2, event (b) would have a hit in T1 but not in T2, event (c) would have hits in both T1 and T2 and would be the only event to trigger.

Comments on the Preliminary Analysis Filter.

Table 4.1 gives a summary of the acceptance of this filter for the different data samples.

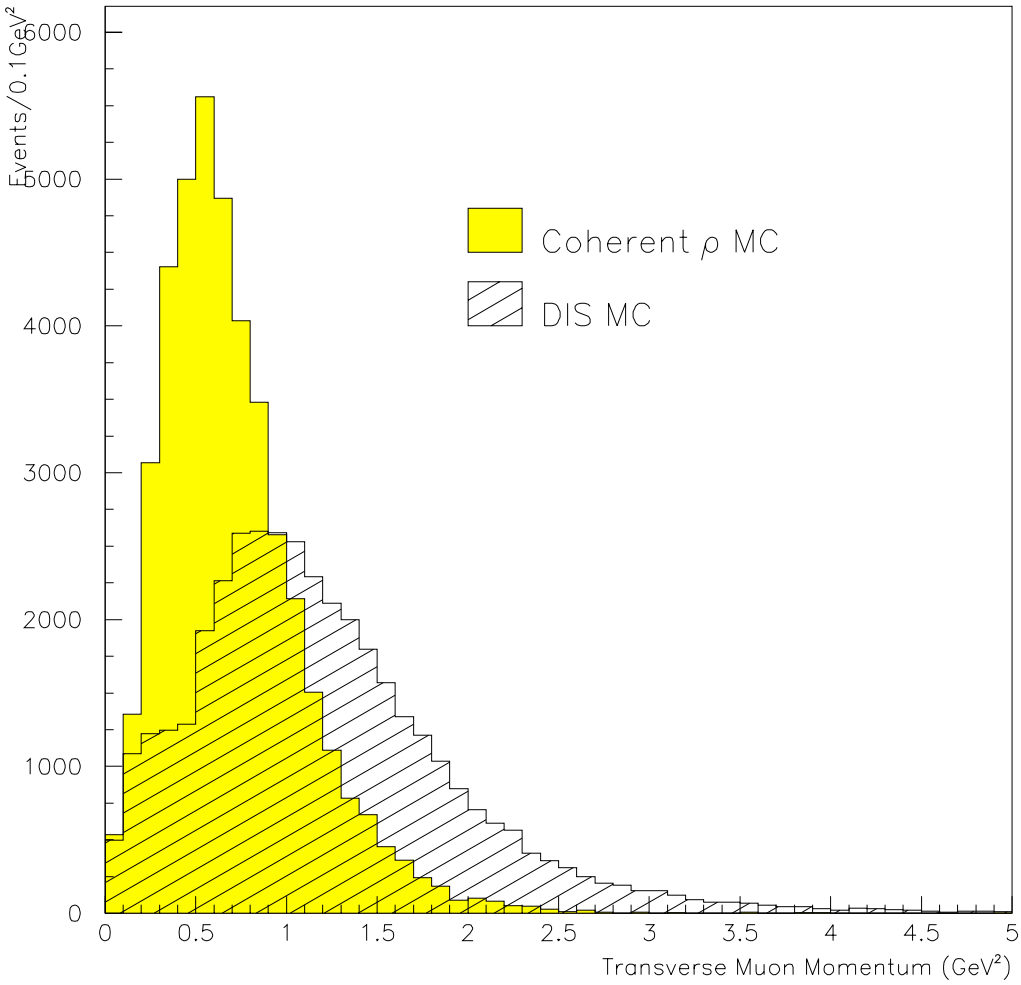

Figure 4.6: The muon transverse momentum.

Cut No.	Coh MC		DIS CC MC		Data	
	This Cut	Cumulative	This Cut	Cumulative	This Cut	Cumulative
1	94.2 %	94.2 %	96.7 %	96.7 %	79.4 %	79.4 %
2	93.9 %	88.5 %	54.8 %	53.0 %	41.7 %	33.1 %
3	85.9 %	76.0 %	94.0 %	49.8 %	89.1 %	29.5 %
4	95.7 %	72.7 %	85.1 %	42.4 %	80.0 %	23.6 %

Table 4.1: The percentage of events remaining after the preliminary filter.

After the first cut, both the Monte Carlo samples are reduced by very little (5%) compared to the data (20%). The Monte Carlo sample was generated to have an interaction vertex inside the fiducial volume and so the events cut here are only those events that were falsely reconstructed outside this volume. The data, on the other hand, contains events with interactions inside the magnet and forward calorimeter. It is mostly these events which are eliminated by this cut.

The second cut eliminates high multiplicity events. As Figure 4.4 shows, the DIS CC Monte Carlo has a lot of high multiplicity events. Consequently, this cut reduces the remaining DIS CC Monte Carlo events by 45%. This is considerably more than the coherent ρ Monte Carlo, which is reduced by only 6%. The data is reduced by 58%. Although the data is made up predominantly from DIS events, it also contains many events that are not real neutrino events at all, such as cosmic rays that may traverse the detector at a small enough angle to meet the trigger condition, but at an angle too large to hit the veto.

The third cut eliminates low multiplicity events. In this case slightly more coherent ρ Monte Carlo events are eliminated (14%) than are DIS CC Monte Carlo events (6%). This is understandable since coherent ρ events are low multiplicity events to begin with and just one missed track may cause the event to be eliminated by this cut. The reduction in data (11%) is larger than the reduction in the DIS CC Monte Carlo. The DIS CC Monte Carlo did not simulate quasi-elastic like events which usually have low multiplicity. Of course, the data contained such events. It is likely that this difference can be attributed to the exclusion of quasi-elastic like events in the DIS CC Monte Carlo.

The final cut in the filter is that the sum of the charges be consistent with a coherent ρ event. Naturally enough, the coherent ρ Monte Carlo is reduced by very little by this cut (4%) . Both the DIS CC Monte Carlo (15%) and the data (20%) have similar reductions.

Overall, the filter has a higher efficiency at eliminating DIS events (58%) than it does for coherent ρ events (27%). More importantly, however, the filter reduces

undesirable events in the data (76%), such as those caused by interactions in the magnet and forward calorimeter and those caused by other non-neutrino events such as large angle cosmic rays that have not been vetoed.

4.3.2 Particle Identification

In order to identify coherent ρ events, it was firstly necessary to identify all the constituent particles of such events.

In order to identify particles from information given by different subdetectors a track extrapolater [38] was used. This track extrapolator took into account all the relevant detector and physics processes, most importantly multiple scattering.

Muon Identification

In addition to the standard muon reconstruction, described in Section 3.10.3, some further cuts are imposed on the muon candidate.

- In order to prevent particles being falsely identified as muons, the muon candidate was required to have momentum greater than 1.5 GeV/c. This is a consequence of the iron wall before the muon chambers. Particles with momenta less than 2 GeV/c are unlikely to penetrate the iron absorber (magnet return yoke) and will not give a signal in the muon chambers.

- The muon candidate was required to match to the negatively charged track coming from the primary vertex. This matching was done by extrapolating the negative track from the primary vertex and seeing how close it was to the track in the muon chambers. A loose cut requiring the extrapolated drift chamber track to meet the one reconstructed by the muon chambers within 20 cm was applied. Examination of the distance between reconstructed muon tracks and extrapolated drift chamber tracks from Monte Carlo data samples showed that the majority of tracks matched to within $20cm$.

- A muon should deposit energy in the E.M. calorimeter. The track identified in the drift chambers as the muon was extrapolated to the front face of the E.M. calorimeter. The position of the nearest E.M. calorimeter cluster (Section 3.8.5 describes how this position is found) was calculated. The distance between the end of the extrapolated track and the centre of the nearest cluster is shown in Figure 4.7. Muon candidates with this distance greater than 11.2 cm were rejected. (11.2 cm is the size of the E.M. calorimeter lead-glass blocks. More detail on the lead-glass blocks is given in Section 3.8.1.)

- The muon candidate was required to deposit energy consistent with that of a minimum ionising particle in the E.M. calorimeter. This cut was made fairly loose, since the modeling of processes occurring in the calorimeter, see Figure 4.8, did not represent the data at low energies. (This has been rectified in a later version of the software).

$$0.250 < E_{dep}(\mu) < 0.8\ GeV \tag{4.13}$$

Charged Pion Identification

Any positively charged particle coming from the primary vertex that does not have a corresponding track in the muon chambers is taken to be a charged pion.

Photon Identification in the E.M. Calorimeter

If a photon reaches the E.M. calorimeter without converting it will initiate an electromagnetic shower. Monte Carlo studies on photons from π^0 decay have shown there is a 64% chance that neither photon will convert before the preshower. Of course, not all these photons will be within the angular acceptance of the preshower and E.M. calorimeter. In order for an electromagnetic shower to be interpreted as a photon it must pass the following cuts:

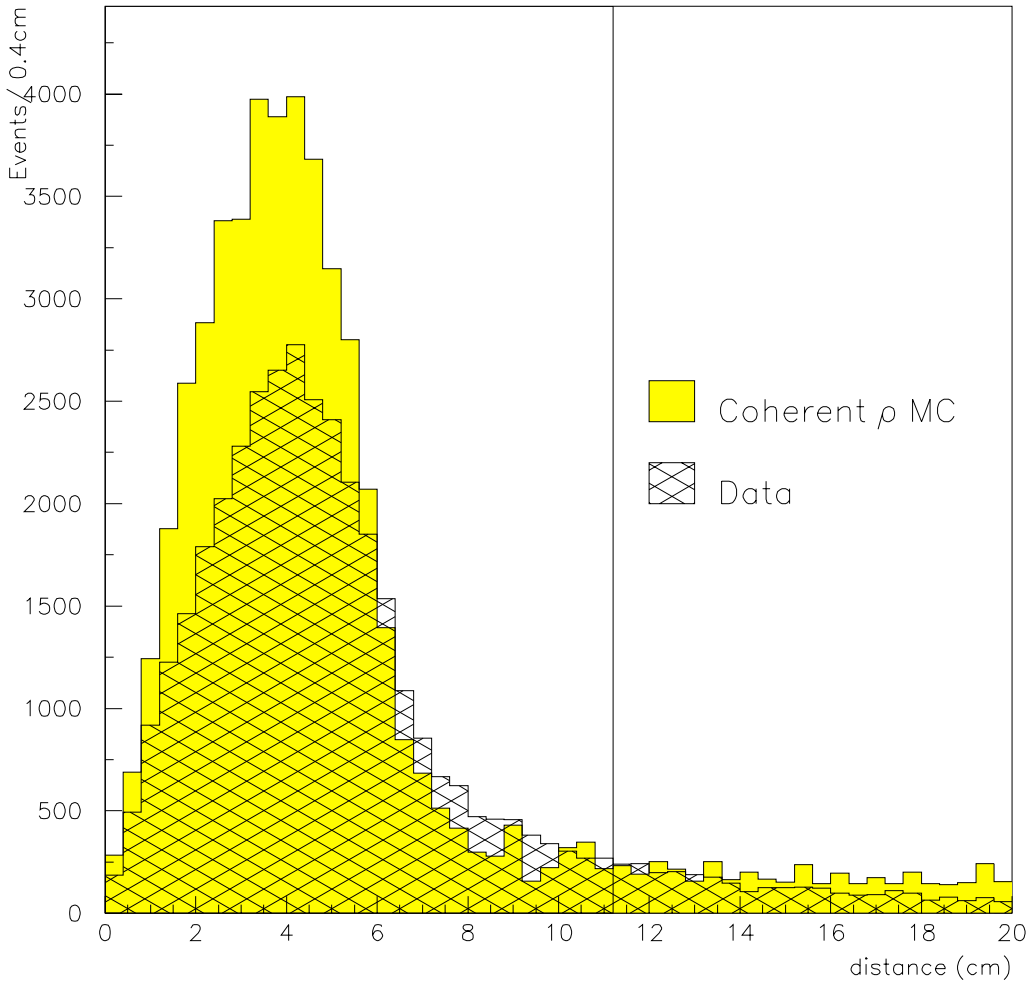

Figure 4.7: The difference in position between the E.M. calorimeter cluster position and the position expected from the track extrapolation to the front face of the E.M. calorimeter for muon candidates. Note: there is a long tail of events above 20 *cm*.

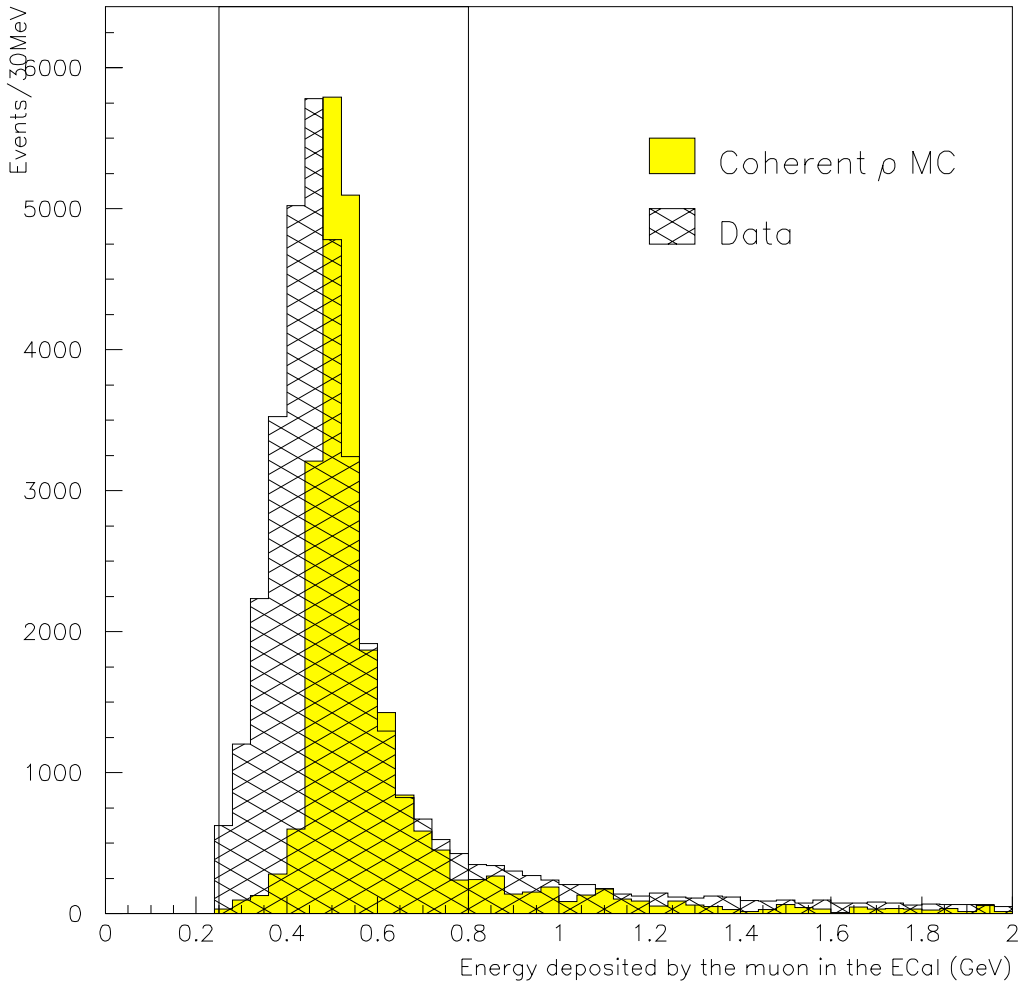

Figure 4.8: The energy deposited by muons in the E.M. calorimeter.

- No charged track in the drift chambers can be extrapolated to within 20 *cm* of the position of a cluster. (Section 3.8.5 gives a definition of a cluster.)
- The shower must be narrow, ie the radial extent of the shower must be less than 11 *cm*, see Figure 4.9. Hadronic showers tend to have a broader spatial distribution.

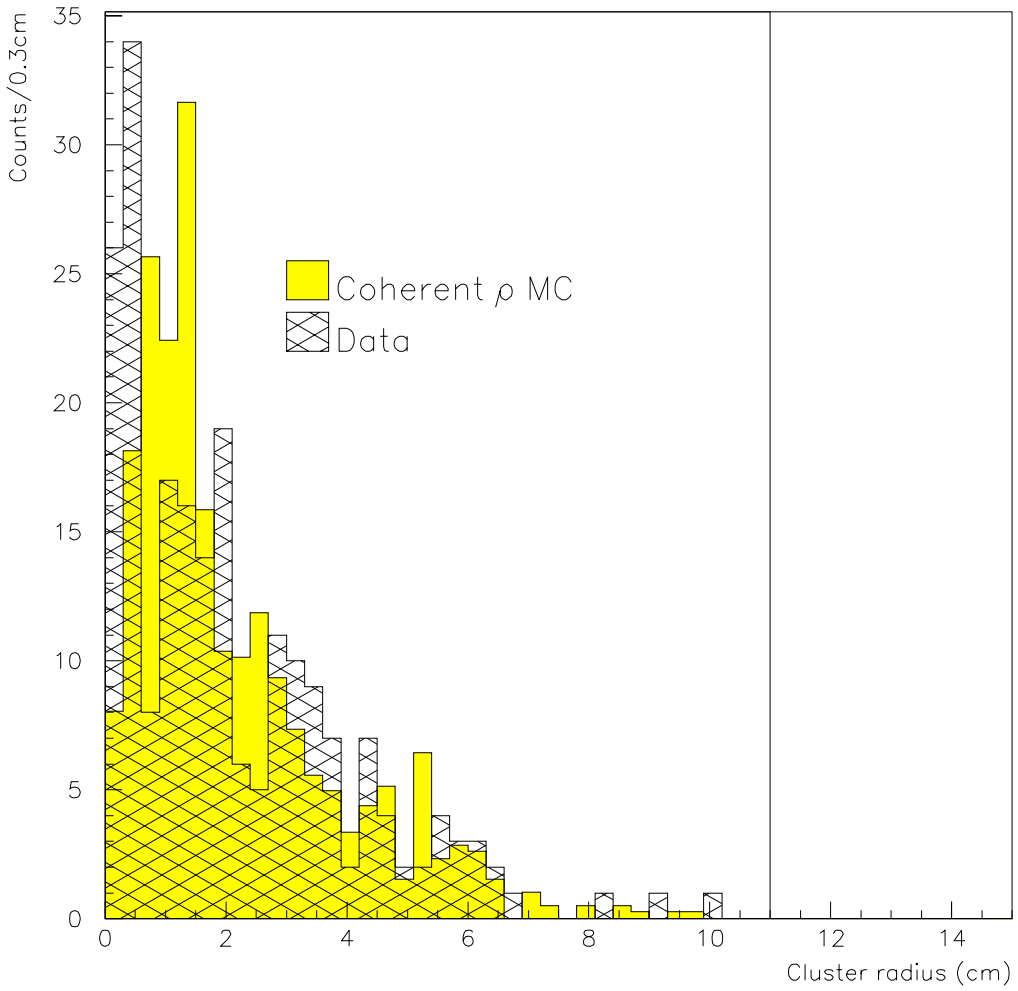

Figure 4.9: The radial width of γ clusters.

- It must be fully contained within the active area of the calorimeter, ie have a centroid position (x,y) such that

$$-137.0 < x, y < 137.0\ cm. \tag{4.14}$$

  This cut ensures an accurate energy measurement (2-6 % depending on the energy), i.e. it ensures no energy is lost out of the sides of the calorimeter.

- Its total energy must be more than 250 MeV. This cut ensures that any noise is not mistaken for a photon cluster.

- The photon cluster may not contain a known noisy cell. Noisy cells were particularly harmful to the search for π^0s because they

  - increase the background by causing "fake" photons to be found
  - mask the real signal by causing true two-photon events to appear as three-photon events and hence be discarded.

  Noisy cells were dealt with by treating that cell as a dead region. For each data sample, the dead region was of the order of 0.1% of the total area.

In order to make a more accurate measurement of the photon momenta than can be provided by the E.M. Calorimeter alone, information from the preshower is used. If a preshower cluster is found in front of the E.M. Calorimeter cluster it is considered to be caused by the same particle that caused the E.M. Calorimeter cluster. The cluster energy is then corrected for energy losses in the preshower. The position of the preshower cluster is considered to be the point at which the photon hit the preshower plane. This position and that of the primary vertex are used to compute the angle at which the photon traveled. This angle, along with the corrected cluster energy, is used to compute the momentum of the photon. If no preshower cluster is found in the vicinity of the E.M. Calorimeter cluster, the centroid of the E.M. Calorimeter cluster is used to determine the angle of the photon.

Photon Identification in the Drift Chambers

If the photon converts to an electron positron pair, $\gamma \rightarrow e^+e^-$, in the drift chambers, then its momentum can be measured from the curvature of the e^+e^- tracks. Monte Carlo studies on photons from π^0 decays have shown that there is 20% of any photon converting to an e^+e^- pair before reaching the preshower. In order for an e^+e^- pair from photon conversion to be accepted as a photon the following criteria must be met.

- Two oppositely charged tracks originating from a downstream non-primary vertex must be found.
- The invariant mass of the tracks, interpreted as an e^+e^- pair, must be less than 55 MeV, see Figure 4.10.

The photon momentum is computed by summing the momenta of both electrons at the beginning of their drift chamber tracks.

If one electron has a much greater momentum than the other, the one with low momentum may not be detected. If the track was extrapolated back to the same z-plane as the primary vertex and the extrapolated point lay within 1 cm of the primary vertex then the track was considered to come from an asymmetric photon conversion. However, this situation could also arise if the drift chamber reconstruction code missed the second electron. Including these events would therefore increase the likelihood of mismeasuring the photon energy. Consequently, it was decided not to include these events in the data sample. These events were infrequent and so their exclusion did not decrease the efficiency significantly.

Using the two methods of identifying photons described above, the two photons from π^0 decay can be identified in one of three ways, by finding:

- two E.M. Calorimeter clusters,
- one E.M. Calorimeter clusters and one e^+e^- pair
- two e^+e^- pairs

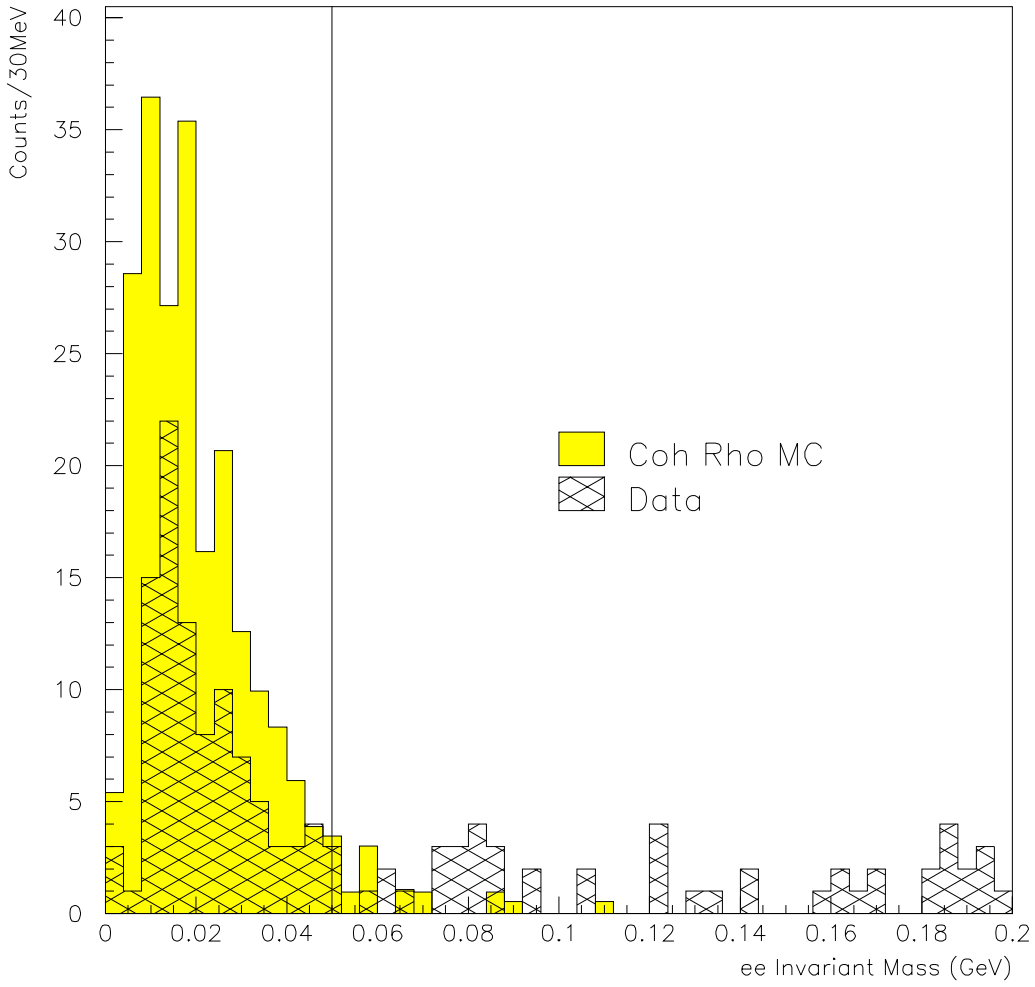

Figure 4.10: The invariant mass of the e^+e^- pair photon candidates.

The proportion of events falling into each of these three categories for each of the coherent ρ and DIS Charged Current Monte Carlos and the data are shown later in Table 4.3.

Neutral Pion Identification

The π^0 ($M_{\pi^0} = 135\ MeV$) decays 98.8% of the time to two photons ($\pi^0 \rightarrow \gamma\gamma$). In order to identify a π^0 two photons need to be observed and accepted. However, in order to identify π^0 from coherent ρ production two and only two photons need to be found, hence there is no combinatorial background. Once they have been identified, it is possible to see if they have originated from π^0 decay by looking at their invariant mass. Figure 4.11 shows the invariant mass distribution for photon pairs from the coherent Monte Carlo sample and from the data. Figure 4.11 (a) shows the distribution formed using events where both photons are identified via an E.M. Calorimeter cluster. Figure 4.11 (b) shows the distribution formed using events where one photon is identified via an E.M. Calorimeter cluster and the other via the identification of an e^+e^- pair in the drift chambers. A clear peak at the mass of the π^0 can be seen for both samples. This plot allows us to constrain $90 < M_{\gamma\gamma} < 180\ MeV$.

Dalitz decays, $\pi^0 \rightarrow e^+e^-\gamma$ were not looked for. These constitute only 1.2% of the total π^0 signal which is minimal compared to the other inefficiencies of the search.

ρ Identification

The ρ^+ ($M_\rho = 770\ MeV$) decays to two pions ($\rho^+ \rightarrow \pi^+\pi^0$) $\approx$ 99.9% of the time. Figure 4.12 shows an enhancement at the π^0, ρ^+ mass. After cutting to include only those events containing π^0, a clear peak at the ρ invariant mass spectrum can be seen. Figure 4.13 shows the invariant mass distribution before the cut on the $\gamma\gamma$ mass. Figure 4.14 shows the distribution after that cut. A clear peak is seen in the second plot. The $\pi^+\pi^0$ mass was constrained to be $550 < M_{\pi^+\pi^0} < 990\ MeV$.

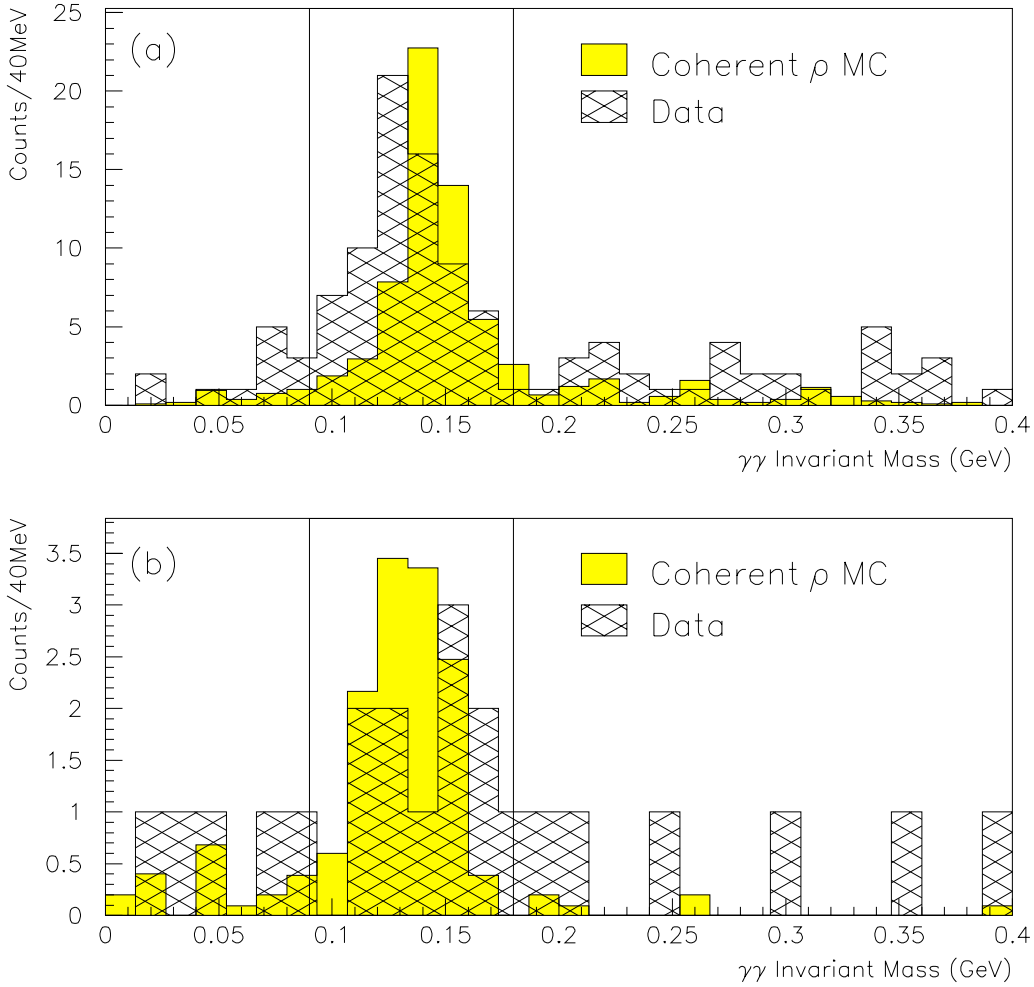

Figure 4.11: The $\gamma\gamma$ invariant mass spectrum from (a) two cluster events, (b) one cluster, one e^+e^- pair.

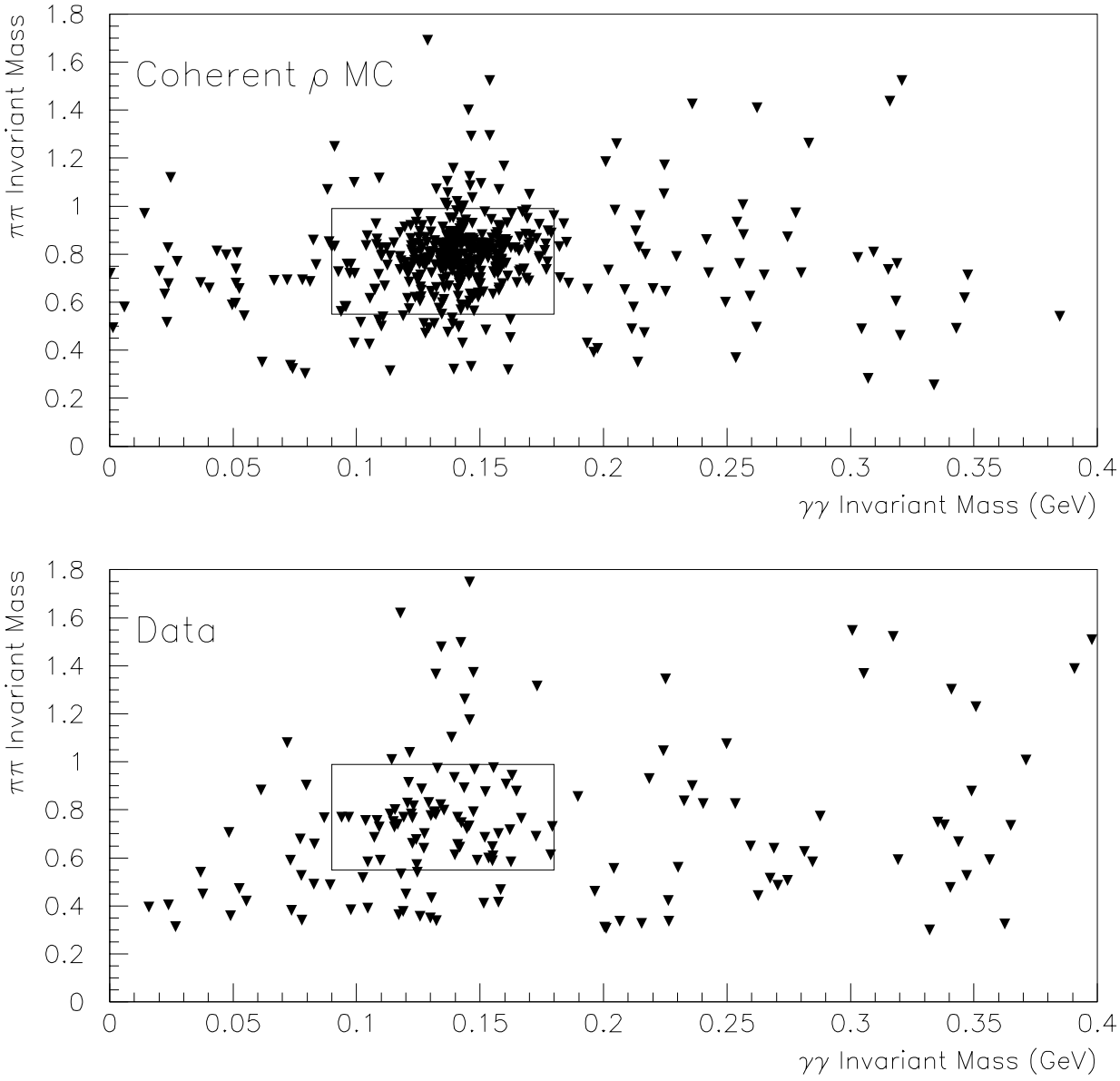

Figure 4.12: A scatter plot of $M_{\pi^0\pi^+}$ vs $M_{\gamma\gamma}$.

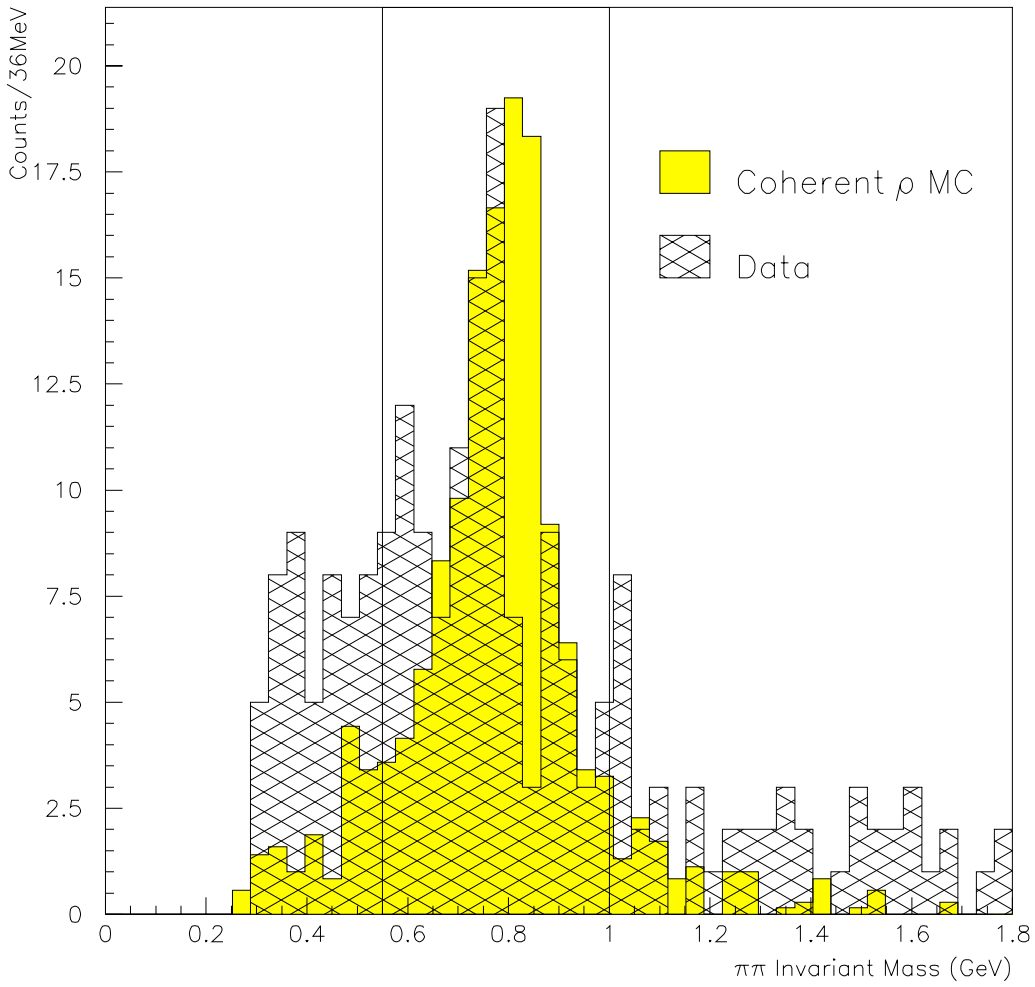

Figure 4.13: The $\pi^0\pi^+$ invariant mass spectrum before cuts on $M_{\gamma\gamma}$.

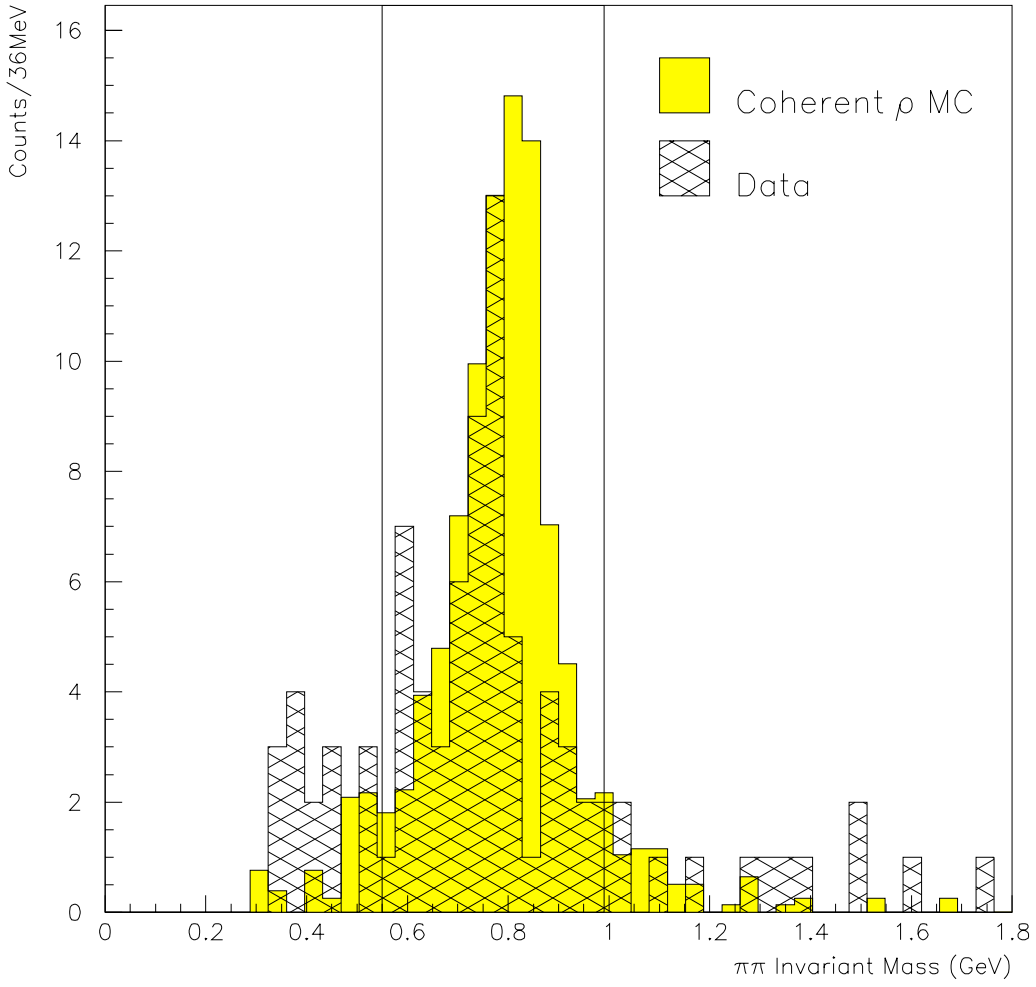

Figure 4.14: The $\pi^0\pi^+$ invariant mass spectrum after cuts on $M_{\gamma\gamma}$.

4.3.3 Coherent Selection & The Analysis Filter

An analysis filter was designed in order to separate coherent diffractive events from the incoherent background. Since coherent events contain the particles $\mu^-\pi^+\pi^0$ (the recoil nucleus is not seen) and no others, events with any other possible particle were discarded from the sample.

The efficiency of this analysis filter is summarized in Table 4.2. This table is a continuation of the table of efficiencies presented earlier in Table 4.1. Hence, the first line in this table is the last line of Table 4.1.

Cut No.	Coh MC		DIS CC MC		Data	
	This cut	Cumulative	This cut	Cumulative	This cut	Cumulative
		72.7 %		42.4 %		23.60 %
1	99.2 %	72.11 %	93.7 %	39.71 %	100.0 %	23.60 %
2	93.1 %	67.10 %	81.6 %	32.41 %	79.0 %	18.64 %
3	58.7 %	39.40 %	29.7 %	9.64 %	16.3 %	3.04 %
4	63.8 %	25.14 %	28.2 %	2.72 %	31.2 %	0.95 %
5	94.6 %	23.78 %	91.5 %	2.49 %	90.5 %	0.86 %
6	98.7 %	23.48 %	99.2 %	2.47 %	98.9 %	0.86 %
7	98.9 %	23.22 %	96.0 %	2.37 %	96.7 %	0.83 %
8	25.3 %	5.87 %	6.8 %	0.16 %	4.8 %	0.04 %
9	76.5 %	4.49 %	62.5 %	0.10 %	50.0 %	0.02 %
10	88.0 %	3.95 %	60.0 %	0.06 %	50.0 %	0.01 %

Table 4.2: The percentages of events remaining after analysis cuts (ϵ).

The following criteria had to be met in order for an event to be considered a coherent diffractive ρ candidate.

1. The event had to satisfy the trigger condition

$$T_{1(2)} = 1 \tag{4.15}$$

where $T_{1,2}$ is true if there is at least one hit in trigger plane 1(2). This cut was added for consistency between the data and the Monte Carlo. It removes very few events from either the Coherent ρ Monte Carlo ($< 1\%$)

or the DIS CC Monte Carlo ($< 7\%$) samples. Of course, no events are removed from the data using this cut. If the data did not meet the trigger condition it would never have been recorded.

2. The primary vertex position was further constrained to be

$$-130 < x, y < 130 \ cm \tag{4.16}$$

$$0 < z < 370 \ cm \tag{4.17}$$

This cut ensures poorly contained events, such as those with particles escaping into the magnet ends and supports do not contaminate the data sample. It removes approximately 7% of the remaining coherent ρ Monte Carlo events and approximately 20% of the DIS CC Monte Carlo and data events.

3. The event must contain a muon candidate passing the cuts described in Section 4.3.2. This cut reduces the coherent Monte Carlo sample to 59% of its previous size. However, it also reduces the DIS CC Monte Carlo to 30% and the data 16% of what they previously were. The larger reduction in the data compared to that in the DIS CC sample can be attributed to the elimination of neutral current events from the data.

4. The event must contain charged tracks consistent with the correct event topology. There must be two and only two oppositely charged tracks coming from the primary vertex. Any other tracks must be consistent with electron tracks coming from photon conversions as described in Section 4.3.2. Any events where the charged pion underwent a secondary interaction were discarded.

   This cut rejects approximately 70% of both the DIS CC and data samples as these samples typically have more than two tracks beginning at the primary vertex. 36% of the coherent ρ sample is rejected. Coherent diffractive events eliminated by this cut include events in which:

- the charged pion re-interacts,
- track reconstruction inefficiencies split a track left by a single particle into two or more track segments,
- the photon converts, but one of the electrons is missed.

5. If the charged tracks are extrapolated to the front face of the E.M. Calorimeter, i.e. they do not stop in the detector or exit the detector from the sides, the event had to contribute some E.M. calorimeter activity within 20 cm of the extrapolated track.

   Fewer than 10% of events from all data samples are cut by making this requirement, but is necessary in order to provide a clean sample of events.

6. All clusters had to be well contained within the E.M. calorimeter in both x and y-directions,

$$-137cm < x, y < 137\ cm. \tag{4.18}$$

   Fewer than 2% of events from all data samples are cut by making this requirement.

7. Any calorimeter cluster not associated to a charged track must meet the criteria described in Section 4.3.2 for photon identification. This cut is designed to eliminate events with neutral clusters caused by neutral hadrons.

   Fewer than 4% of events from all data samples are cut by making this requirement.

8. The number of neutral E.M. calorimeter clusters must be equal to that expected from the event under the assumption that it is a coherent ρ event, that is either two, one or zero clusters depending on the number of e^+e^- pairs found. Events with any other combination of neutral candidates were discarded.

   This cut was extremely damaging to both the DIS CC events (only 7%

survive) and the data (only 5% survive). This cut is so effective against these samples because neither the DIS CC Monte Carlo or the data necessarily contain just one π^0 per event.

Unfortunately, the coherent ρ Monte Carlo was strongly effected by this cut. The sample was reduced to 25% of its previous strength. The coherent diffractive events cut using this criteria were events in which:

- Both photons deposited energy in the same region of the E.M. calorimeter and appeared as one cluster.
- One or both photons deposited energy in the same region of the E.M. calorimeter as a charged track.
- One or both photons left the detector without depositing energy in the E.M. calorimeter.
- An electron from pair production underwent bremsstrahlung.
- The muon produced a delta-ray that went undetected in the drift chambers.

The events that pass this cut fall into three one of three categories. The proportion of events in each category is shown in Table 4.3. The invariant mass distributions of the $\gamma\gamma$ pairs for the first two categories are shown in Figures 4.11 (a) and (b). It is not sensible to show a similar plot for events in which both photons are identified via an e^+e^- pair, since there are two few events in this category to make any conclusions about the distribution.

Photon Type	Coh MC		DIS CC MC		Data	
	Events		Events		Events	
Two Clusters	447	82.0 %	136	81.0 %	160	75.5 %
One Cluster, One pair	96	17.6 %	32	19.0 %	46	21.7 %
Two pairs	2	0.4 %	0	0.0 %	6	2.8 %

Table 4.3: The number of π^0 candidates identified via E.M. Calorimeter clusters and via tracks in the drift chambers.

9. The invariant mass of the photon photon pair had to fall within the π^0 mass limits as described in Section 4.3.2.

   If the effect of this cut on the coherent ρ sample (76% survive) is contrasted with the effect it has on the DIS CC Monte Carlo (63% survive) and the data (50% survive) it is clear that this requirement causes a significant reduction in the background. The difference in the reduction factors between the DIS CC Monte Carlo and the data may seem significant, but by this stage there are very few events left in the sample and the uncertainties are large. Again, the invariant mass of the photon photon pair from non-coherent events may differ from what is expected for a π^0 if the photons come from different π^0s within the same event.

10. The invariant mass of the $\pi\pi$ pair had to fall within the limit of the ρ mass as described in Section 4.3.2.

    Again, if the effect of this cut on the coherent ρ sample (88% survive) is contrasted with the effect it has on the DIS CC Monte Carlo (60% survive) and the data (50% survive) it is clear that this requirement causes a significant reduction in the background. Again the statistics are low and the uncertainties are large.

Comments on the Analysis Filter.

The most damaging cuts to the DIS CC and data samples are those that require that the event topology be that of a coherent diffractive ρ event (cuts no. 3, 4 and 8) and those that require the presence of a π^0 and a ρ (cuts no. 9 and 10).

After application of all the cuts described above, the overall efficiencies for reconstructing coherent diffractive ρ Monte Carlo is 3.9%. This value is extremely low, but it is necessary to cut this severely in order to reduce the significant contribution from Deep Inelastic Scattering events (reduced to 0.06% of the original amount). This leads to a DIS CC Monte Carlo reduction factor 66 times greater than the coherent ρ reduction factor.

4.4 Backgrounds

In the search for coherent diffractive ρ events two main backgrounds are envisaged, the background from Δ-Resonance production and the background from Deep Inelastic Scattering events. In the following sections 4.4.1 and 4.4.2 the possible contribution from these two sources are examined.

4.4.1 Background From Δ-Resonance Production

A potentially significant source of background to the coherent ρ search is from quasi-elastic resonance production of deltas and their subsequent decay.

$$\nu n \rightarrow \mu^- \Delta^+, \;\; \Delta^+ \rightarrow p^+ \pi^0 \tag{4.19}$$

If the decay proton from is taken to be a charged pion and if the invariant mass of the "π^+"π^0 pair falls within the range of the ρ mass, then this event could pass the cuts to isolate coherent diffractive ρ events.

The Expected Number of Δ^+s.

The fiducial volume of NOMAD used in this analysis is $2.6 \times 2.6 \times 3.7 m^3$ corresponding to a fiducial mass of $2.5 \times 10^3 kg$. The number of protons and neutrons in NOMAD is calculated [40] to be:

$$N_{prot} = 7.9 \times 10^{29} \tag{4.20}$$

and

$$N_{neut} = 7.2 \times 10^{29} \tag{4.21}$$

in the full 11 modules.

The cross-section for $\nu n \rightarrow \mu^- p \pi^0$ is to a good approximation energy inde-

pendent over the energy range in question [41], [42] and has the value

$$\sigma(\nu_\mu n \to \mu^- p\pi^0) = 0.35 \times 10^{-38}\ cm^2 \tag{4.22}$$

The integral over the neutrino flux can be estimated from the neutrino beam Monte Carlo. This calculation is discussed in more detail in Section 4.5.2. The number of neutrinos used in calculations of expected event rates is shown in Table 4.4.

Data Sample	$\int \phi(E)dE$	N_{neut}
8-module	3.10×10^{16}	5.2×10^{29}
11-module	2.25×10^{16}	7.2×10^{29}

Table 4.4: A summary of the parameters used to calculate the expected number of Δ^+ particles in NOMAD.

The number of expected interactions can be calculated from the relation

$$\frac{dN}{N} = \frac{n\sigma A}{A} dz \tag{4.23}$$

where N is the expected number of interactions, n is the number density of target particles, Adz is an infinitesimal volume of target with area A perpendicular to the beam and σ is the cross-section. Neutrinos interact so rarely that to a very good approximation it can be assumed that the neutrino flux does not decrease as the beam passes through the target. Integrating Equation 4.23 and making the approximation described above we can deduce the number of $\nu n \to \mu^- p\pi^0$ events expected in NOMAD (assuming 100% efficiency) to be

$$\begin{aligned} N(\nu_\mu n \to \mu^- p\pi^0) &= \frac{N_{neut} \times \sigma}{A} \int \phi(E)dE \\ &= 1670 \end{aligned} \tag{4.24}$$

where N_{neut} is the number of neutrons in the detector, ϕ is the neutrino flux at

NOMAD, A is the cross-sectional area of NOMAD and σ is the cross-section for this interaction.

Two methods were used to understand how many of these 1670 such events would fake coherent ρ and contaminate the signal. The first method was a direct simulation of resonance production. The second method involved using an easily identifiable resonance (Δ^{++}) and transforming it to the more elusive Δ^{+}.

Δ-Resonance Simulation.

The first method used was a Monte Carlo simulation of resonance production by neutrinos, based on the cross section calculation by Rein & Sehgal [43].

A sample of 1942 events underwent the same analysis and cuts as that of the coherent Monte Carlo, the Deep Inelastic Scattering Monte Carlo and the data.

The most effective cut against these quasi-elastic like resonances is the requirement that both the photons from the π^0 decay were identified. Table 4.3 shows that the majority of photons are identified via a photon-like E.M. Calorimeter cluster. In order for the π^0 from the Δ decay to be found, at least one photon must reach the E.M. calorimeter and deposit energy above threshold. Even if one photon converts in the drift chamber as happens $\approx 20\%$ of the time, the other photon must still reach the front face of the E.M. Calorimeter in order for the π^0 to be identified. The π^0s from Δ-resonance decays are of much lower energy than are π^0s from coherent diffractive ρ, see Figure 4.15. Consequently, the photons from Δ-resonance interactions are widely spread in angle compared to those from coherent ρ production and many more of them exit through the side of the detector instead of depositing energy in the E.M. calorimeter.

As a result of this low energy distribution, the acceptance for finding π^0 from Δ^{+} is very low. Of the 1942 Monte Carlo events studied, 0 events passed the required cuts. Under Poisson statistics, this translates as a limit of

$$N_{BG} \leq 2.3 \tag{4.25}$$

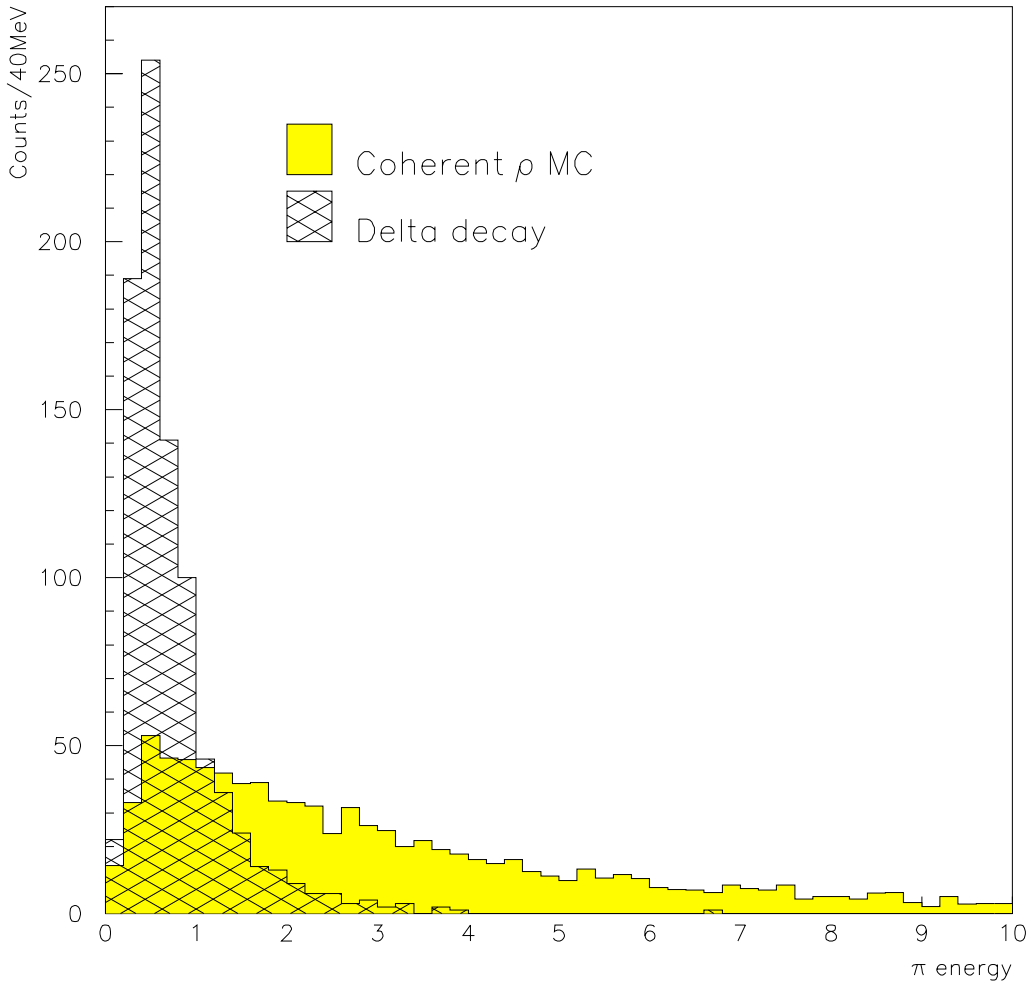

Figure 4.15: The π^0 energy spectrum from Δ^+ decay and from coherent ρ decay.

Search For Δ^{++} in the Data.

In order to find a method of studying the quasi-elastic resonant background that is independent of detector efficiencies and acceptances and has a greater statistical significance than the method described above, a second method of analysis was devised.

The interaction

$$\nu p^+ \rightarrow \mu^- \Delta^{++}, \;\; \Delta^{++} \rightarrow p^+ \pi^+ \tag{4.26}$$

is much easier to identify than the Δ^+ interaction described by Equation 4.19 due to the relative ease of finding charged tracks compared to the difficulty of finding neutral particles. Since the kinematics of both these interactions are for our purposes identical, a knowledge of the amount of Δ^{++} in the data will allow a good estimate of the amount of Δ^+.

Naively, one might expect the production rate of Δ^+ to be twice the production rate of Δ^{++}, since at the quark level we have the same process and there are twice as many down quarks in neutrons as in protons. Isospin invariance then tells us that while the Δ^{++} decays 100% of the time to $p\pi^+$, the Δ^+ decays only 2/3 of the time to $p\pi^0$. This would lead us to conclude that the rates for interaction 4.19 and interaction 4.26 would be in the ratio of 4:3.

A more sophisticated estimation of the cross-section ratios for the two interactions can be gained from current algebra. This leads us to conclude that Δ^{++} particles ($I = \frac{3}{2}$, $I_3 = \frac{3}{2}$) are produced three times more frequently than Δ^+ particles ($I = \frac{3}{2}$, $I_3 = \frac{1}{2}$). This results in a ratio of 9:2 for interaction 4.26 to interaction 4.19.

Experimental results give a third answer for the ratio of the production rates. The cross-sections for these two interactions at energies above 2 GeV are [41]:

$$\sigma(\nu p \rightarrow \mu^- \Delta^{++}) = 0.70 \times 10^{-38} \; cm^2, \tag{4.27}$$

$$\sigma(\nu n \rightarrow \mu^- \Delta^{+}) = 0.35 \times 10^{-38} \; cm^2, \tag{4.28}$$

(no uncertainties are quoted). So, from experimental production rates, we expect twice as many Δ^{++} events as Δ^{+} events.

For the purpose of this analysis, the experimental ratio is used.

The search for Δ^{++} candidates was made using the following algorithm.

- Events with one muon and two additional positive tracks coming from the primary vertex were considered as candidates.

- Events with other activity indicating the presence of other particles were not considered as candidates, i.e. no events with neutral E.M. calorimeter clusters or secondary vertices were accepted.

- The two positive tracks were used to make the Δ^{++} invariant mass. Both combinations were formed. In the first combination, the first tracks was assumed to be the proton and the second the pion. In the second combination, the first tracks was assumed to be the pion and the second was assumed to be the proton. The combination with the calculated Δ mass closest to the true Δ mass was used. In this way, the best assignment of the $p^{+}\pi^{+}$ tracks was made. Figure 4.16 shows the invariant mass distribution of these tracks after the assignment of the tracks. Only events with $1.00 < M_{\Delta} < 1.70\ GeV$ were passed. This gives a total of 870 events.

- A π^{0} was formed from the 3-momentum of the π^{+}. In order to do this, the charge of the particle was set to zero, the mass to $M_{\pi^{0}}$ and the 3-momentum to that of the reconstructed π^{+}.

- This artificial π^{0} was made to decay isotropically to two photons. As a first approximation, the momenta of the photons are not "smeared" by detector effects.

- These photons were extrapolated from the primary vertex to the z-plane of the E.M. calorimeter. Figure 4.17 shows the spatial distribution of photon pairs at the front face of the E.M. calorimeter from Δ-resonance production.

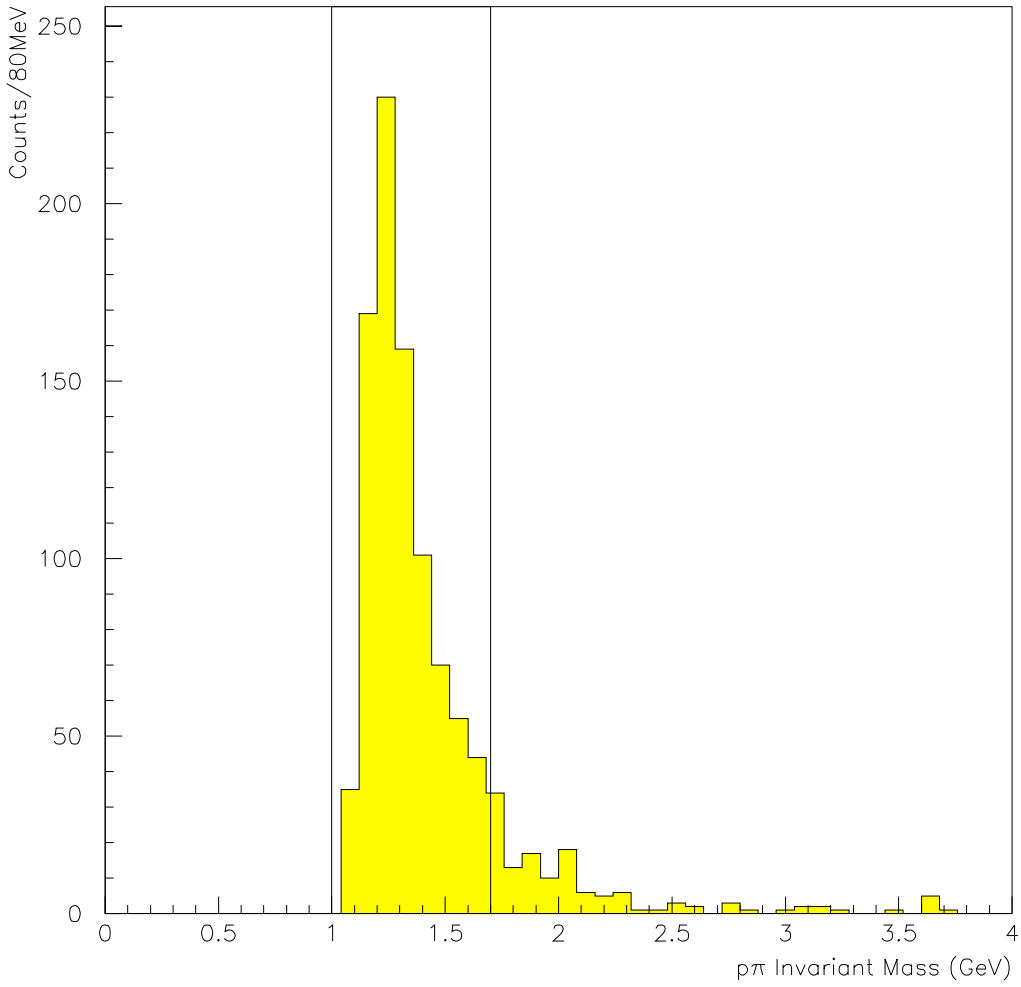

Figure 4.16: The "best" invariant mass of the $p\pi^+$ pair.

It can be seen that a large percentage of photons miss the E.M. calorimeter altogether. Thus, the hypothesis that quasi-elastic like resonances have a very poor angular acceptance is confirmed by this independent method of analysis.

- If both photons were within the angular acceptance of the E.M. calorimeter, the π^0 and ρ invariant masses were formed, see Figure 4.18. For the ρ, the proton was deliberately taken to be a charged pion and the charged pion to be a neutral one.
- The events falling within $550 < M_\rho < 990\ MeV$ were accepted as a contribution to the background.
- The t' -distribution of the remaining events was plotted in Figure 4.19.

Given the low statistics available, it is difficult to tell the exact shape of the t' background distribution from this plot. If we consider that momentum smearing would drag low t' events higher, the distribution shown in Figure 4.19 is a pessimistic one. Furthermore, Figure 4.19 contains twice as many events as we actually expect (the ratio of Δ^{++} to Δ^{+} is two). Using this method of analysis, we expect only 2 events in the region below $t' < 0.1\ GeV^2$. The very lack of events in the low t' region clearly indicates that the signal shown later in Figure 4.20 is not due exclusively to Δ-Resonance production.

4.4.2 The Deep Inelastic Background

Another possible source of background comes from low multiplicity charged current deep inelastic scattering. In order to study the effect of this background on the signal, another Monte Carlo simulation was performed. This simulation was based on the LUND Monte Carlo for deep inelastic scattering, LEPTO [37].

A search was made in the simulated deep inelastic scattering events for coherent diffractive like events, ie events containing μ, π^+ and π^0. The algorithm used in this search is identical to that used in the search for coherent diffractive ρ and

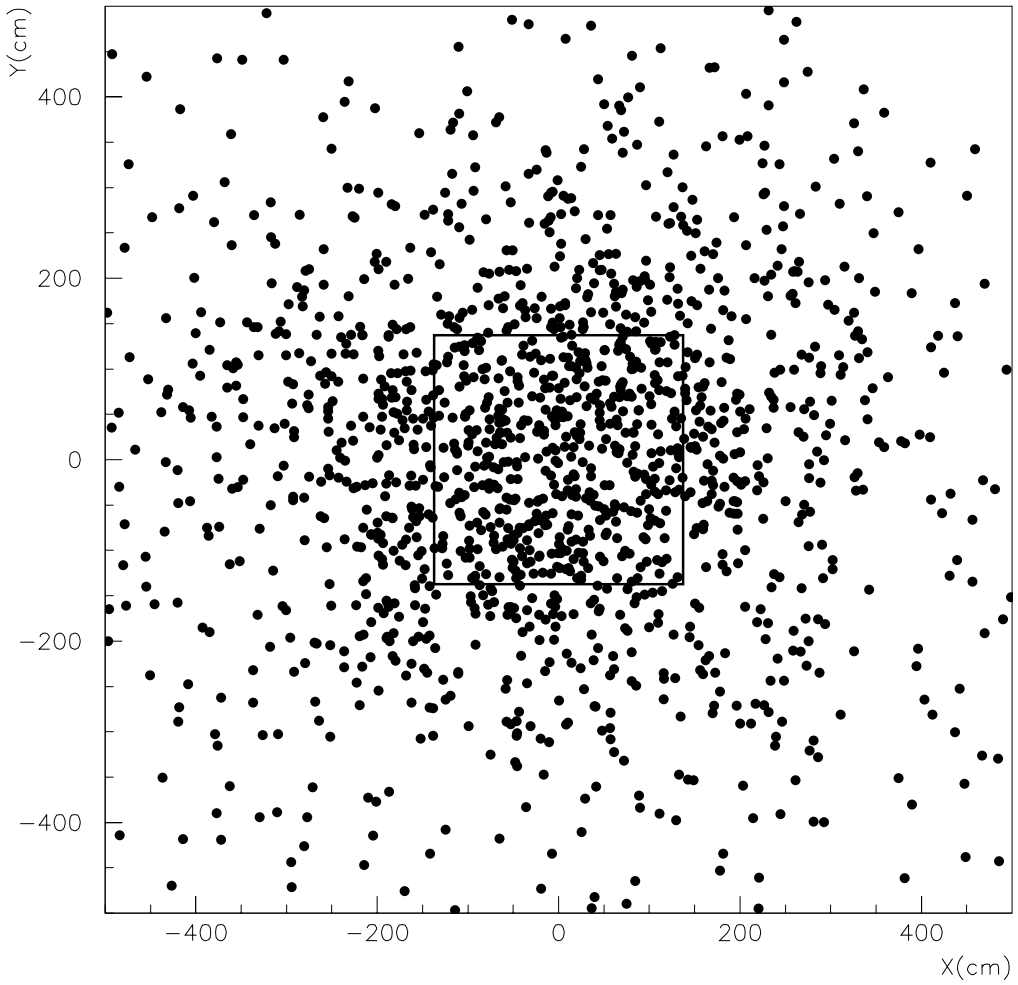

Figure 4.17: The xy-spatial distribution of photons at the front face of the E.M. calorimeter. The region enclosed by the box $-137 < x, y < 137$ cm represents the acceptance of the calorimeter.

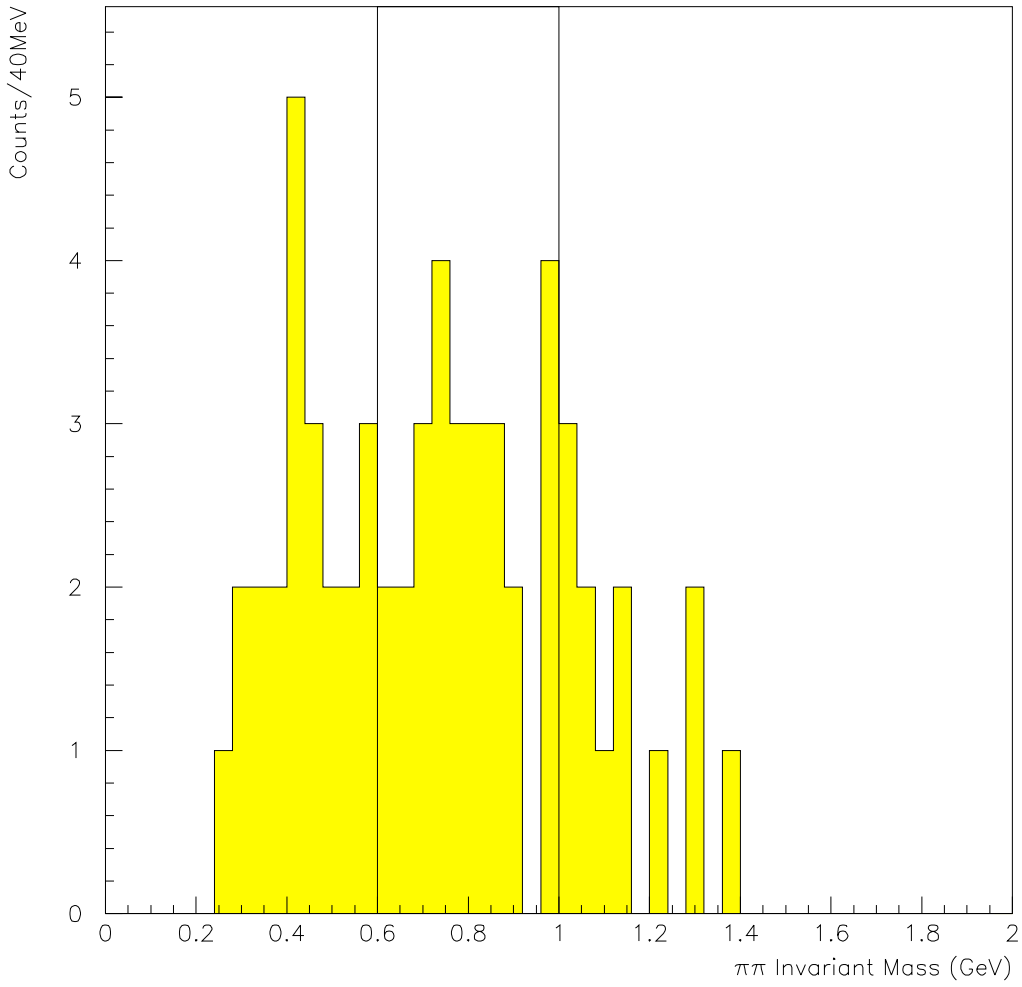

Figure 4.18: The $\pi^0\pi^+$ invariant mass distribution of the manufactured Δ^+ sample.

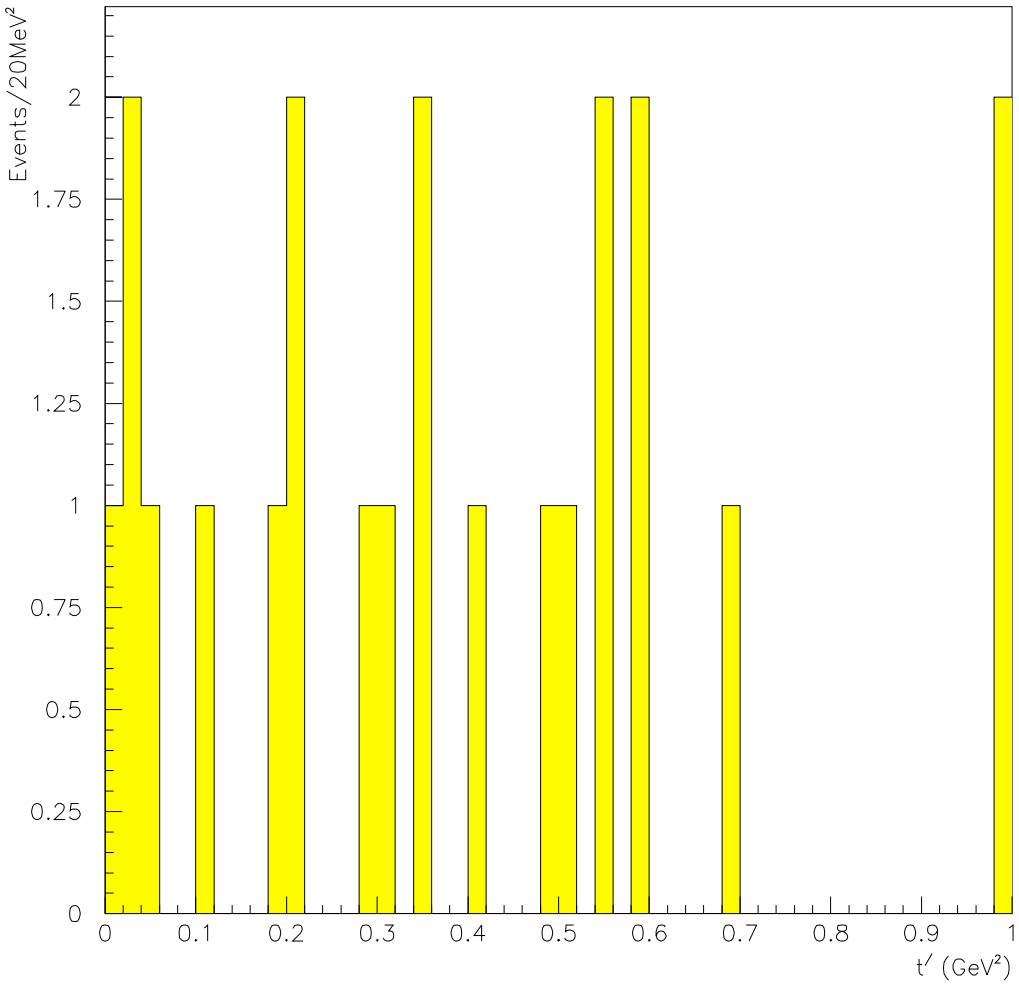

Figure 4.19: The t' -distribution of the manufactured Δ^+ sample.

has been described in extensively throughout Section 4.3. The resultant efficiency for reconstructing these events as coherent ρ events is very low, of the order of 0.1%, see Table 4.2. However, given the large sample size, a significant number of events satisfy the criteria described above. 30 events pass all cuts and have $t' < 1.0\ GeV^2$.

An investigation was made into the types of charged current DIS events which could mimic coherent ρ. It was found that a significant proportion were events containing a ρ, but with a neutron that went undetected. Some information on all low multiplicity charged current events passing all the cuts and having t' less than 0.1 GeV^2 are tabulated in Appendix C.

4.4.3 Conclusions on the Background to the Search for Coherent ρ

As the above studies using both the direct simulation of Δ-resonance production and the transformation of the Δ^{++} to Δ^{+} have shown, the background from Δ production is very small (< 2.5 events). The background from Deep Inelastic Scattering Charged Current however is not negligible. Consequently, further calculations will use the approximation that the only background to the search for coherent ρ is Deep Inelastic Scattering Charged Current events.

4.5 Results

4.5.1 Kinematic distributions.

In order to give further weight to the hypothesis that the events we have isolated using the analysis cuts described in Section 4.3.3 are coherent ρ events we can compare some kinematic distributions from our signal candidates to that we expect from the Monte Carlo events.

The t' -distribution.

One of the main features of coherent diffractive meson production is the characteristically steep exponential dependence on t' , as described in Section 2.1.1.

The t' -distribution for the coherent Monte Carlo is compared to that of the data in Figure 4.20. These plots are made on a log scale to illustrate more clearly the exponential nature of the observed slope.

MINUIT [44] was used to calculate an exponential fit to the coherent ρ Monte Carlo t' -distributions such that

$$N = P_1 e^{-P_2 t'} . \tag{4.29}$$

The fit was performed over the region $0 \rightarrow 0.1\ GeV^2$, since the coherent diffractive Monte Carlo indicates there are very few events with $t' > 0.1\ GeV^2$.

The important parameter to consider is the slope parameter $P_2 = b$. For the coherent Monte Carlo this parameter is

$$b = 42 \pm 3\ GeV^{-2}. \tag{4.30}$$

It should be noted that the distribution has been somewhat broadened from the generated slope of $b = 56.6\ GeV^{-2}$ by the finite resolution of NOMAD. The few events present in the tail of the distribution ($t' > 0.1\ GeV^2$) are due to mis-measurement of the particle momenta.

A similar fit was performed on the data. The fit results for this distribution correspond within uncertainties with that predicted by the Monte Carlo for coherent diffractive ρ and clearly indicate an enhanced signal at low t' . There is a noticable excess of events in the data at $t' \approx 0.1\ GeV^2$. It is likely that this excess is a statistical fluctuation. The slope parameter is

$$b = 28 \pm 9\ GeV^{-2}. \tag{4.31}$$

The

Figure 4.21 shows an enlargement of Figure 4.20 at low t' for the data. The curves of $\pm 1\sigma$ are drawn along with the best fit to the slope. The uncertainty on the slope seems very large, it is of the order of 35%. However, when the maximum and

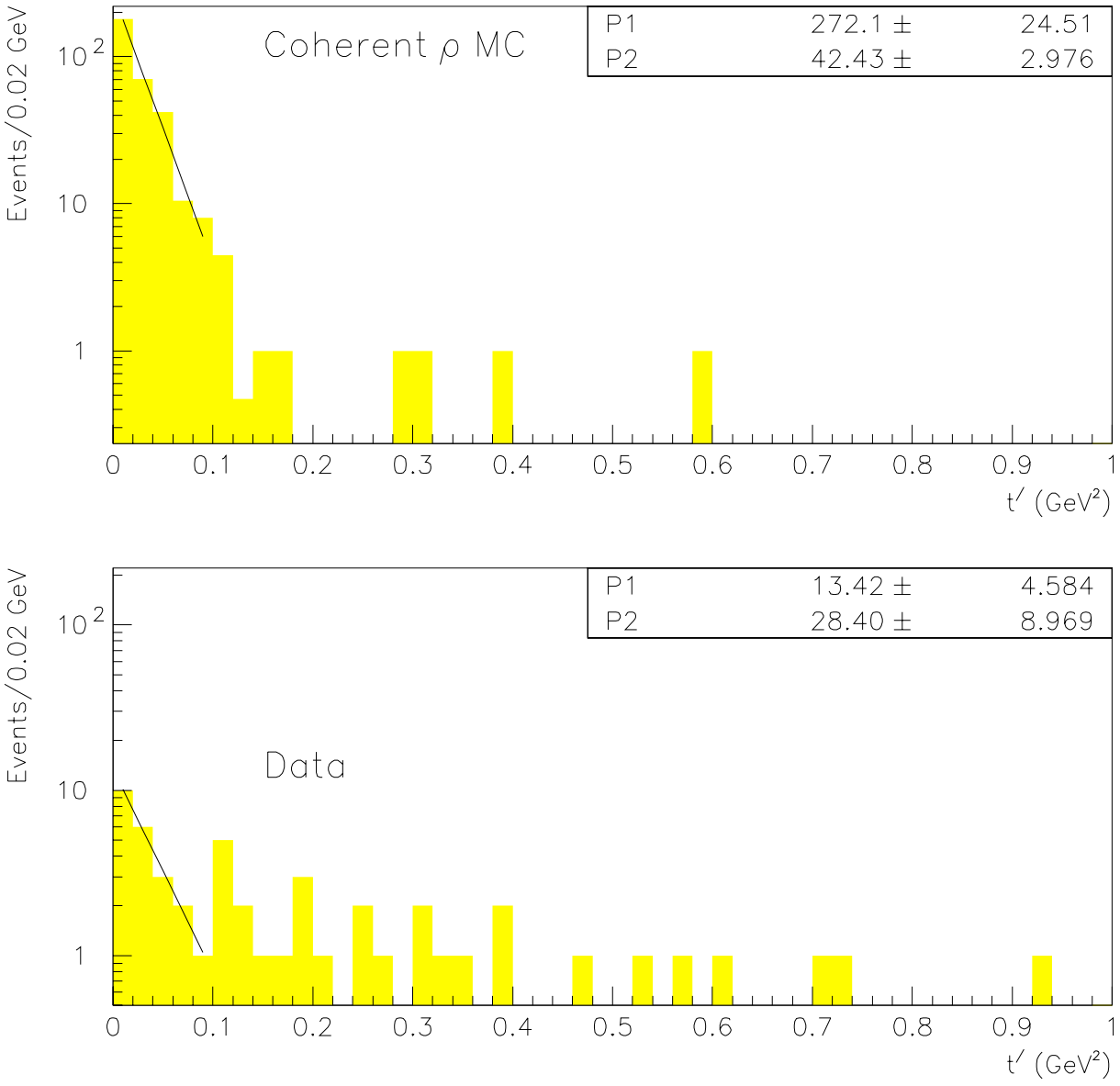

Figure 4.20: The t' -distribution of the coherent ρ Monte Carlo and the data.

minimum slopes are plotted on top of the data they reasonably represent the region in question. This uncertainty is due to the poor statistics of the distribution. The t'-distribution for the data and coherent Monte Carlo should be contrasted with that for the Deep Inelastic Scattering Monte Carlo, Figure 4.22. Although there are more events at low t' than at higher t' , these events do not exhibit the sharp exponential distribution that is typical of coherent ρ events. An attempt to fit this distribution with an exponential fuction was made. If the fit is made over the region $t' < 0.2\ GeV^2$ a slope of $(9 \pm 3)\ GeV^{-2}$ is obtained. However, the fit result varied significantly with the way the distribution was binned and with the range over which the fit was made, clearly indicating that this distribution is not well described by an exponential.

A study of these low t' Deep Inelastic Scattering Charged Current Monte Carlo events was made. These events are all events with a high t' that have been mismeasured. Appendix C lists what type of events were mismeasured to give low t' . Many events are of the type $\nu_\mu n \rightarrow \mu^- \rho^+ n$ where the neutron went undetected.

Other Kinematic Distributions

Plots of the neutrino energy (E_ν), the energy transfer (ν), to four momentum transfer from the leptonic system (Q^2), the hadronic invariant mass (W^2), and the Bjorken variables (x and y) for both the coherent Monte Carlo and the signal for those events having t' less than 0.1 GeV^2 are shown in Figure 4.23. As can be seen from Figure 4.23 the distributions from the data are similar in shape to that of the coherent Monte Carlo, providing some confidence that the data consists mainly of coherent diffractive ρ.

4.5.2 The Integrated Cross-Section.

Cross-sections can be calculated from the following relation.

$$N_{EVT} = \frac{N_T}{A} \int \epsilon \sigma(E) \phi(E) dE \tag{4.32}$$

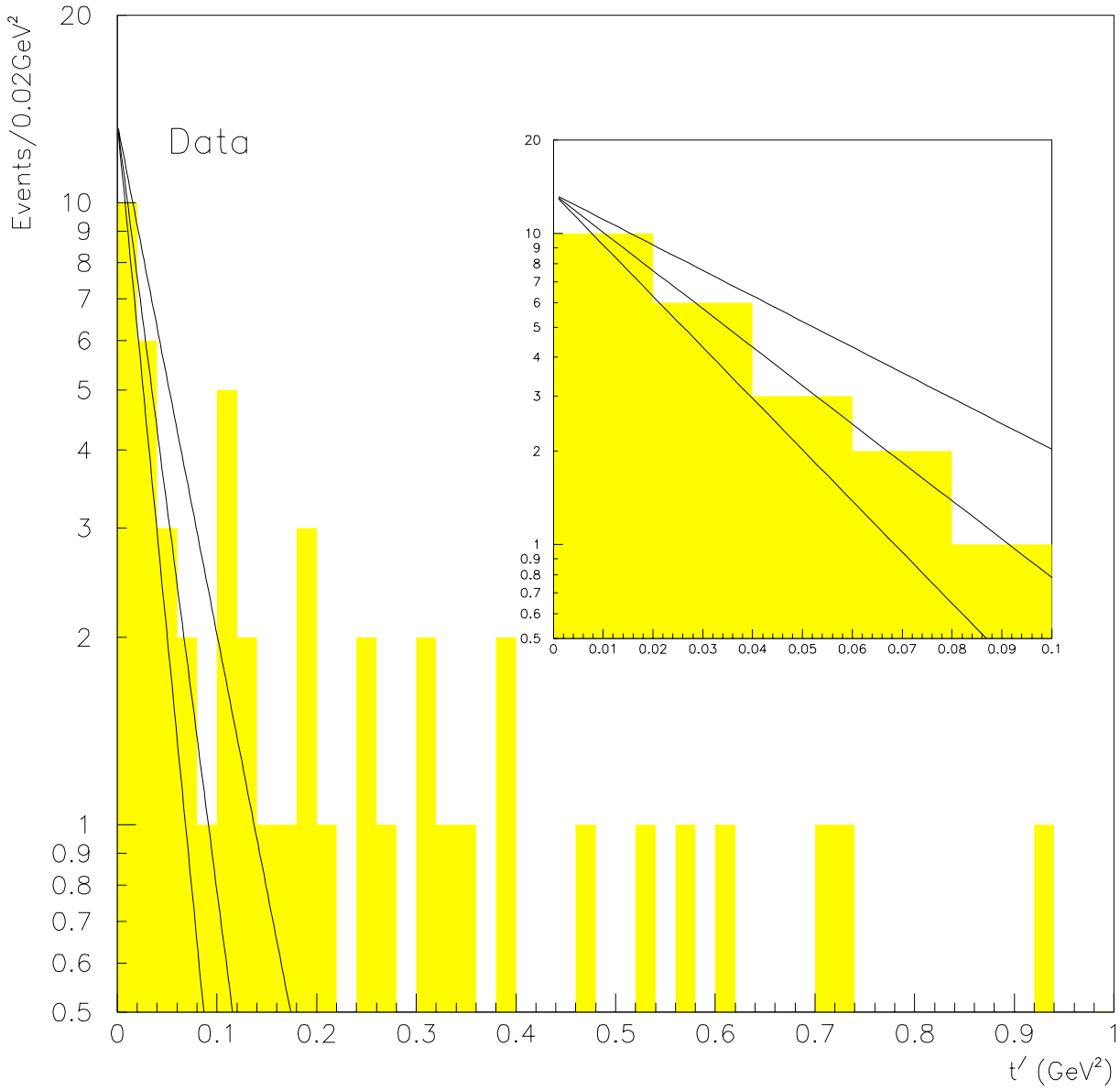

Figure 4.21: The t' -distribution of the data at low t' showing the best fit as well as the maximum and minimum slopes.

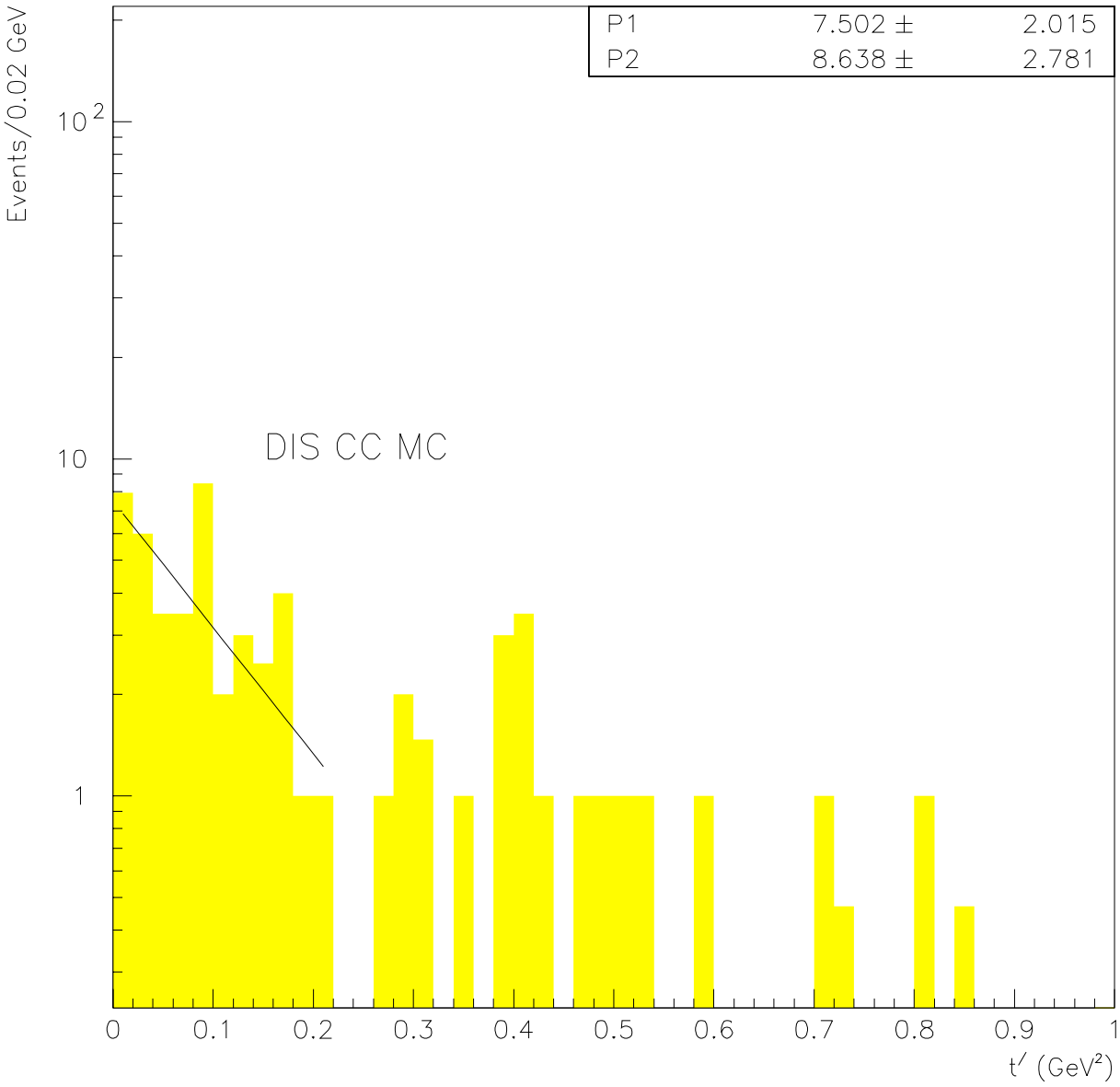

Figure 4.22: The t' -distribution of the DIS CC Monte Carlo.

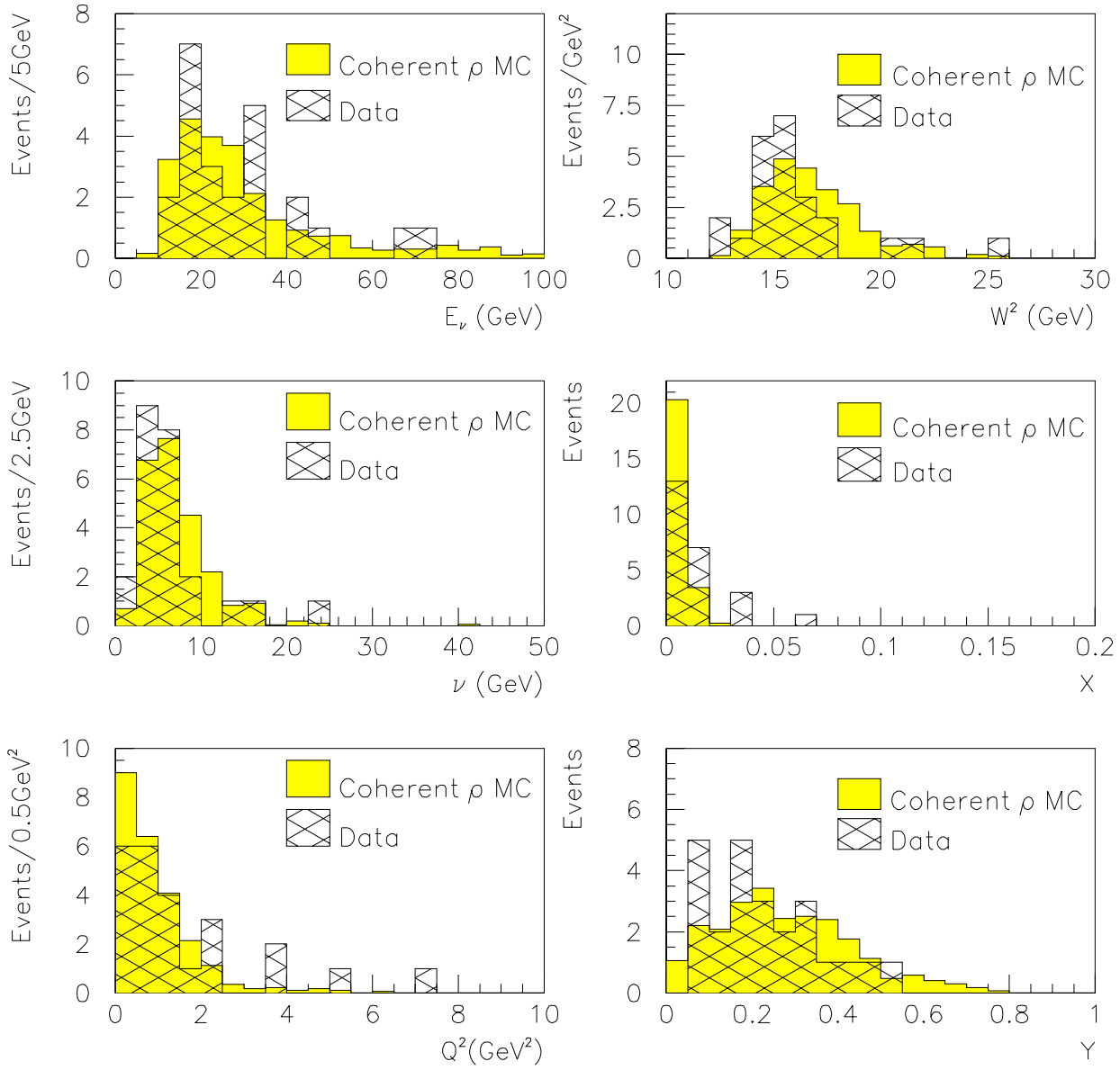

Figure 4.23: Kinematic distributions for data events with $t' < 0.1\ GeV^{-2}$ compared to those for the coherent diffractive Monte Carlo.

where N_T is the number of target nuclei, A is the cross-sectional area of NOMAD, ϵ is the efficiency including the acceptance, σ the cross-section and ϕ the neutrino flux at the detector. Of course, the cross-section can only be calculated under the assumption that a signal has been observed.

The Number of Signal Events.

The following section outlines two methods of estimating the background and so of calculating the signal.

Examination of the t'-distribution for the coherent ρ Monte Carlo reveals that nearly all events have t' less than 0.1 GeV^2. Under the assumption that the Monte Carlo describes the coherent diffractive process well, the number of observed coherent diffractive events in the data can be estimated by counting the number of events with t' less than 0.1 GeV^2. However, the problem of how to estimate the contribution of the background to this region remains.

Two approaches to estimating this background were made. The first approach is to estimate the background from the tail of the data i.e. from the data in the region $t' > 0.1\ GeV^2$. The second approach is to use the information from the Deep Inelastic Scattering CC Monte Carlo as an estimate of the background.

1. **Using the Tail of the Data as an Estimate of the Background**
   Under the first approach, we can use a constant fit to the region $t' > 0.2\ GeV^2$ to give us an estimate the background in this region. The lower limit on the range used to make this fit was chosen so as to be well clear of the exponential part of the signal, as determined by the coherent diffractive ρ Monte Carlo. The upper limit on the range was chosen somewhat arbitrarily to be 1.0 GeV^2. The effect of the choice of range on the fit result is shown in Table 4.5.

   A log-likelihood fit was used to fit the data instead of the more usual χ^2 method. The χ^2 method does not work well for distributions with low event statistics per bin. As can be seen from the way the fit result changes

Range GeV^2	Fit Result (events/0.02 GeV^2)
$0.2 \rightarrow 0.5$	0.73 ± 0.22
$0.2 \rightarrow 1.0$	0.43 ± 0.10
$0.2 \rightarrow 2.0$	0.20 ± 0.05

Table 4.5: The effect of the chosen range on the fit to the tail of the t' -distribution for the data.

with the chosen fit range, the t' -distribution greater than 0.2 GeV^2 is not well described by a constant term. However, given the available statistics, it would be difficult to fit with more parameters.

Using the result of the fit over the range $0.2 < t' < 1.0$ GeV^2, the estimated background to the t' -distribution in the five bins below 0.1 GeV^2 is:

$$N_{BKG} = 2.2 \pm 0.5 \text{ (stat)}. \tag{4.33}$$

However, the dominant uncertainty is the systematic term. This is estimated from the difference in the results fitting over the different ranges. If the mean value is assumed to be 0.43 events/0.02 GeV^2 then this leads to a systematic uncertainty of $^{+1.5}_{-1.2}$ events.

Using Figure 4.21 one can see that the number of observed events with t' less than 0.1 GeV^2 is 22. Following the method given in the Particle Data Book [12] and using the above result for the number of background events, the coherent signal is estimated to be:

$$N_{EVT} = 20 \pm 4. \tag{4.34}$$

(quoting the one sigma standard error). This method is valid under the assumption that the uncertainty on the number of background events is negligible, which is not strictly true in this case. However, there is no generally acceptable method for the case of a non-negligible uncertainty on the background. In this instance the uncertainty on the background

number of events is small compared with the statistical uncertainty on the number of observed events, $22 \pm \sqrt{22}$.

2. **Using the DIS CC Monte Carlo as an Estimate of the Background**

   The second approach assumes that the only significant background to the signal is the contribution from Deep Inelastic Scattering Charged Current events, as described in Section 4.4.2. In this approach, the tail ($0.2 < t' < 1.0\ GeV^2$) of the DIS CC Monte Carlo is normalized to the tail of the data. Again the tail is fitted using a log-likelihood method. The fit to the tail of the DIS CC Monte Carlo is (0.50±0.11) events/0.02 GeV^2, making the scaling ratio equal to

$$(0.43 \pm 0.10)/(0.50 \pm 0.11) = (0.85 \pm 0.28). \tag{4.35}$$

   The distribution is then scaled according to this normalization factor and subtracted from the data. The remaining distribution is assumed to be the contribution from coherent diffractive ρ and is shown in Figure 4.24.

   As can be seen from Figure 4.24 very few events remain after background subtraction. In fact, in the region $t' < 0.1\ GeV^2$ there are -3 events. If the maximum and minimum signals after background subtraction are used to estimate the uncertainty, the signal is estimated to be

$$N_{EVT} = -3 \pm 10. \tag{4.36}$$

   If this method were the one adopted for background estimation, the coherent diffractive ρ signal is consistent with zero.

The estimated number of signal events under the two methods of background estimation described above are summarized in Table 4.6. Given the results described above, it is not possible to say conclusively that a coherent ρ signal has

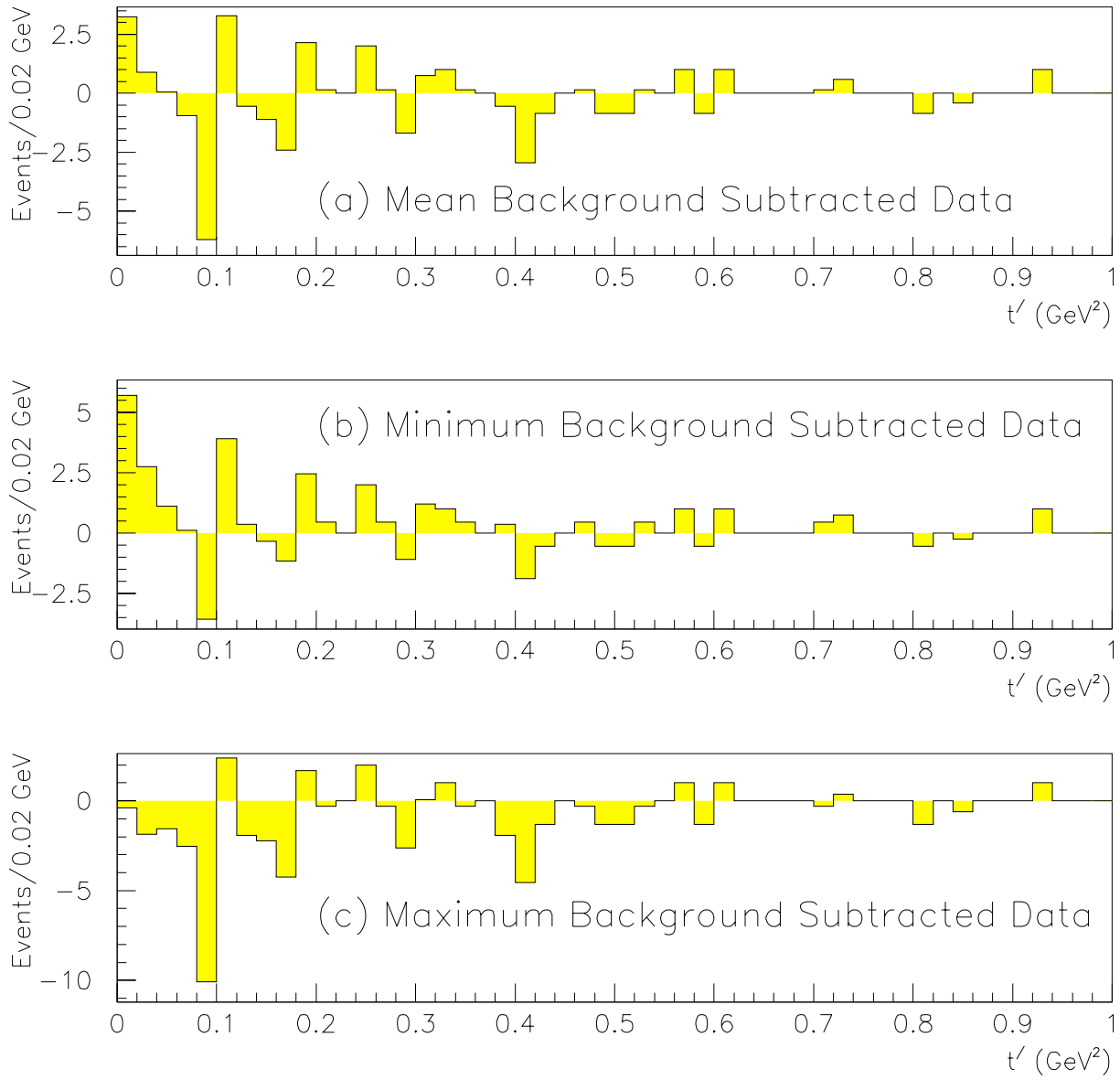

Figure 4.24: The t' -distributions for the background subtracted data. Plot (a) shows the values obtained with the mean normalization factor, plot (b) shows the maximum background subtracted distribution and plot (c) shows the minimum background subtracted signal using this method.

Method	N_{OBS}	Estimated Background	Signal
1	22	$2.2 \pm 0.5^{+1.5}_{-1.2}$	20 ± 4
2	22	25 ± 9	-3 ± 10

Table 4.6: The number of coherent events found in the data under the two methods of approach for the estimation of the background.

been seen. Nevertheless, the cross-section for this process will be calculated from the results obtained by both methods of background estimation. The advantages and disadvantages of this procedure are discussed further in Section 4.6.1.

The Number of Target Nuclei

The fiducial volume used for this analysis was $2.6 \times 2.6 \times 3.7 m^3$ corresponding to a mass of $2.5 \times 10^3 kg$. (For a full description of the NOMAD target, see Section 3.4.) The NOMAD target consists predominantly of carbon (64% by weight), oxygen (22% by weight) and nitrogen (6% by weight). The contribution from each of these elements to the coherent signal cannot be separated. Consequently, nitrogen and oxygen are treated as "carbon-like" nuclei for the purpose of this analysis. NOMAD also contains 5% hydrogen, but the contribution made by hydrogen to the coherent signal is negligible, since it should not lead to a peak at $t' < 0.1\ GeV^2$.

Using the information above we find for the full 11-module NOMAD target there is a total of 1.08×10^{29} carbon-like nuclei. In the 8-module data set there is a total of 0.78×10^{29} carbon-like nuclei.

Data Sample	N_T
8-module	7.84×10^{28}
11-module	10.78×10^{28}

Table 4.7: The number of target nuclei.

Efficiency and Acceptance

One can define the acceptance to be the number of events remaining in the signal after the effects of a non-ideal detector, eg losses of particles from the sides of the detector, losses due to the track reconstruction algorithm etc. In a perfect detector the acceptance would be 100%. One can define the efficiency to be due to the cuts and constraints individual to the analysis and a result of trying to distinguish the signal from the background. However, it is often difficult to separate one from the other. For the purpose of this analysis, the acceptance and efficiency will be combined into a single number ϵ.

An investigation was made into the energy dependence of ϵ. This investigation showed the efficiencies and acceptances seemed to be roughly independent of energy and can so be taken outside of the integral.

The inefficiencies for the reconstruction of Coherent ρ Monte Carlo are described in Sections 4.3.2 and 4.3.3 and tabulated in Table 4.2. Other analyses [20], [19] have shown the Monte Carlo process is accurate as a means of simulating the real processes that occur in NOMAD. Hence the acceptance/efficiency (ϵ) can be determined from the Monte Carlo.

$$\epsilon = (3.9 \pm 0.2)\% \tag{4.37}$$

The Neutrino Flux

The integrated neutrino flux ($\int \phi dE$) at NOMAD is dependent on a number of parameters. These parameters are outlined below.

- **The Number of Protons on Target (*p.o.t.*)**
  The performance of the CERN SPS during 1995 is summarized in Table 3.3. The data for this analysis came from a total of $6.38 \times 10^{18} p.o.t.$ [45]. More details on the neutrino beam can be found in Section 3.12.

- **The NOMAD off-time.**
  NOMAD off-time is considered to be the time when NOMAD is not taking data

because it is switched off. This usually occurs when some upgrade or repair work is scheduled that can not be completed during time when the beam itself is switched off. For the data collecting periods described in Section 4.1 the average on-time was 76% [45].

- **The NOMAD dead-time**

  NOMAD dead time is the time where the detector is running, but is not actually taking data because:

  - The event is vetoed because it coincides with a low angle cosmic ray, a spurious beam muon or a muon from any of the upstream material including the CHORUS experiment.
  - A second event occurs closely after a first one and the detector is still reading/processing the data from the first event and is unable to process the second.

  For the data taking periods used in this analysis, the NOMAD live time is 96% [20].

Data Sample	$\int \phi(E)dE$	After live time considerations
8-module	4.25×10^{16}	3.10×10^{16}
11-module	3.09×10^{16}	2.25×10^{16}

Table 4.8: The number of neutrinos at NOMAD and the number of neutrinos after live time/off time considerations for a fiducial area of $2.6 \times 2.6 m^2$.

- **The Beam Divergence.**

  Since NOMAD is placed $400m$ from the end of the decay tunnel (the WANF neutrino beam is described in Section 3.12) the beam divergence over the 400 cm length of the NOMAD target is insignificant.

- **The Beam Angle.**

  As described in Section 3.12, the neutrino beam intercepts NOMAD at a slight

angle to the horizontal. While this angle is important to the calculation of the transverse momentum, the amount of detector traversed by a neutrino is increased by less than $4mm$ compared to that which would have been traversed if the beam were horizontal. This difference is less than 0.1% and an insignificant correction to the cross-section calculation.

The neutrino flux can be calculated from the beam Monte Carlo [31] which considers all the significant factors mentioned above. The ν_μ flux as a function of energy can be seen in Figure 3.11.

The Resultant Cross-Section

Combining all the above information and inverting Equation 4.32 and under the first approach described above, we find the resultant cross-section for coherent diffractive ρ production to be

$$\begin{aligned} \sigma_{TOT} &= \frac{N_{EVT}A}{\epsilon(N_T \int \phi(E)dE)} \\ &= \frac{20 \times (260)^2}{0.039 \times [(7.84 \times 10^{28} \times 3.10 \times 10^{16}) + (10.78 \times 10^{28} \times 2.25 \times 10^{16})]} \\ &= 71 \times 10^{-40}\ cm^2 \end{aligned} \tag{4.38}$$

Under the second approach the resultant cross-section for coherent diffractive ρ is calculated to be zero (since a negative cross-section is un-physical).

Uncertainty

The largest contribution to the uncertainty on the cross-section is the uncertainty on the number of observed coherent events. All other potential sources of error are insignificant in comparison. This approximation can be used to simplify the calculation of the uncertainty on the cross-section.

$$\frac{\delta\sigma}{\sigma} = \frac{\delta N_{EVT}}{N_{EVT}} = \frac{4}{20} \tag{4.39}$$

Under the first approach and using the information from Table 4.6 the cross-section is therefore calculated to be

$$(71 \pm 14) \times 10^{-40}\ cm^2 \tag{4.40}$$

Under the second approach and the same approximations as for the first approach, the cross-section is

$$(0 \pm 32) \times 10^{-40}\ cm^2 \tag{4.41}$$

which is consistent with zero (again it is noted that negative cross-sections are unphysical).

4.6 Discussion

4.6.1 Comparison of Background Estimation Methods

Two possible methods of estimating the background to the coherent diffractive ρ signal have been described in Section 4.5.2. The limitations and advantages of each method are discussed below.

Under the the first approach a non-zero cross-section has been measured and a fit to the t'-distribution has been performed. The slope of this t'-distribution is $b = (28 \pm 9)\ GeV^{-2}$ and is consistent with that predicted by the coherent diffractive Monte Carlo.

The results obtained under this approach are limited by the lack of available statistics. The tail of the distribution is used to estimate the number of background events in the signal region. However, the tail of the distribution ($0.2 < t' < 1.0\ GeV^2$) contains only 16 events. A constant has been used to fit this tail. The poor statistics in this region limit the accuracy of this fit. This method is limited because it relies heavily on the assumption that the background to the signal is flat and so the result is dominated by the systematic uncertainty.

Under the second approach, the coherent diffractive ρ signal is consistent with zero. Again, this method is limited by poor statistics. In the region $0.2 < t' < 1.0\ GeV^2$ of the Deep Inelastic Scattering Charged Current Monte Carlo there are only 29.5 events. The tail of this distribution is used to normalize it to the data. It has been assumed in this work that the tail of the distribution is flat. However, this assumption was made because the poor statistics limited the fit to one of few parameters. Given many more events, it would be possible to better normalize this this distribution.

It is not only the tail of the Deep Inelastic Scattering Monte Carlo that suffers from a lack of statisitcs. The region $t' < 0.1\ GeV^2$ also has a limited number of events and peaks weakly near zero. Since it is this part of the distribution that is being subtracted from the data to leave a signal, it is important that this region is an accurate representation of the data. Since the data is also contains only a limited number of events, a small statistical fluctuation here can have a significant effect on the size and shape of the signal. This effect is clearly illustrated by the excess of events at around $t' = 0.09\ GeV^2$.

The second approach is good in that it does not make any a priori assumptions about the shape of the background to the coherent signal, but it relies on assumption that the Deep Inelastic Charged Current Monte Carlo accurately represents the data in the kind of events that can fake coherent diffractive ρ. As the name implies, the Deep Inelastic Scattering Monte Carlo has been designed to model the Deep Inelastic Scattering process, but has not been tuned at kinematical extremes similar to those present in coherent diffractive ρ scattering. This method is limited by the accuracy of this Monte Carlo in this kinematic region.

4.6.2 Comparison With Theoretical Predictions, Assuming a Signal.

In the following sections it is only the signal calculated using the first approach that is compared to the theoretical predictions and to previous measurements. The result using the second approach is not invalid, but not much can be

learnt from making this comparison.

Section 2.4.4 describes the theoretical prediction for the value of the cross-section. For carbon-like nuclei at the neutrino energies at NOMAD, theory predicts a cross-section of $(40 \rightarrow 70) \times 10^{-40}\ cm^2$, depending on the exact form of the model used. The cross-section measured using NOMAD agrees within the calculated uncertainty limits with that predicted by theory. Even the lower limit of the prediction still lies within two standard deviations of the measurement.

Given the uncertainty on the cross-section result, it is impossible to make any distinction between the different theoretical models. However, with an increase in the number of neutrino interactions measured by NOMAD a greater statistical certainty should be achievable.

4.6.3 Comparison With Previous Measurements.

E546

Using a 47% molar neon target, the E546 [8] experiment observed 11 events with an estimated background of 1.5 ± 1. This group measured the cross-section per neon nucleus to be $(0.28 \pm 0.10)\%$ of the total charged current neutrino cross-section at the FNAL Quadrapole Triplet Beam. This corresponds to a coherent cross-section of $(280 \pm 100) \times 10^{-40}\ cm^2/$ neon nucleus.

WA59

The WA59 [48], [49] experiment used a 75% neon 25% hydrogen target and an anti-neutrino beam to observe 40 events with $|t| < 0.10\ GeV^2$ with a complete π^0 reconstruction with an estimated background of 7 ± 4 events. This group measured the cross-section to be $(95 \pm 25) \times 10^{-40}\ cm^2/$ neon nucleus or $(0.58 \pm .15)\%$ of the total charged current cross-section for anti-neutrinos at energies given by the neutrino beam from the CERN SPS.

E632

The E632 [50] experiment used a neon-hydrogen target (75% molar neon 1985, 63% molar neon 1987-1988) and the FNAL Quadrapole Triplet Beam (ν) to measure a signal of 19 events with an estimated background of 7 events. This group measured the cross-section to be $(210 \pm 80) \times 10^{-40}\ cm^2/$ neon nucleus.

NOMAD

Using 1995 data alone, NOMAD has observed 22 events with $t' < 0.10\ GeV^2$ with a complete π^0 reconstruction with an estimated background of 2 ± 0.5 (stat) $\pm$ 1.5 (syst) events. The coherent signal is therefore estimated to be 20 ± 4 events. The cross-section was measured to be $(71 \pm 14) \times 10^{-40}\ cm^2/$ carbon nucleus.

4.6.4 Discussion

Table 4.9 shows results from NOMAD along with those from previous experiments described above.

Experiment	$\overline{E}_\nu(GeV)$	Target	No. Observed Events	Coherent Signal	$\sigma(10^{-40}cm^2)$	
E546	80	Ne	12	9.5 ± 3	(280 ± 100)	per Ne nucl
WA59	25	Ne	40	33 ± 7	(95 ± 25)	per Ne nucl
E632	80	Ne	26	19 ± 7	(210 ± 80)	per Ne nucl
NOMAD	24	C	22	20 ± 4	(71 ± 14)	per C-like nucl

Table 4.9: A comparison between this result and previous cross-section measurements.

It should be stressed that NOMAD is using predominantly carbon as a target, whereas previous experiments used neon. Section 2.4.5 gives a description of how the choice of target nuclei alters the predicted cross-section. For carbon nuclei, the cross-section is predicted to be around 40% lower than that predicted for neon nuclei. If the cross-section result from the WA59 experiment (since this experiment was performed at the same beam energy as NOMAD) which used neon as a target,

is scaled to reflect this reduction it would be $38 \times 10^{-40} cm^2$. Hence under the most optimistic approach presented in this analysis, $\sigma = (71 \pm 14) \times 10^{-40} cm^2$, the NOMAD result is in agreement with the WA59 result within the stated uncertainties. Given the rather large uncertainties of all results, no further distinction can be made.

Chapter 5

Conclusion

The diffractive model combines the hadron dominance model of interactions with that of the conservation of vector current. The model has not been contradicted by various tests made by experiments using bubble chambers filled with neon. However, thorough tests on other nuclei have yet to be performed.

Using data from 1995 taken from NOMAD exposed to the CERN SPS ν_μ beam, a study of the coherent diffractive production of ρ mesons was made. 22 events with $t' < 0.1\ GeV^2$ were observed. Under an optimistic method of background estimation, the signal was estimated to be 20 ± 4 events and to have a slope of $b = (28 \pm 9)\ GeV^{-2}$. This corresponds to a measured cross-section of $(71 \pm 14) \times 10^{-40} cm^2$ which consistent with previous experiments and current theoretical predictions within the uncertainty of the measurement. The distributions of the kinematic variables are in agreement with the theoretical predictions from CVC and VMD models.

However it has been shown that in 1995 alone NOMAD has not been able to measure coherent diffractive ρ to levels comparable to earlier experiments. As more data is taken and processed it is hoped that a significant level of improvement can be made on the measurement of the coherent diffractive ρ production cross-section and a fuller understanding of the kinematics of this process can be gained.

5.1 Future

The data presented in this work were taken from a period when 0.6×10^{19} *p.o.t.* were delivered. During 1996 a total of 1.4×10^{19} *p.o.t.* were delivered. If the two data sets are combined and the expected number of coherent diffractive ρ events are estimated by naively scaling the measured number of events with the number of protons on target we expect an increase of a factor of ≈ 3 in the number of observed events.

Since my analysis on the 1995 data was done, the NOMAD reconstruction software has been significantly improved. The main improvements are in the area of drift chamber track reconstruction, in particular, the software is now much more efficient at constructing tracks from track segments, i.e. tracks arising from the same particle that in 1995 would have been assigned to to track segments are now joined together to make a unique track. This increase in track construction efficiency has been estimated to increase the overall efficiency for coherent ρ by a factor of ≈ 3.

Not only would the improved reconstruction software help the search for coherent ρ by improving the efficiency, it would also help to give a more accurate measurement of important parameters such as charged particle momenta.

Combining the increase in statistics due to the larger neutrino flux with the increase due to the improvement in track reconstruction efficient, we would expect to observe ≈ 200 events in the low t' region. If the background estimate was similarly scaled under the optimistic approach and we follow the same procedure outlined in Section 4.5.2 we would expect to observe a signal of (180 ± 14) events, corresponding to a cross-section of $(71\pm6)\times10^{-40}cm^2$ i.e. the statistical uncertainty on the measurement would be more than halved. This measurement would then be the most statistically significant measurement to date.

It would be possible to further improve the results presented here in a number of ways. Firstly, the number of events in the DIS CC Monte Carlo could be increased significantly to allow a better estimation of the background to the t' -distribution. Potentially, this would also make it possible to fine-tune some of the cuts presented

in Section 4.3 and further reduce the amount of DIS CC events contaminating the sample.

In an ideal world it would be possible to do a double check on the calculations performed in Section 4.5.2 by calculating the cross-sections for the 8-module and 11-module data individually and then comparing the results. However, the very small amount of available data makes this double check impractical.

Similarly, it would be a nice exercise to calculate the cross-section for a number of different energy bins. Theory predicts, and this is supported by evidence from previous experiments, that the cross-section increases with energy. However, the data in support of this is a result obtained from experiments that have been run at different neutrino beam energies and not from the same experiment with data split into different energy regions. Again the very small amount of available data makes this impractical.

Appendix A

An outline of my personal involvement with NOMAD.

The search for coherent diffractive ρ forms the bulk of this thesis. During the pursuit of this task, however, I was involved in various activities, not always directly related to the main subject of the thesis. Nevertheless these other tasks were important to the smooth operation of the experiment as a whole.

During periods spent at CERN (typically three months per year for four years), I participated in data taking runs for the NOMAD experiment. Naturally, this involved checking the quality of the data taken by all the subdetectors during the data taking runs.

The NOMAD veto (Section 3.3 describes the NOMAD veto in more detail) was designed and constructed by the Australian groups of which I was a member. In particular, I was involved in the installation and testing of the plastic scintillator veto, photomultiplier tubes and associated electronics. I shared responsibility for the development of online monitoring and control for this equipment (veto slow control). This task involved writing a LabVIEW [51] program to monitor photomultiplier high voltages, discriminator levels etc and to activate alarms designed to alert the people on shift if these values fell outside their normal range. I also had occasion to act in the capacity of "*veto expert*", the person ultimately responsible for the smooth performance of the veto.

The analysis of the coherent ρ signal was somewhat tangential to the main aim of NOMAD to search for neutrino mass oscillations. However, some essential

elements of the coherent ρ analysis, were also important to the oscillation search. In particular, the early work done by myself in establishing a π^0 signal in the data was used by the collaboration as a stepping stone to the search for oscillations via the hadronic decay mode of the τ.

A.0.1 List of Publications.

I am a co-author of the following papers:

- NOMAD Collaboration
  The NOMAD Experiment at the CERN SPS: A Status Report
  Memo 95-27 30 June, 1995

- NOMAD Collaboration
  The NOMAD experiment at the CERN SPS.
  Accepted for publication in Nuclear Instruments and Methods A.

Appendix B

Derivation of t.

Assuming the target nuclei is initially at rest, the four-momentum transfer to the nucleus squared can be written as

$$\begin{aligned} t &= (p - p')^2 \\ &= K_N^2 - (\vec{p}_N)^2 \end{aligned} \tag{B.1}$$

where $\vec{p_N}$ is the three-momentum and K_N is the kinetic energy of the final state nucleus. It can also be expressed as

$$t = 2m_N K_N \tag{B.2}$$

Conservation of momentum implies

$$\vec{p}_N = \vec{p}_\nu - \sum_i \vec{p}_i \tag{B.3}$$

where the sum is over all the observed final state paritcles, in this case the muon and the charged and neutral pions.

Conservation of energy implies

$$E_\nu + m_N = \sum_i E_i + m_N + K_N \tag{B.4}$$

and again the sum is over all the observed final state particles.

If we now split Equation B.3 into componants parallel to $(\hat{z})$ and transverse to

the neutrino beam and substitute the result from Equation B.4 we find an expression for the three-momentum of the final state nucleus

$$\vec{p}_N = [\sum_i E_i - \sum_i p_i^L + K_N]\hat{z} - \sum_i p_i^T \tag{B.5}$$

where the superscripts L and T refer to the componant of the particle momentum parallel to and transverse to the neutrino beam respectively.

We can now square the three-momentum to give

$$|\vec{p}_N|^2 = [\sum_i (E_i - p_i^L)]^2 + K_N^2 + 2K_N \sum_i (E_i - p_i^L) + (\sum_i p_i^T)^2. \tag{B.6}$$

Substituting the above results into Equation B.1, we can find the exact expression for t

$$|t| = [\sum_i (E_i - p_i^L)]^2 + 2K_N \sum_i (E_i - p_i^L) + (\sum_i p_i^T)^2. \tag{B.7}$$

Equation B.2 gives the relationship between K_N and t. If we now substitute this expression for K_N into B.7 into the above equation we find

$$|t| = [\sum_i (E_i - p_i^L)]^2 + (\sum_i p_i^T)^2 + 2\frac{t}{2m_N} \sum_i (E_i - p_i^L) \tag{B.8}$$

Some simple algebra now leads us to the final exact expression for $|t|$

$$|t| = \frac{[\sum_i (E_i - p_i^L)]^2 + (\sum_i p_i^T)^2}{(1 - \frac{\sum_i (E_i - p_i^L)}{m_N})} \tag{B.9}$$

At small values of $|t|$ the fraction $\frac{\sum_i (E_i - p_i^L)}{m_N}$ is much smaller than one, and so to a good approximation

$$|t| = [\sum_i (E_i - p_i^L)]^2 + (\sum_i p_i^T)^2 \tag{B.10}$$

the expression used in much of the literature.

Appendix C

A Summary of Deep Inelastic Scattering Monte Carlo Events that Fake Coherent Diffractive ρ.

The events tabulated below are a sub-sample of the 132,064 Deep Inelastic Scattering Monte Carlo events simulated to investigate possible backgrounds to the coherent diffractive ρ signal. Each of these events passed the analysis cuts described in Section 4.3.3 and tabulated in Table 4.2. Each event also satisfies the further criteria that t' is less than 0.1 GeV^2.

Background Type	Comment	No. of Events
$\nu n \rightarrow \mu^- \rho^+ n$	small p_T neutron is missed	13
$\nu p \rightarrow \mu^- \rho^+ \pi^+ n$	missed both the neutron and π^+	7
$\nu n \rightarrow \mu^- \rho^+ \pi^0 n$	missed both the neutron and π^0	4
$\nu n \rightarrow \mu^- \rho^+ \pi^0$	miss the π^0 from the ρ decay, mismeasure π^+	1
$\nu n \rightarrow \mu^- \pi^0 \pi^+ n$	miss the neutron and get M_ρ from $\pi^+\pi^0$ pair	1
$\nu n \rightarrow \mu^- \pi^0 \pi^+ n \pi^0$	miss the neutron and one π^0	1
$\nu n \rightarrow \mu^- \rho^+ \Delta^0 \eta^0$	miss the Δ^0 and the η^0	1
$\nu p \rightarrow \mu^- \eta \Delta^{++}$	miss π^+ from Δ^{++} decay, mismeasure η mass	1
$\nu p \rightarrow \mu^- \pi^0 \Delta^{++}$	missed π^+ from Δ^{++} decay, misidentified p	1
total		30

Table C.1: Low multiplicty charged current background event types.

Bibliography

[1] Piketty & Stodolsky

Diffraction Model of High-Energy Leptonic Interactions.

Nucl. Phys. B15 (1970) 571-600

[2] A.M. Polyakov *et al*

Theory of Pomeron Interactions

JETP Lett. 19:147, 1974

[3] S.Weinberg

A model of Leptons

Phys Rev Letters 19 1264-1266, 1967

A. Salam

Proc. 8th Nobel Symp. Stockholm (1968) 367

[4] Feynman & Gell-Mann

Theory of Fermi Interaction

Phys Rev, Volume 109, 193-198, 1958

[5] S. L. Adler

Tests of the Conserved Vector Current and Partially Conserved Axial-Vector Current Hypotheses in High-Energy Neutrino Reactions

Phys Rev, Volume 135, number 4B, (August 24 1964) 963-966.

[6] B.Z. Kopeliovich & P. Marage

Low Q^2, high ν neutrino physics (CVC, PCAC, hadron dominance)

International Journal of Modern Physics A, Vol. 8, No 9 (1993) 1513-1602

[7] M.K. Gaillard & C.A. Piketty
Diffractive Neutrino Production of Vector Mesons.
Phys Lett B Volume 68B, number 3, (June 6 1977) 267-270

[8] H.C. Ballagh *et al* E546 Collaboration
Coherent ρ^+ Production in Neutrino-Neon Interactions.
Phys Rev D Volume 37, number 7, 1 April 1988 1744-1749

[9] M.S. Chen *et al*
Diffractive Production of Vector Mesons in Lepton-Nucleon Intereactions.
Nucl. Phys. B118 (1977) 345-35

[10] A. Bartl *et al*
Neutrino Production of Vector and Axial-Vector Mesons at High Energies.
Phys Rev D16 (1977) 2124

[11] A.W. Thomas
CVC in Particle Physics.
International Symposium on Non-Nucleonic Degrees of Freedom Detected in Nucleus - NMDF '96, Osaka Japan 2-5 September 1996.

[12] Particle Data Group
Review of Particle Properties
The American Physical Society
Phys Rev D45-II 1994

[13] D. Rein & L.M. Sehgal
Coherent π^0 production in neutrino reactions.
Nucl. Phys. B223 (1983) 29-44

[14] A.A. Bel'kov & B.Z. Kopeliovich
The Adler relation and neutrino production of single hadrons.
Sov. J. Nucl. Phys. 46(3) (1987) 499-505

[15] NOMAD Collaboration

Search for the Oscillation $\nu_\mu \rightarrow \nu_\tau$

CERN-SPSLC/91-21 SPSC/P261 11 March 1991

[16] NOMAD Collaboration

Addendum to Proposal P261 Search for $\nu_\mu - \nu_\tau$ Oscillation

CERN-SPSLC/91-48 SPSC/P261 Add1 21 August 1991

[17] NOMAD Collaboration

Addendum to Proposal P261 Search for $\nu_\mu - \nu_\tau$ Oscillation

CERN-SPSLC/91-53 SPSC/P261 Add2 25 October 1991

[18] NOMAD Collaboration

NOMAD Status Report

24 August 1993

[19] NOMAD Collaboration

The NOMAD Experiment at the CERN SPS: A Status Report

Memo 95-27 30 June, 1995

[20] NOMAD Collaboration

The NOMAD experiment at the CERN SPS.

Preprint submitted to Elsevier Science 20 October 1996.

[21] P. Astier *et al*

Nomad Reconstruction Software Drift Chamber Package Version 5 Release 7.

June 24 1995

[22] F. Fruhwirth

Kalman Filtering.

Nucl. Instr. and Meth. A, 62, 1987, 444.

[23] I. G. Bird

Vertex Finding and Fitting Package.

May 9, 1996

[24] Martine Steininger
Private communication June 1995

[25] M.Mezzetto
The NOMAD electromagnetic calorimeter
BNL Conference - 1994

[26] M. Baldo-Ceolin *et al*
Extraction of the calibration constants of the NOMAD E.M. calorimeter.
NOMAD Memo 58, August 11, 1994

[27] F. Pastore & R. Petti
Energy Resolution and linearity of the lead-glass E.M. calorimeter.
NOMAD memo 47, April 11, 1994

[28] P.W. Cattaneo *et al*
The Reconstruction Algorithm and Bank Structure for the E.M. Calorimeter.
November 1995

[29] D. Ferrere *et al*
The Reconstruction Algorithm and Data Formats for the NOMAD Muon Chambers.
December 1995

[30] Emmanuel Tsesmelis
Search for Neutrino Oscillations at the CERN SPS
Proceedings of the 22nd INS International Symposium on Physics with High Energy Colliders, Tokyo, 8-10 March 1994

[31] Charm2 Collaboration & NOMAD Collaboration
GBEAM-document in preparation
1997

[32] A. Geiser & J. Long
Study of ν_μ-CC Events and Comparison with NUBEAM, NEGLIB and GENOM.
Memo 97-005 13 February 1997

[33] I.G. Bird
NOMAD reconstruction program.
Memo 37 24 September 1993

[34] NOMAD Collaboration
NOMAD GEANT Off-line Manual.
4 July 1994

[35] Application Software Group Computing and Networks Division CERN Geneva, Switzerland
GEANT Detector Description and Simulation Tool.
CERN Program Library Long Writeups Q123

[36] NOMAD Collaboration
NOMAD Event Generator Off-line Manual.
20 December 1994

[37] LUND
LEPTO Version 6.1-The Lund Monte Carlo for Deep Inelastic Lepton-Nucleon Scattering.
May 1992

[38] P. Astier *et al*
NOMAD Reconstruction Software Extrapolator Package.
October 1995

[39] T. Fazio *et al*
NOMAD TRD Electron Identification: Method and First Results
Memo 95-041 November 1995

[40] J. P. Meyer
Drift Chamber Chemical Composition
Memo 96-003 March 1996

[41] H.J. Grabosch *et al*
Cross-section measurements of single pion production in charged current neutrino and anti-neutrino interactions.
Z Phys C41 (1989) 527-531

[42] G.T. Jones *et al*
Experimental test of the PCAC hypothesis in the reactions $\nu_\mu p \rightarrow \mu^- p\pi^+$ and $\overline{\nu_\mu} p \rightarrow \mu^+ p\pi^-$ in the $\Delta(1232)$ region.
Z Phys C43, 527-540, 1989

[43] D.Rein & L.M.Seghal
Neutrino Excitation of Baryon Resonances and Single Pion Production.
Ann Phys 133:79 1981

[44] F. James & M. Roos
MINUIT-Function Minimization and Error Analysis
CERN Program Library D506 1988.

[45] Paul Soler
Run News
Presentation at the NOMAD General Meeting 12 October 1995

[46] J. Bell *et al*
Diffractive Production of Vector Mesons in High-Energy Neutrino Interactions.
Phys. Rev. Lett. Volume 40, Number 17, (8 May 1978) 1226-1229

[47] V.V. Ammosov *et al* E180 Collaboration
Study of the Reaction $\overline{\nu} N \rightarrow \mu^+ \rho^- N$ at High Energies.
Sov. J. Nucl. Phys. 42(2), (August 1985) 236-237

[48] P. Marage *et al* WA59 Collaboration
Coherent Production of ρ Mesons in Charged Current Antineutrino-Neon Interactions in BEBC.
Z Phys C35 (1987) 275-282

[49] P. Marage *et al* WA59 Collaboration
Observation of Coherent Diffractive Charged Current Interactions of Antineutrinos on Neon Nuclei.
Phys Lett B140 (1984) 137-141

[50] S Willocq *et al* E632 Collaboration
Coherent Production of Single Pions and ρ Mesons in Charged-Current Interactions of Neutrinos on Neon Nuclei at the Fermilab Tevatron.
Phys Rev D47 (1993) 2661

[51] National Instruments, Austin, TX.
LabVIEW for Macintosh